68-10,448

AVULA, Xavier Jayaseela Rao, 1936-
UNSTEADY FLOW IN THE ENTRANCE REGION OF A CIRCULAR TUBE.

Iowa State University, Ph. D., 1968
Engineering Mechanics

University Microfilms, Inc., Ann Arbor, Michigan

UNSTEADY FLOW IN THE ENTRANCE REGION OF A CIRCULAR TUBE

by

Xavier Jayaseela Rao Avula

A Dissertation Submitted to the
Graduate Faculty in Partial Fulfillment of
The Requirements for the Degree of
DOCTOR OF PHILOSOPHY

Major Subject: Engineering Mechanics

Approved:

Signature was redacted for privacy.

In Charge of Major Work

Signature was redacted for privacy.

Head of Major Department

Signature was redacted for privacy.

Dean of Graduate College

Iowa State University
Of Science and Technology
Ames, Iowa

1968

TABLE OF CONTENTS

I. INTRODUCTION

In this investigation the unsteady, laminar flow of a viscous, incompressible fluid in the entrance region of a circular tube is treated analytically and experimentally. In particular, the case for a fluid initially at rest and rapidly set in motion under a constant head is considered. Such a starting flow situation is often experienced, but relatively little research has been done on this problem.

To provide a proper background to the unsteady entrance region problem it is appropriate to discuss the developing flow phenomenon for the steady flow case. When a fluid flows steadily and smoothly through a tube connected to a large reservoir the velocity distribution in the tube changes from some initial uniform velocity profile at the tube entrance to a fully developed parabolic profile, which is independent of axial position far downstream. The pressure gradient also varies from some initial value at the inlet to a value that remains essentially constant beyond some downstream position. The length of the tube over which this change takes place is designated the entrance length (Figure 1-a). The change in the velocity profile is due to the viscous forces. Through the influence of wall friction, flow near the wall is retarded, and a boundary layer starts growing at the inlet and gradually approaches the tube center as the flow proceeds downstream. A core of fluid essentially

undisturbed by the wall friction, but accelerated to compensate for the retarded flow near the wall, exists in the central portion of the tube. Close to the entrance where the boundary layer is thin and the velocity gradient is large there will be high friction loss in comparison to that occurring in the fully developed region. Also, the variation in the velocity profile with axial location contributes to a momentum change resulting in a relatively high pressure drop.

For the case of unsteady flow, in which the entrance velocity is time-dependent, the downstream velocity profile depends on both axial position and time. Also, one can visualize an entrance length beyond which the velocity distribution and pressure gradient are independent of location, but dependent on time. It should be emphasized that for this case the entrance length depends on time (Figure 1-b). The objectives of the present investigation were: (1) to determine the velocity profile at any instant and position in the entrance region when the flow is started from rest, (2) to determine the time-dependent entrance length theoretically and compare with an experimentally determined value, and (3) to develop a suitable experimental technique for unsteady flow problems of this type.

A survey of the fluid mechanics literature has shown that the integral momentum equation has not been fully exploited in solving unsteady flow problems. An attempt has been made

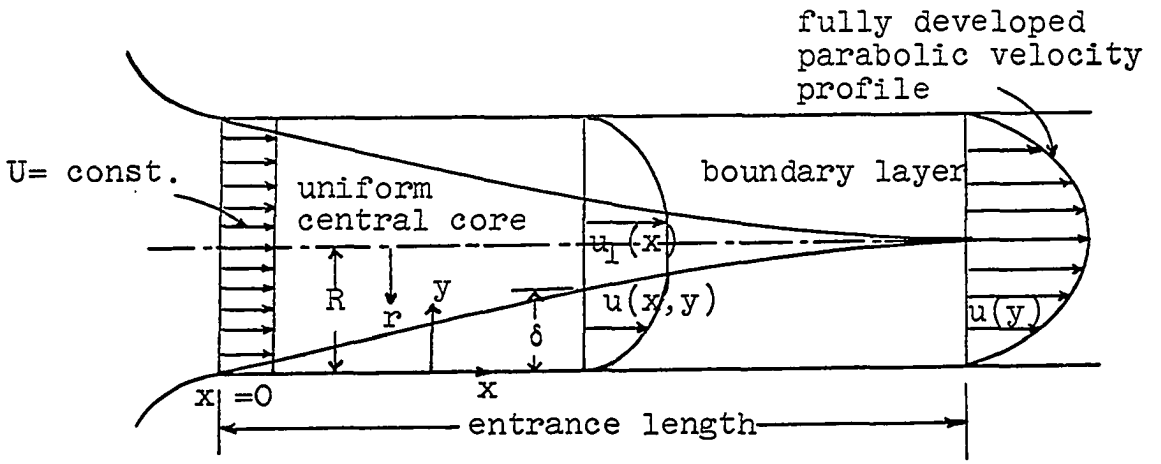

Fig. 1-a. Boundary layer model for steady flow in the entrance region of a circular tube.

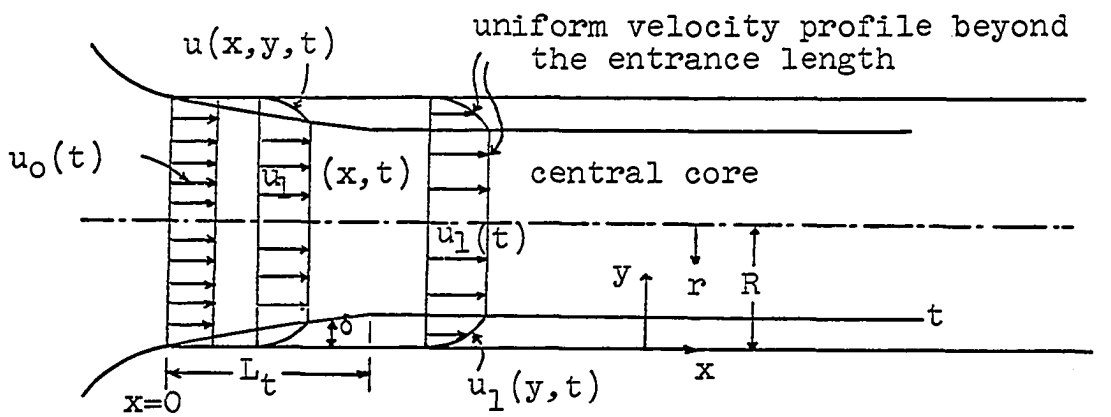

Fig. 1-b. Boundary layer model for unsteady flow in the entrance region of a circular tube. L_t is the entrance length at time t.

in this study to use this equation in conjunction with a boundary layer model in the entrance region to obtain a theoretical solution of the problem under consideration.

II. REVIEW OF LITERATURE

In view of the importance of the flow characteristics in the entrance region there has been considerable interest in the so-called "entrance-region" problem. Various investigators have attacked the steady flow problem using several different methods of solution, and numerous solutions are available.

For steady flow in the entrance region of a circular tube Langhaar (13) by means of a linearizing approximation solved the Navier-Stokes equations. The family of velocity profiles were defined by Bessel functions and expressions for pressure drop and entrance length were obtained. Han (9) applied a similar technique to rectangular ducts. The linearizing method was also applied by Lundgren et al. (14) for determining the pressure drop in the entrance region of ducts of arbitrary cross section. The most significant aspect of this method was that the incremental pressure drop in the entrance length could be calculated from a knowledge of the fully developed velocity profile alone. Results of the application of this method to a variety of duct cross-sections were in good agreement with the available analytical and experimental results.

Another method consisting of patching boundary layer solutions, that apply near the beginning of entrance region, to perturbations of the fully developed solutions that apply

far downstream was used by Schlichting (18) for the parallel plate channel. This method with a slight variation was applied to a circular tube by Atkinson and Goldstein (8).

Still another approach considering an integral representation of the momentum equation for a circular tube was followed by Schiller (17) in which a boundary layer and inviscid core model was assumed for the entire entrance region. In this approach the velocity profile was described as a parabolic one. Campbell and Slattery (3) refined Schiller's solution by accounting for viscous dissipation within the boundary layer.

A numerical approach was considered by Wang and Longwell (24) using the Navier-Stokes equations for the inlet region of a channel. Hornbeck (11) solved numerically the boundary layer equations for the entrance region of a circular tube.

While numerous references are available for steady flow very few were found that are related to unsteady flow in the entrance region of ducts. Atabek (1) using a linearizing approximation, solved the Navier-Stokes equations for unsteady and oscillating flows in the entrance region of coaxial tubes, tubes and channels with the inlet velocity described as an arbitrary function of time. However, the starting flow problem of the type considered in the present investigation was not solved. Atabek, Chang and Fingerson (2) published an experimental study on the measurement of

oscillating flow in the inlet region of a circular tube to verify Atabek's earlier theory. The experimental results were in good agreement with the theory. Pearson (15) using a numerical technique solved the Navier-Stokes equations for the time-dependent laminar flow of a viscous fluid in the inlet section between two suddenly accelerated parallel plates.

There are a number of publications on unsteady boundary layers which are of interest with respect to this thesis. Stewartson (22) published a paper concerned with the motion of a fluid in a boundary layer developed on an impulsively started semi-infinite plate. In one of his approaches he obtained an approximate solution from the boundary layer integral momentum equation by the method of characteristics. His results were in good agreement both with Rayleigh's solution for the infinite plate (for small time) and with Blasius's solution for the flat plate (for large time). Schuh (19) developed a general method, based on the integral momentum equation, for the approximate calculation of unsteady boundary layers. Results of the particular cases considered in Schuh's work were in agreement with available exact solutions. It was also shown in the general case, for an arbitrary velocity distribution in time and space, outside the boundary layer, that the integral momentum equation could be reduced to two simultaneous differential

equations that could be solved by the method of characteristics.

In the present investigation the unsteady entrance velocity was determined indirectly using unsteady pressure gradients measured in the fully developed region. There are several publications in which discharge and the corresponding unsteady pressure gradients for fully developed flows are discussed. Ito (12), using methods of operational calculus, determined expressions for the velocity distribution and discharge for various types of non-steady pressure gradients. Szymanski (23) solved the Navier-Stokes equations for flow of a fluid started from rest in an infinitely long circular tube under a constant pressure gradient. Gerbes (6) by means of Laplace transformation solved the Navier-Stokes equations for flow in a long circular tube with sudden application of a constant pressure gradient, with sudden removal of the constant pressure gradient, and with an oscillating pressure gradient. Rogge and Young (16) presented a general method for obtaining an exact solution of the Navier-Stokes equations for time-dependent flow in parallel plate channels and circular tubes, given the discharge as a prescribed function of time. An approximate solution, valid for small times, was also obtained using the integral momentum equation. For both the cases of constant discharge and linearly accelerated flow the exact and approximate solutions were in good

agreement.

It was apparent from the review of literature that the use of the momentum equation for the study of unsteady flow problems was feasible but had not received much attention.

III. EQUATIONS AND METHOD OF SOLUTION

A. Derivation of the Governing Equation

The general integral momentum equation applied to a control volume is

$$\int_{\mathcal{V}} \frac{\partial \rho \bar{v}}{\partial t} \, d\mathcal{V} + \int_{S} \rho \bar{v}(\bar{n} \cdot \bar{v}) dS = \Sigma \bar{F} \qquad (1)$$

where

t = time

$\bar{v}$ = velocity vector

$\bar{n}$ = unit vector normal to the surface of the control volume

dS = surface element of the area enclosing the control volume

$d\mathcal{V}$ = volume element of the control volume

ρ = density of the fluid

$\Sigma \bar{F}$ = vector sum of all forces acting on the control volume

Consider an element of fluid in the entrance region of a circular tube (Figure 2). Application of the momentum integral equation to this element in the axial direction gives

$$\left[\int_0^R \frac{\partial(\rho u)}{\partial t} \, 2\pi r dr\right] dx - \int_0^R \rho u^2 2\pi r dr + \int_0^R \rho \left(u + \frac{\partial u}{\partial x} dx\right)^2 2\pi r dr$$

$$= -\tau_\omega \, 2\pi R dx - \sigma \int_0^R 2\pi r dr + \left(\sigma + \frac{\partial \sigma}{\partial x} dx\right) \int_0^R 2\pi r dr \qquad (2)$$

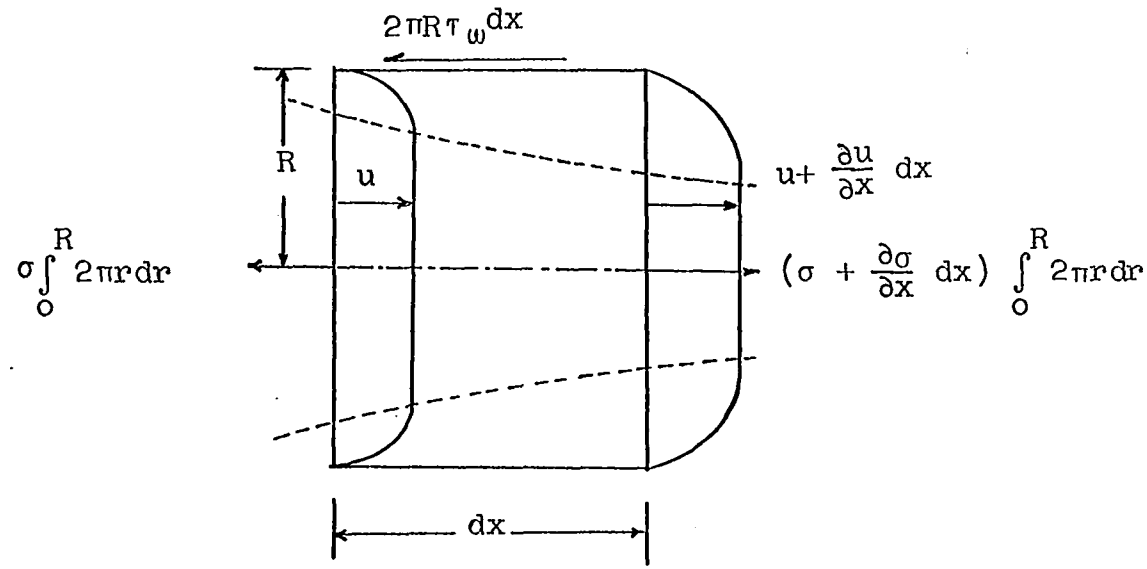

Fig. 2. Control volume in the entrance region for momentum analysis.

where

u = velocity in the axial direction

τ_ω = wall shear stress

R = radius of the tube

σ = normal stress in the axial direction, assumed constant over the cross-section of the tube

In Equation 2 the quantity $(\frac{\partial u}{\partial x}\, dx)^2$ is neglected in comparison with u^2 and $2u\,\frac{\partial u}{\partial x}\, dx$. On dividing by $2\pi\rho dx$ and simplifying we obtain, for an incompressible fluid,

$$\int_0^R \frac{\partial u}{\partial t}\, r dr + \int_0^R 2u\,\frac{\partial u}{\partial x}\, r dr = -\frac{\tau_\omega R}{\rho} + \frac{1}{\rho}\,\frac{\partial \sigma}{\partial x}\int_0^R r dr \qquad (3)$$

With the transformation

$$r = R - y$$

$$dr = -dy \qquad (4)$$

where y is defined as shown in Figure 1-a, Equation 3 can be written as

$$\int_0^R \frac{\partial u}{\partial t}\,(R-y)dy + \int_0^R 2u\,\frac{\partial u}{\partial x}\,(R-y)dy = -\frac{\tau_\omega R}{\rho} + \frac{1}{\rho}\,\frac{\partial \sigma}{\partial x}\int_0^R (R-y)dy \qquad (5)$$

For an incompressible fluid, the normal stress and velocity gradient in the axial direction are related by the equation

$$\sigma = -p + 2\mu\,\frac{\partial u}{\partial x}$$

where

p = pressure (average normal stress)

μ = absolute viscosity of the fluid

Thus,

$$\frac{\partial \sigma}{\partial x} = - \frac{\partial p}{\partial x} + 2\mu \frac{\partial^2 u}{\partial x^2}$$

In the inviscid core of the entrance region, where the viscosity is assumed to be zero,

$$\frac{\partial \sigma}{\partial x} \equiv - \frac{\partial p}{\partial x}$$

And, in the boundary layer $\partial^2 u/\partial x^2$ is usually neglected. Thus, for the entire cross-section, we can take

$$\frac{\partial \sigma}{\partial x} = - \frac{\partial p}{\partial x} \tag{6}$$

From Equations 5 and 6 we obtain

$$\int_0^R \frac{\partial u}{\partial t} (R-y)dy + \int_0^R 2u \frac{\partial u}{\partial x} (R-y)dy = - \frac{\tau_\omega R}{\rho} - \frac{1}{\rho} \frac{\partial p}{\partial x} \int_0^R (R-y)dy \tag{7}$$

In the analysis that follows, the following assumptions are made with respect to the inviscid core model considered:

(1) The entrance velocity, which is a function of time, is uniform over the entire cross-section of the tube at the inlet, that is, at $x = 0$.

(2) The velocity in the inviscid core is uniform over the cross section of the core. That is, the radial component of the fluid velocity is zero in the inviscid core. Let the core velocity be u_1.

(3) As noted earlier, the pressure variation within the boundary layer in the radial direction is negligible in comparison with that in the axial direction. This leads to the conclusion that the

axial pressure-gradient in the entire fluid is the same as the axial pressure-gradient in the inviscid core. Since the viscosity and the radial velocity are zero in the inviscid core this assumption reduces the Navier-Stokes equation for velocity u_1 within the core to

$$\frac{\partial u_1}{\partial t} + u_1 \frac{\partial u_1}{\partial x} = - \frac{1}{\rho} \frac{\partial p}{\partial x} \tag{8}$$

(4) The fluid is Newtonian.

(5) The velocity profiles in the boundary layer are similar and the dimensionless velocity profiles can be expressed as

$$\frac{u}{u_1} = 2 \frac{y}{\delta} - \frac{y^2}{\delta^2} \tag{9}$$

where δ is the boundary layer thickness.

From Equations 7 and 8 we have

$$\int_0^R \frac{\partial u}{\partial t} (R-y)dy + \int_0^R 2u \frac{\partial u}{\partial x}(R-y)dy = - \frac{\tau_w R}{\rho} + \int_0^R \frac{\partial u_1}{\partial t} (R-y)dy + \int_0^R u_1 \frac{\partial u_1}{\partial x} (R-y)dy$$

By rearranging the terms we obtain

$$- \frac{\tau_w R}{\rho} = \int_0^R \frac{\partial}{\partial t} (u-u_1)(R-y)dy + \int_0^R \frac{\partial u^2}{\partial x}(R-y)dy - \int_0^R u_1 \frac{\partial u_1}{\partial x}(R-y)dy$$

To the right hand side let us add and subtract the term $\int_0^R u \frac{\partial u_1}{\partial x}(1- \frac{y}{R})dy$ and simplify. Observing that $\int \frac{\partial}{\partial x}(uu_1)(1- \frac{y}{R})dy = \int u \frac{\partial u_1}{\partial x}(1- \frac{y}{R})dy + \int u_1 \frac{\partial u}{\partial x}(1- \frac{y}{R})dy$ we can further write

$$\frac{\tau_\omega}{\rho} = \frac{\partial}{\partial t}\int_0^R (u_1-u)\left(1-\frac{y}{R}\right)dy + \int_0^R \frac{\partial}{\partial x}(uu_1)\left(1-\frac{y}{R}\right)dy - \int_0^R \frac{\partial u^2}{\partial x}\left(1-\frac{y}{R}\right)dy$$

$$+ \int_0^R \frac{\partial u_1}{\partial x}(u_1-u)\left(1-\frac{y}{R}\right)dy - \int_0^R u_1\frac{\partial u}{\partial x}\left(1-\frac{y}{R}\right)dy$$

Since u_1 is not a function of y we can write

$$\frac{\tau_\omega}{\rho} = \frac{\partial}{\partial t}\left\{u_1\int_0^R\left(1-\frac{u}{u_1}\right)\left(1-\frac{y}{R}\right)dy\right\} + \frac{\partial}{\partial x}\left\{u_1^2\int_0^R\frac{u}{u_1}\left(1-\frac{u}{u_1}\right)\left(1-\frac{y}{R}\right)dy\right\}$$

$$+ u_1\frac{\partial u_1}{\partial x}\int_0^R\left(1-\frac{u}{u_1}\right)\left(1-\frac{y}{R}\right)dy - u_1\int_0^R\frac{\partial u}{\partial x}\left(1-\frac{y}{R}\right)dy \qquad (10)$$

The last term in Equation 10 can be proved to be zero through the equation of continuity. For axi-symmetric flow the equation of continuity is

$$\frac{\partial}{\partial x}(ur) + \frac{\partial}{\partial r}(vr) = 0$$

or,
$$\frac{\partial}{\partial x}(ur) = -\frac{\partial}{\partial r}(vr) \qquad (11)$$

where v is the radial velocity. From Equations 4 and 11,

$$\int_0^R \frac{\partial u}{\partial x}\left(1-\frac{y}{R}\right)dy = -\int_0^R \frac{\partial}{\partial x}\left(u\frac{r}{R}\right)dr$$

$$= \frac{1}{R}\int_0^R \frac{\partial}{\partial r}(vr)dr$$

$$= \frac{1}{R}\int_0^R d(vr) = \frac{1}{R}\left\{vr\,\Big|_0^R\right\}$$

$$= \frac{1}{R}\left\{(vr)_{r=R} - (vr)_{r=0}\right\} = 0 \qquad (12)$$

Further, in boundary layer theory, for axi-symmetric flow,

the quantities $\int_0^R (1- \frac{u}{u_1})(1- \frac{y}{R})dy$ and $\int_0^R \frac{u}{u_1}(1- \frac{u}{u_1})(1- \frac{y}{R})dy$ are defined as the displacement thickness and momentum thickness, respectively. The displacement thickness is the distance by which the irrotational core is displaced toward the center of the tube due to the decrease in velocity in the boundary layer, and the momentum thickness is that distance within which the momentum, if the flow is irrotational, is equivalent to the momentum loss in the boundary layer. Let the displacement thickness be

$$\int_0^R (1- \frac{u}{u_1})(1- \frac{y}{R})dy = \delta^* \tag{13}$$

and the momentum thickness

$$\int_0^R \frac{u}{u_1} (1- \frac{u}{u_1})(1- \frac{y}{R})dy = \theta \tag{14}$$

With Equations 12, 13, and 14 in Equation 10 we can write

$$\frac{\tau_\omega}{\rho} = \frac{\partial}{\partial t} (u_1 \delta^*) + \frac{\partial}{\partial x} (u_1^2 \theta) + u_1 \frac{\partial u_1}{\partial x} \delta^* \tag{15}$$

Differentiation of the second term on the right hand side and division throughout by u_1^2 gives

$$\frac{\tau_\omega}{\rho u_1^2} = \frac{1}{u_1^2} \frac{\partial}{\partial t} (u_1 \delta^*) + \frac{1}{u_1} \frac{\partial u_1}{\partial x}(\delta^* + 2\theta) + \frac{\partial \theta}{\partial x} \tag{16}$$

With the parabolic velocity profile $\frac{u}{u_1} = 2 \frac{y}{\delta} - \frac{y^2}{\delta^2}$ the quantities δ^* and θ can be evaluated. Since $\frac{u}{u_1} = 1$ for $R \geq y \geq \delta$ we can write

$$\delta^* = \int_0^R (1-\frac{u}{u_1})(1-\frac{y}{R})dy = \int_0^\delta (1-\frac{u}{u_1})(1-\frac{y}{R})dy$$

$$= \int_0^\delta (1-2\frac{y}{\delta}+\frac{y^2}{\delta^2})(1-\frac{y}{R})dy = \frac{1}{3}\delta - \frac{1}{12}\frac{\delta^2}{R} \qquad (17)$$

$$\theta = \int_0^R \frac{u}{u_1}(1-\frac{u}{u_1})(1-\frac{y}{R})dy = \int_0^\delta \frac{u}{u_1}(1-\frac{u}{u_1})(1-\frac{y}{R})dy$$

$$= \int_0^\delta (2\frac{y}{\delta}-\frac{y^2}{\delta^2})(1-2\frac{y}{\delta}+\frac{y^2}{\delta^2})(1-\frac{y}{R})dy = \frac{2}{15}\delta - \frac{1}{20}\frac{\delta^2}{R} \qquad (18)$$

and $$\delta^* + 2\theta = \frac{3}{5}\delta - \frac{11}{60}\frac{\delta^2}{R}$$

Also, $$\frac{\tau_\omega}{\rho} = \frac{\mu(\frac{\partial u}{\partial y})_{y=0}}{\rho} = \nu(\frac{\partial u}{\partial y})_{y=0}$$

$$= \nu[\frac{\partial}{\partial y}\{u_1(2\frac{y}{\delta}-\frac{y^2}{\delta^2})\}]_{y=0} = \frac{2\nu u_1}{\delta} \qquad (19)$$

Substitution for $\frac{\tau_\omega}{\rho}$, δ^* and θ into Equation 16 gives

$$\frac{2\nu}{\delta u_1} = \frac{1}{u_1^2}\frac{\partial}{\partial t}\{u_1(\frac{1}{3}\delta - \frac{1}{12}\frac{\delta^2}{R})\} + \frac{1}{u_1}\frac{\partial u_1}{\partial x}(\frac{3}{5}\delta - \frac{11}{60}\frac{\delta^2}{R}) +$$

$$\frac{\partial}{\partial x}(\frac{2}{15}\delta - \frac{1}{20}\frac{\delta^2}{R}) \qquad (20)$$

We can obtain a relation between the inlet velocity u_o (Figure 1-b) and the core velocity u_1 by applying the principle of conservation of mass for the fluid between the inlet and any downstream position. The principle of conservation of mass gives

$$\pi R^2 u_o = \pi(R-\delta)^2 u_1 + \int_{R-\delta}^R 2\pi r u dr$$

$$= \pi(R-\delta)^2 u_1 + \int_0^\delta 2\pi(R-y)u dy$$

Replacement of u in the integral by the parabolic velocity profile results in $\pi R2u_o = \pi(R-\delta)^2u_1 + \int_o^\delta 2\pi(R-y)u_1(2\frac{y}{\delta} - \frac{y^2}{\delta^2})dy$

or, $\pi R^2u_o = \pi(R-\delta)^2u_1 + 2\pi u_1 (\frac{2}{3} R\delta - \frac{5}{12} \delta^2)$

Simplification of the above equation yields

$$\frac{u_o}{u_1} = 1 - \frac{2}{3}\frac{\delta}{R} + \frac{1}{6}\frac{\delta^2}{R^2} \qquad (21)$$

or, $$u_1 = \frac{u_o}{1- \frac{2}{3}\frac{\delta}{R} + \frac{1}{6}\frac{\delta^2}{R^2}}$$

With the use of u_1 Equation 20 can be written as

$$\frac{2\nu}{\delta u_o}(1- \frac{2\delta}{3R} + \frac{1}{6}\frac{\delta^2}{R^2}) = \frac{(1- \frac{2}{3}\frac{\delta}{R} + \frac{1}{6}\frac{\delta^2}{R^2})^2}{u_o^2} \frac{\partial}{\partial t} \{\frac{u_o(\frac{1}{3}\delta - \frac{1}{12}\frac{\delta^2}{R})}{1- \frac{2}{3}\frac{\delta}{R} + \frac{1}{6}\frac{\delta^2}{R^2}}\}$$

$$+ \frac{(1- \frac{2}{3}\frac{\delta}{R} + \frac{1}{6}\frac{\delta^2}{R^2})}{u_o}\{\frac{\partial}{\partial x}(1- \frac{2}{3}\frac{\delta}{R} + \frac{1}{6}\frac{\delta^2}{R^2})\}(\frac{3}{5}\delta - \frac{11}{60}\frac{\delta^2}{R})$$

$$+ \frac{\partial}{\partial x}(\frac{2}{15}\delta - \frac{1}{20}\frac{\delta^2}{R}) \qquad (22)$$

On simplification Equation 22 is reduced to

$$\frac{2\nu}{\delta u_o}(1- \frac{2}{3}\frac{\delta}{R} + \frac{1}{6}\frac{\delta^2}{R^2})^2 = \frac{R}{u_o^2}(\frac{1}{3}\frac{\delta}{R} - \frac{1}{12}\frac{\delta^2}{R^2})(1- \frac{2}{3}\frac{\delta}{R} + \frac{1}{6}\frac{\delta^2}{R^2})\frac{\partial u_o}{\partial t}$$

$$+ \frac{1}{u_o}(\frac{1}{3} - \frac{1}{6}\frac{\delta}{R})(1- \frac{2}{3}\frac{\delta}{R} + \frac{1}{6}\frac{\delta^2}{R^2})\frac{\partial \delta}{\partial t}$$

$$+ 2[(\frac{3}{5}\frac{\delta}{R} - \frac{11}{60}\frac{\delta^2}{R^2})(\frac{1}{3} - \frac{1}{6}\frac{\delta}{R}) + (\frac{1}{15} - \frac{1}{20}\frac{\delta}{R})(1- \frac{2}{3}$$

$$+ \frac{1}{6}\frac{\delta^2}{R^2})]\frac{\partial \delta}{\partial x} \qquad (23)$$

The pertinent initial and boundary conditions are:

$$\delta = 0 \quad \text{at } t = 0 \quad \text{for } x \geq 0$$

$$\delta = 0 \quad \text{at } x = 0 \quad \text{for } t \geq 0$$

Let us define the dimensionless variables ξ, η, τ and u_o^* by the relations

$$\xi = x/R$$

$$\eta = \delta/R$$

$$\tau = tU/R \text{ and,}$$

$$u_o^* = u_o/U$$

where U = steady state average velocity. Equation 23 in terms of the above dimensionless variables becomes

$$\frac{2\nu}{R\eta U u_o^*}\left(1-\frac{2}{3}\eta+\frac{1}{6}\eta^2\right)^2-\frac{1}{u_o^{*2}}\left(\frac{1}{3}\eta-\frac{1}{12}\eta^2\right)\left(1-\frac{2}{3}\eta+\frac{1}{6}\eta^2\right)^2\frac{\partial u_o^*}{\partial\tau}$$

$$=\frac{1}{u_o^*}\left(\frac{1}{3}-\frac{1}{6}\eta\right)\left(1-\frac{2}{3}\eta+\frac{1}{6}\eta^2\right)\frac{\partial\eta}{\partial\tau}$$

$$+2\left[\left(\frac{3}{5}\eta-\frac{11}{60}\eta^2\right)\left(\frac{1}{3}-\frac{1}{6}\eta\right)+\left(\frac{1}{15}-\frac{1}{20}\eta\right)\left(1-\frac{2}{3}\eta+\frac{1}{6}\eta^2\right)\right]\frac{\partial\eta}{\partial\xi} \tag{24}$$

The corresponding initial and boundary conditions in terms of the new variables are:

$$\eta = 0 \quad \text{at } \tau = 0 \quad \text{for } \xi \geq 0$$

$$\eta = 0 \quad \text{at } \xi = 0 \quad \text{for } \tau \geq 0 \tag{25}$$

B. Method of Solution

Equation 24 is a quasi-linear partial differential equation of the first order of the type

$$P(\xi,\tau,\eta)\,\frac{\partial\eta}{\partial\xi} + Q(\xi,\tau,\eta)\,\frac{\partial\eta}{\partial\tau} = R(\xi,\tau,\eta) \tag{26}$$

and its solution, as shown by Sneddon (21), is obtained by integrating the system of ordinary differential equations chosen from the auxiliary system

$$\frac{d\xi}{P} = \frac{d\tau}{Q} = \frac{d\eta}{R} \tag{27}$$

There are two independent ordinary differential equations in the system 27. Each ordinary differential equation has solutions represented by a one-parameter family of curves, which are called characteristics of the first order quasi-linear partial differential equation. The characteristics comprising a one-parameter family of solutions of Equations 27 generate the surface $\eta = \eta(\xi,\tau)$, which is the solution of the Equation 26. Following this well-known method of solution the auxiliary system associated with Equation 24 can be written as

$$\frac{d\xi}{2\left[\left(\frac{3}{5}\eta - \frac{11}{60}\eta^2\right)\left(\frac{1}{3} - \frac{1}{6}\eta\right) + \left(\frac{1}{15} - \frac{1}{20}\eta\right)\left(1 - \frac{2}{3}\eta + \frac{1}{6}\eta^2\right)\right]}$$

$$= \frac{d\tau}{\frac{1}{u_o^*}\left(\frac{1}{3} - \frac{1}{6}\eta\right)\left(1 - \frac{2}{3}\eta + \frac{1}{6}\eta^2\right)} \tag{28}$$

$$= \frac{d\eta}{\frac{2\nu}{R\eta U u_o^*}\left(1 - \frac{2}{3}\eta + \frac{1}{6}\eta^2\right)^2 - \frac{1}{u_o^{*2}}\left(\frac{1}{3}\eta - \frac{1}{12}\eta^2\right)\left(1 - \frac{2}{3}\eta + \frac{1}{6}\eta^2\right)^2 \frac{\partial u_o^*}{\partial\tau}}$$

In the following, Equation 28 in conjunction with the appropriate initial and boundary conditions is solved (i) for constant entrance velocity, i.e., for $u_o^* = 1$; which implies that the entrance velocity u_o has reached the value of the steady state velocity U for $t \geq 0$, and (ii) for a time-dependent entrance velocity derived from unsteady pressure gradients measured in the fully-developed flow region.

1. Solution for constant entrance velocity

For $u_o^* = 1$ the system of ordinary differential equations, given by Equation 28, becomes

$$\frac{d\xi}{2[(\frac{3}{5}\eta - \frac{11}{60}\eta^2)(\frac{1}{3} - \frac{1}{6}\eta) + (\frac{1}{15} - \frac{1}{20}\eta)(1 - \frac{2}{3}\eta + \frac{1}{6}\eta^2)]} = \frac{d\tau}{(\frac{1}{3} - \frac{1}{6}\eta)(1 - \frac{2}{3}\eta + \frac{1}{6}\eta^2)} = \frac{d\eta}{\frac{2\nu}{R\eta U}(1 - \frac{2}{3}\eta + \frac{1}{6}\eta^2)^2} \tag{29}$$

Two independent ordinary differential equations can now be written:

$$d\tau = \frac{\frac{RU}{2\nu}(\frac{1}{3}\eta - \frac{1}{6}\eta^2)}{1 - \frac{2}{3}\eta + \frac{1}{6}\eta^2} d\eta \tag{30}$$

$$d\xi = \frac{\frac{RU}{\nu}[(\frac{3}{5}\eta - \frac{11}{60}\eta^2)(\frac{1}{3}\eta - \frac{1}{6}\eta^2) + (\frac{1}{15}\eta - \frac{1}{20}\eta^2)(1 - \frac{2}{3}\eta + \frac{1}{6}\eta^2)]}{(1 - \frac{2}{3}\eta + \frac{1}{6}\eta^2)^2} d\eta \tag{31}$$

Integration of Equation 30 between the limits 0 and τ in conjunction with the initial condition $\eta = 0$ at $\tau = 0$ for $\xi \geq 0$ gives

$$\tau = \frac{RU}{\nu}\{-\frac{\eta}{2} - \frac{1}{2}\ln(1 - \frac{2}{3}\eta + \frac{1}{6}\eta^2) + \frac{1}{\sqrt{2}}\tan^{-1}(\frac{\eta - 2}{\sqrt{2}}) - \frac{1}{\sqrt{2}}\tan^{-1}(-\sqrt{2})\} \tag{32}$$

Integration of Equation 31 between the limits 0 and ξ using the boundary condition

$\eta = 0$ at $\xi = 0$ and $\tau \geq 0$ gives

$$\xi = \frac{RU}{\nu}\{-\frac{3}{10}\eta+(\frac{\frac{11}{60}\eta^3-\frac{31}{20}\eta+\frac{24}{5}}{1-\frac{2}{3}\eta+\frac{1}{6}\eta^2})+\frac{11}{10}\ln(1-\frac{2}{3}\eta+\frac{1}{6}\eta^2)$$

$$-\frac{37\sqrt{2}}{20}\tan^{-1}(\frac{\eta-2}{\sqrt{2}})+\frac{37\sqrt{2}}{20}\tan^{-1}(-\sqrt{2})-\frac{24}{5}\} \qquad (33)$$

Defining the Reynolds number as $Re = 2RU/\nu$, we may replace the quantity RU/ν by $Re/2$ in the above equations. It can be observed in Equations 32 and 33 that the dimensionless boundary layer thickness η is not obtained explicitly as a function of τ and as a function of ξ. However, the η-τ, η-ξ relationships are expressed graphically by plotting τ and ξ for various values of η (see Figures 3 and 4). The value of η may vary from 0 to 1 since this is the range of interest, in the sense that at $\eta = 1$ the boundary layer thickness is equal to the radius of the tube at which time the flow is considered to have attained the fully-developed state. Treating η as a parameter, ξ and τ are related through the parameter η, and the characteristic through the origin on the ξ-τ plane is plotted. This characteristic divides the ξ-τ plane into two regions which are designated as Region I and Region II (Figure 5). Region I is the range of influence of the initial curve $\xi = 0$ (the τ-axis along which $\tau \geq 0$), and Equation 33 which is valid for $\tau \geq 0$ gives the appropriate

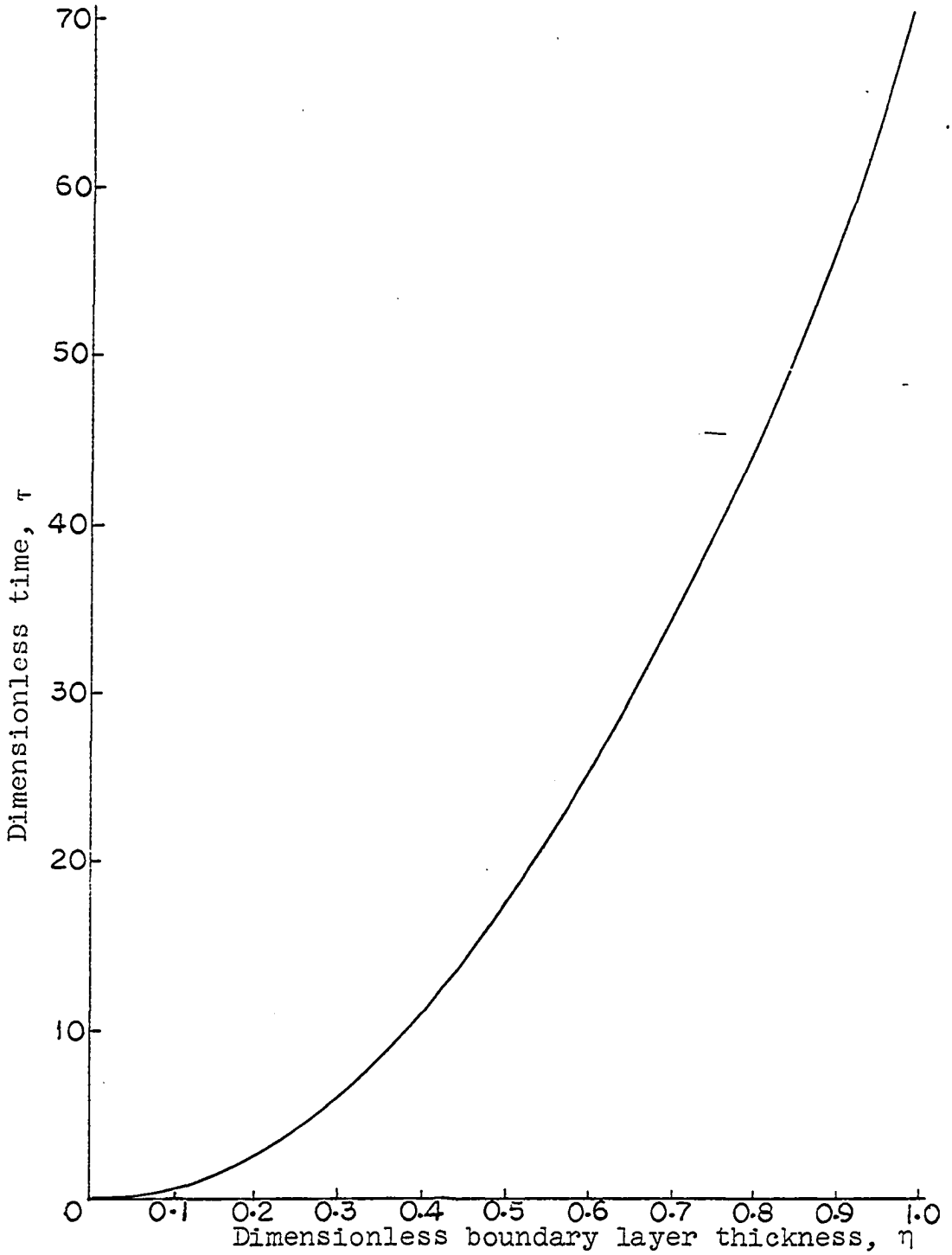

Fig. 3. Variation of boundary layer thickness with time. Constant entrance velocity. Re = 1610.

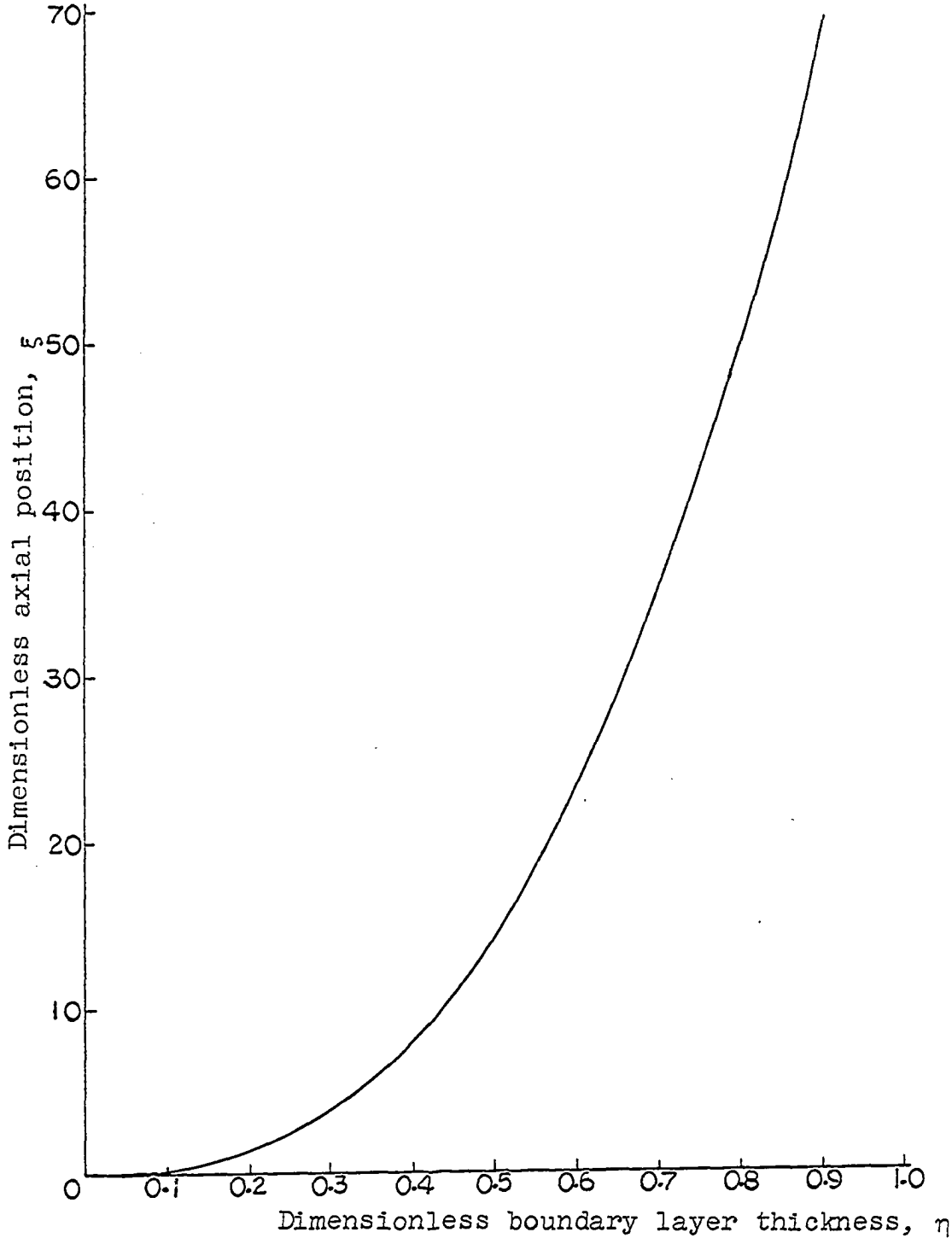

Fig. 4. Variation of boundary layer thickness with axial position. Constant entrance velocity. Re = 1610.

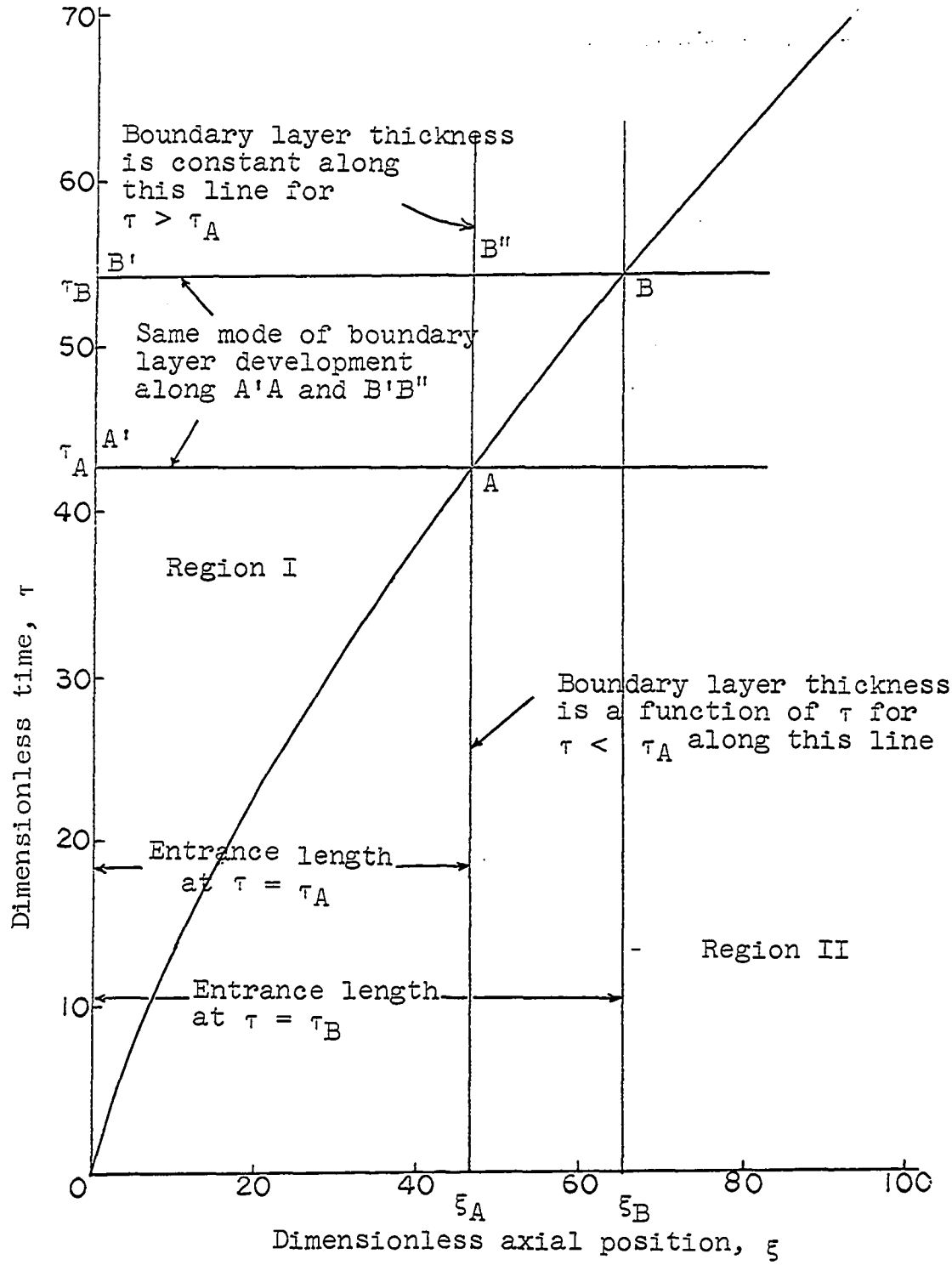

Fig. 5. Characteristic in the ξ-τ space. Nature of the boundary layer growth in Region I and in Region II. Re = 1610.

solution in this region. It can be seen from Equation 33 that the boundary layer thickness, η, is independent of τ, and is a function of ξ alone. This means that at any axial position in Region I the boundary layer thickness developed is constant for all τ. The limiting value of ξ, for which the boundary layer thickness is a function only of the axial position, is determined by the ξ-coordinate corresponding to the τ in question on the ξ-τ characteristic of Figure 5. This value of ξ corresponds to the instantaneous dimensionless entrance length. The boundary layer thickness for various values of ξ (and τ) in Region I are determined from Figure 4.

Region II is the range of influence of the initial curve $\tau = 0$ (the ξ-axis along which $\xi \geq 0$). Equation 32, which is valid for $\xi \geq 0$, gives the appropriate solution in this region. The boundary layer thickness, as can be seen in Equation 32, is independent of ξ, and is a function of τ alone. That is, at any particular time the boundary layer thickness is constant for all axial positions beyond the value of ξ determined from the ξ-τ characteristic, as described above. The boundary layer thicknesses at various τ in Region II are determined from Figure 3.

Figure 5 illustrates the nature of the boundary layer growth at any τ and at any ξ. Suppose the modes of the boundary layer growth at $\tau = \tau_A$ and at $\tau = \tau_B$ are required. The lines $\tau = \tau_A$ and $\tau = \tau_B$ intersect the characteristic at

A and B respectively. The axial positions ξ_A and ξ_B are the respective entrance lengths corresponding to τ_A and τ_B. Along the straight line $\tau = \tau_A$ the boundary layer thickness is a function of ξ over the portion A'A (in Region I) and is constant for $\xi >$ A'A (in Region II). In the same manner, along the straight line $\tau = \tau_B$ the boundary layer thickness is a function of ξ over the portion B'B (in Region I) and is constant for $\xi >$ B'B (in Region II). Now, let us consider the boundary layer growth along the straight line $\xi = \xi_A$. Along the line $\xi = \xi_A$ the boundary layer thickness is a constant over the portion AB" (in Region I). That is, η is constant along this line for $\tau > \tau_A$. For $\tau < \tau_A$, in Region II, the boundary layer thickness is a function of time. Since in Region I, the boundary layer thickness is constant, at any axial position, for all τ the axial dependence of the boundary layer thickness is the same over the portions A'A and B'B". This means that the boundary layer development at $\tau = \tau_B$ is the same as that for the boundary layer at $\tau = \tau_A$ up to an axial length $\xi = \xi_A$. Similar patterns of boundary layer growth can be observed for all time. A sketch of the boundary layer development in the entrance region, as determined by the Equations 32 and 33, for the case of constant entrance velocity is shown in Figure 6. Although the solution for η, as presented in Equations 32 and 33, is not obtained explicitly as a function

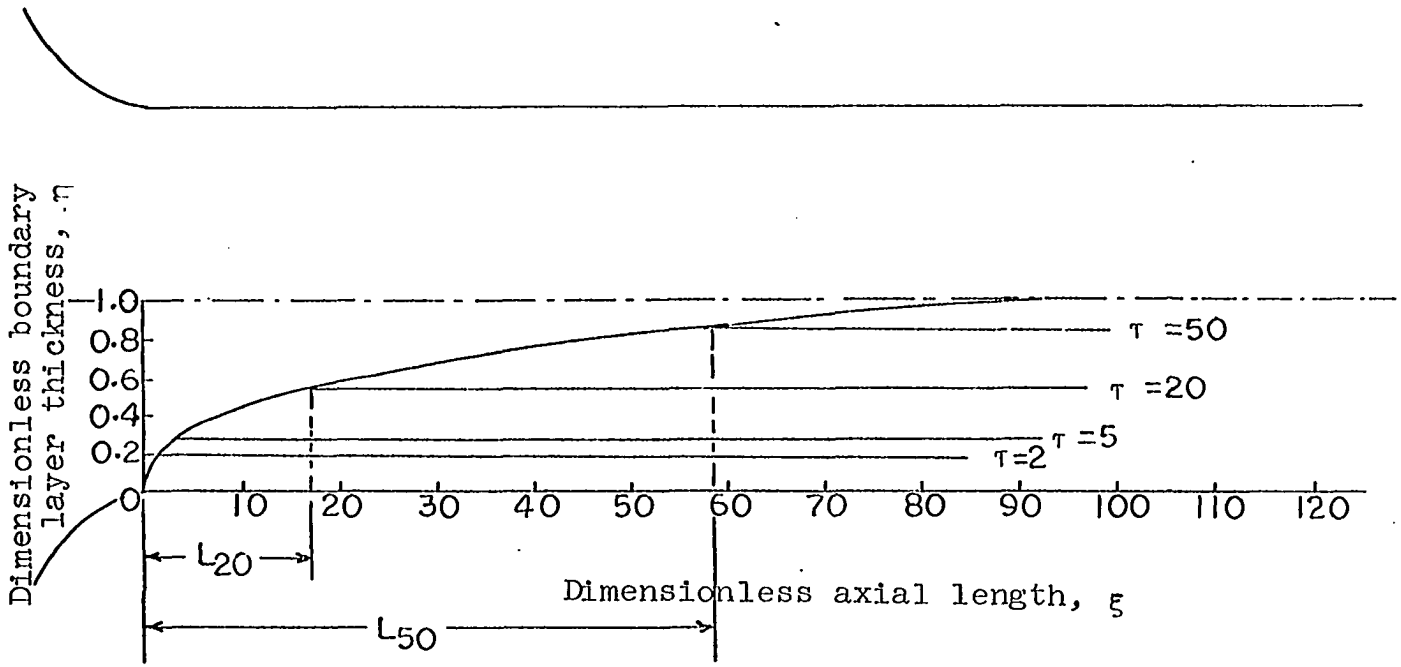

Fig. 6. Mode of unsteady boundary layer development in the entrance region with constant entrance velocity. Re = 1610. L_{20} and L_{50} are entrance lengths at τ = 20 and 50, respectively.

of ξ and τ it is a closed form solution.

In computing ξ and τ (Figures 3, 4, and 5) a Reynolds number of 1610 was used. The reason for using this number is convenience from the point of the experiment designed to produce this number based on a steady state velocity. A detailed description of the experiment is given in the next chapter.

For the case of a time-dependent velocity at the inlet, Equation 24 does not yield a closed form solution because of the coupling of the η and τ functions. A computer method involving a numerical technique according to Runge-Kutta-Gill (7) is employed to solve this problem, as described in the next section.

The main purpose for obtaining the solution for the constant entrance velocity was to establish some level of confidence in the computer program for the solution of the more general problem with a time-dependent entrance velocity. Before making this comparison a discussion of the time-dependent entrance velocity problem will be given.

2. Solution for time-dependent entrance velocity

Consider once again Equations 26 and 27. Let us seek a solution of 26 passing through a prescribed initial curve

$$\xi = \xi(r), \quad \tau = \tau(r), \quad \eta = \eta(r) \tag{34}$$

in space. Garabedian (5) has shown that this problem can be solved by considering for each value of r the integral curve

of the auxiliary system 27 with initial values defined by Equation 34. If we now introduce a parameter, s, along these integral curves we obtain a surface

$$\xi = \xi(s,r), \quad \tau = \tau(s,r), \quad \eta = \eta(s,r) \tag{35}$$

in parametric form. If we represent η as $\eta(\xi,\tau)$ in Equation 35, which we can, this should yield the solution of Equation 26 passing through the initial curve given by Equations 34. Then the system of Equations 27 can be replaced by the system

$$\frac{d\xi}{ds} = P(\xi,\tau,\eta), \quad \frac{d\tau}{ds} = Q(\xi,\tau,\eta), \quad \frac{d\eta}{ds} = R(\xi,\tau,\eta) \tag{36}$$

where the parameter s plays the role of an independent variable.

In accord with the above theory we can replace the system of Equations 28 by the system

$$\begin{aligned}
\frac{d\xi}{ds} &= 2\left[\left(\frac{3}{5}\eta - \frac{11}{60}\eta^2\right)\left(\frac{1}{3} - \frac{1}{6}\eta\right) + \left(\frac{1}{15} - \frac{1}{20}\eta\right)\left(1 - \frac{2}{3}\eta + \frac{1}{6}\eta^2\right)\right]\eta u_o^{*2} \\
\frac{d\eta}{ds} &= \frac{4}{Re}\, u_o^*\left(1 - \frac{2}{3}\eta + \frac{1}{6}\eta^2\right)^2 - \eta\left(\frac{1}{3}\eta - \frac{1}{12}\eta^2\right)\left(1 - \frac{2}{3}\eta + \frac{1}{6}\eta^2\right)^2 \frac{du_o^*}{d\tau} \\
\frac{d\tau}{ds} &= u_o^*\eta\left(\frac{1}{3} - \frac{1}{6}\eta\right)\left(1 - \frac{2}{3}\eta + \frac{1}{6}\eta^2\right)
\end{aligned} \tag{37}$$

Now we have a system of ordinary differential equations for which we seek the solution passing through the initial curve

$$\begin{aligned}
\xi &= 0, \quad \eta = 0 \\
\tau &= 0, \quad \eta = 0
\end{aligned} \tag{38}$$

It was not possible to obtain a closed form solution of Equations 37 because of the coupling of η and τ functions on the right hand side. Therefore we considered a numerical

solution employing a step-by-step integration procedure. A computer program called NODE, available in the Computer Science Library of Iowa State University, was used to solve Equations 37. The NODE program makes use of R. L. Crane's predictor-corrector procedure with the starting process due to Runge-Kutta-Gill, and is available in FORTRAN version for the IBM 360 system. The listing of the main program and the subroutines associated with NODE are presented in Appendix A. The solution of Equations 37 for the time-dependent entrance velocity problem is presented in Chapter VI.

To establish some level of confidence in the computer program, the previously described problem of constant entrance velocity is considered, and the results are compared with those given by the closed form solution.

3. Comparison of the closed form solution and the computer solution for the case of constant entrance velocity

For the case $u_o^* = 1$, the set of Equations 37 become

$$\frac{d\varepsilon}{ds} = 2\left[\left(\frac{3}{5}\eta - \frac{11}{60}\eta^2\right)\left(\frac{1}{3} - \frac{1}{6}\eta\right) + \left(\frac{1}{15} - \frac{1}{20}\eta\right)\left(1 - \frac{2}{3}\eta + \frac{1}{6}\eta^2\right)\right]\eta$$

$$\frac{d\eta}{ds} = \frac{4}{Re}\left(1 - \frac{2}{3}\eta + \frac{1}{6}\eta^2\right)^2 \qquad (39)$$

$$\frac{d\tau}{ds} = \eta\left(\frac{1}{3} - \frac{1}{6}\eta\right)\left(1 - \frac{2}{3}\eta + \frac{1}{6}\eta^2\right)$$

The appropriate initial and boundary conditions remain the same as in Equation 38. The Reynolds number used in Equations 39 is 1610. After integration of the set of Equations 39 with the NODE subroutine, we can construct a

family of characteristics in ξ-τ space by treating η as a parameter. Such a family of characteristics, mechanically plotted by incorporating the Simplotter (GRAPH) subroutine into the NODE program, is shown in Figure 7.

With reference to Figure 7, the space above the characteristic through the origin is Region I and the space below is Region II as defined earlier.

For values of η from the computer solution the corresponding ξ and τ can be computed from the closed form solution given in Equations 32 and 33, and compared with ξ and τ of the computer solution. The validity of the computer program can then be evaluated by considering the agreement between the computer solution and the closed form solution for ξ and τ. Table 1 illustrates the good agreement for various values of η.

Table 1. Comparison of computer solution and closed form solution for the case of constant entrance velocity

η	ξ		τ	
	computer solution	closed form solution	computer solution	closed form solution
0.0773	0.1849	0.1842	0.4039	0.4041
0.1131	0.4216	0.4206	0.8683	0.8685
0.2111	1.7233	1.7235	3.0554	3.0555
0.3241	4.7967	4.7966	7.2729	7.2731
0.4217	9.2567	9.2569	12.4024	12.4027
0.5075	14.9143	14.9141	18.0572	18.0580
0.6194	25.2422	25.2435	27.0275	27.0283
0.7161	37.2935	37.2963	36.1880	36.1889
0.8526	60.0134	60.0187	51.2461	51.2480

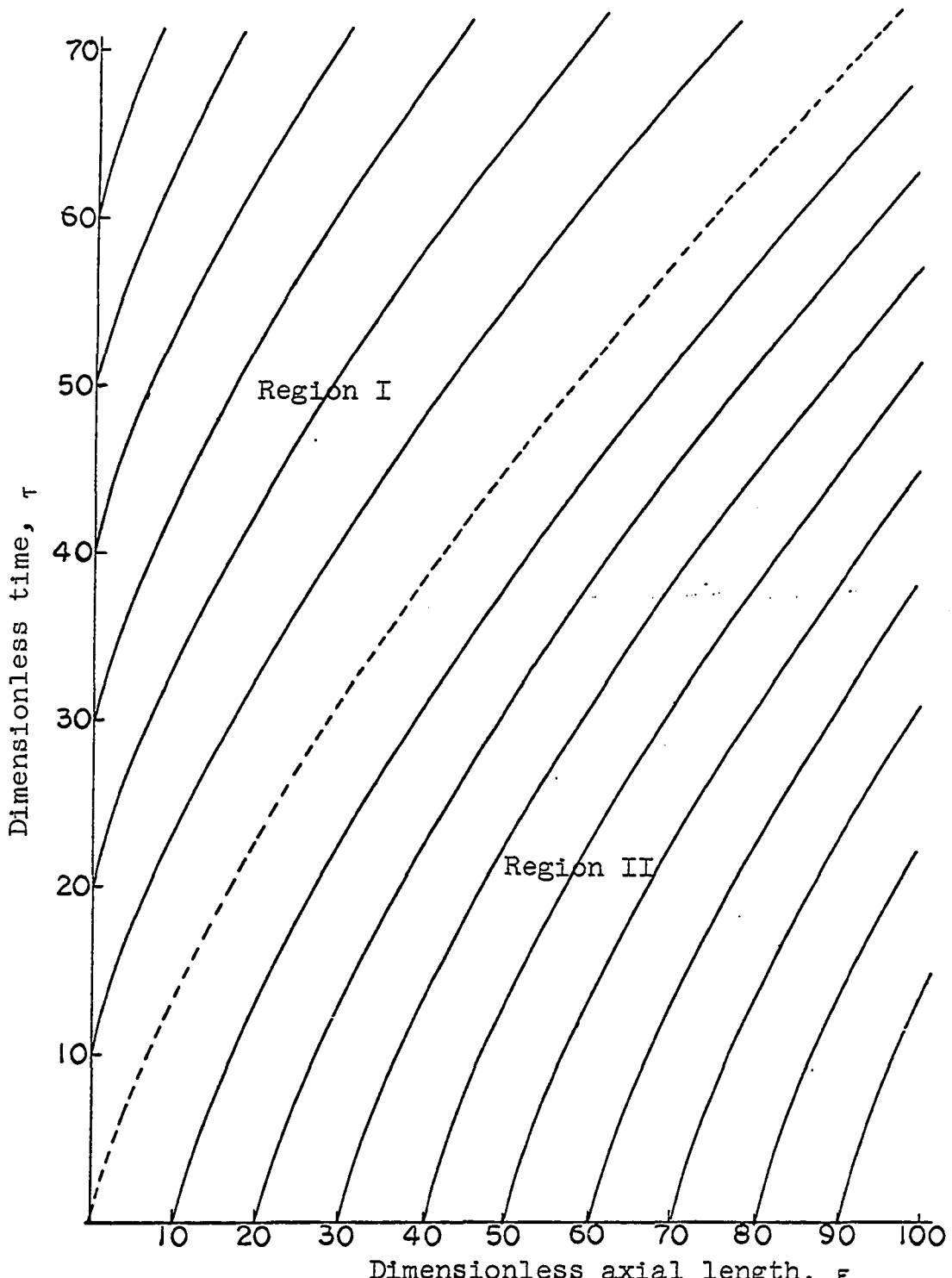

Fig. 7. Characteristics of the development of boundary layer in the entrance region of a circular tube. Constant entrance velocity, Re = 1610.

IV. EXPERIMENTAL INVESTIGATION

A. Objectives

The main purpose of the experimental investigation was to veryify the theoretical solution (computer solution) obtained for the time-dependent entrance length when a fluid, initially at rest, was suddenly set in motion under a constant head. Also, the development of suitable experimental techniques for studies involving unsteady flows of this type was considered to be important.

The experiments were further intended to determine indirectly, the unsteady entrance velocity from the pressure gradients measured in the fully developed region. The criterion for determining the fully developed region was based on the constancy of the unsteady pressure gradient with respect to axial position. The entrance velocity thus determined was used for u_o^* in the Equations 37.

B. Description of Equipment

The apparatus used in the investigation is shown in Figure 8. The flow system consisted of a constant head tank, a calming chamber, a test section, a mechanism to start the flow at the end of the tube, a collection tank and a pump. The instrumentation consisted of two strain-gage type pressure transducers, two Dana D.C. amplifiers and a two

Fig. 8. Overall view of the equipment.

A-constant head tank, B-test section,
C-pressure tap, D-pressure transducer,
E-spring-mounted plunger, F-Dana amplifier,
G-Oscilloscope equipped with Polaroid
camera.


H
A
C
D
E
G
F

channel cathode ray oscilloscope with Polaroid camera. A simple manometer and a traveling microscope were used to calibrate the pressure transducers. A graduated cylinder and a stop watch were used for determining steady-state flow rate.

The flow system schematic is illustrated in Figure 9. The constant head tank was made of an 8 in. inside diameter plexiglass tube, and was designed to produce a hydrostatic head of approximately 7-3/4 in. The calming chamber was made of a 3-1/2 in. inside diameter plexiglass tube and was positioned parallel to the test section as shown in Figure 11. The test section was a 12 ft. long brass tube with a nominal inside diameter of 0.375 in., and a wall thickness of 1/16 in. Twelve pressure taps, each of diameter 0.032 in. were drilled radially along the top edge of the tube. The inside surface of the test section was polished to eliminate burrs by rubbing with emery cloth. At each pressure tap a B & D one-way female louver valve was permanently fixed to the tube by means of a resin cement. The construction of a pressure tap is shown in Figure 13. The construction of the first tap in the entrance region was different from that of others because of its special position (see Figure 14). The distances of the pressure taps, measured from the inside surface of the face plate of the calming chamber, are given in Table 2. The distance of the first tap measured from the

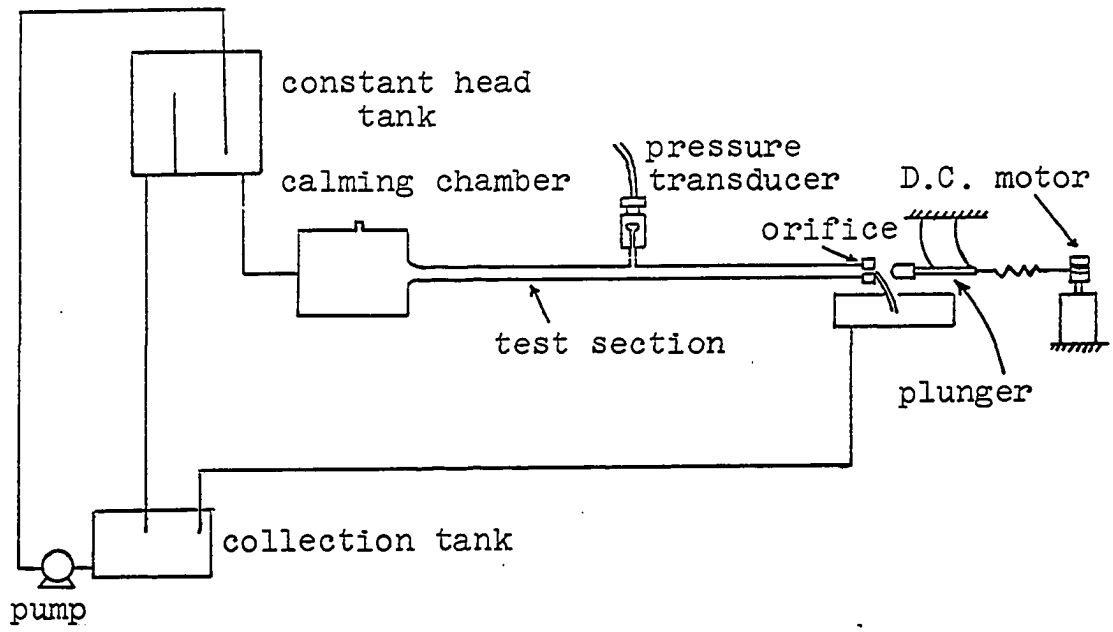

Fig. 9. Schematic of the flow system.

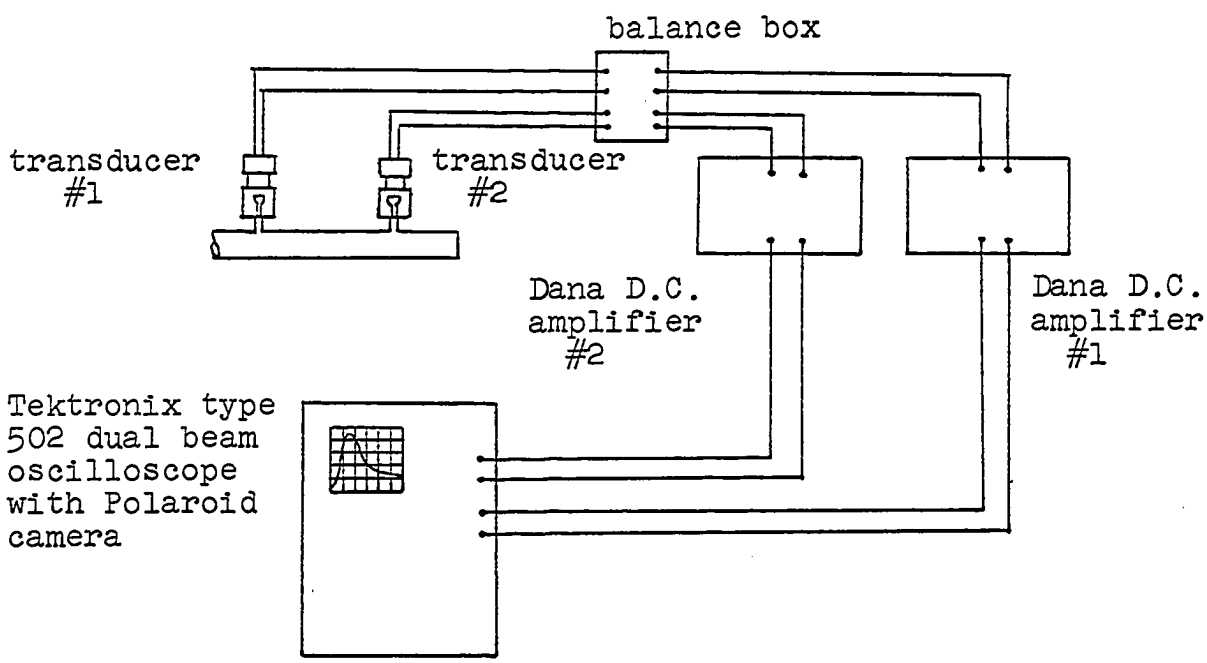

Fig. 10. Schematic of the instrumentation.

Fig. 11. The constant head tank and the calming chamber. Pressure transducer located at tap 2 can be seen on the right.

Fig. 12. Equipment for pressure measurement.

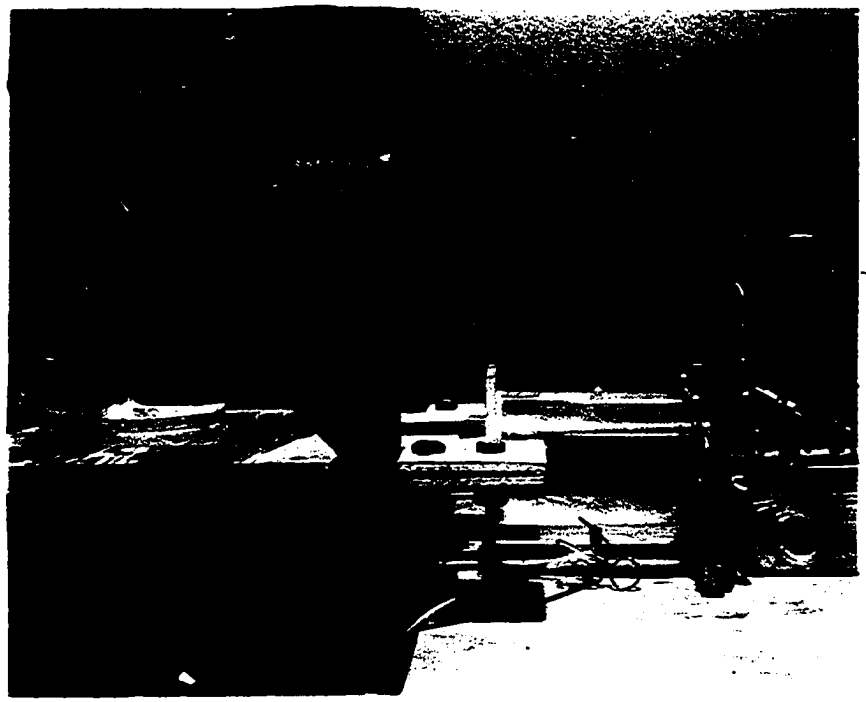

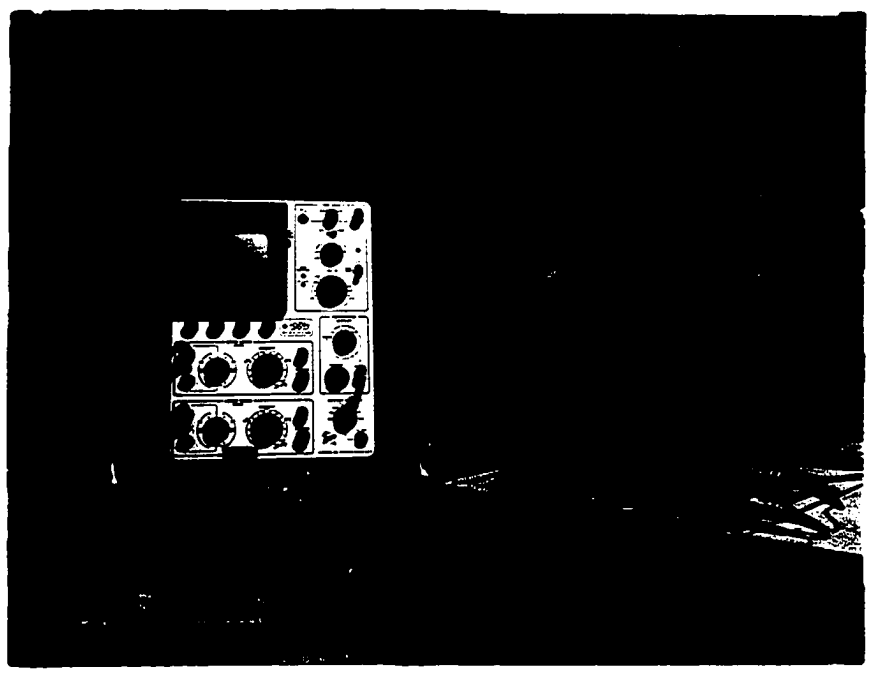

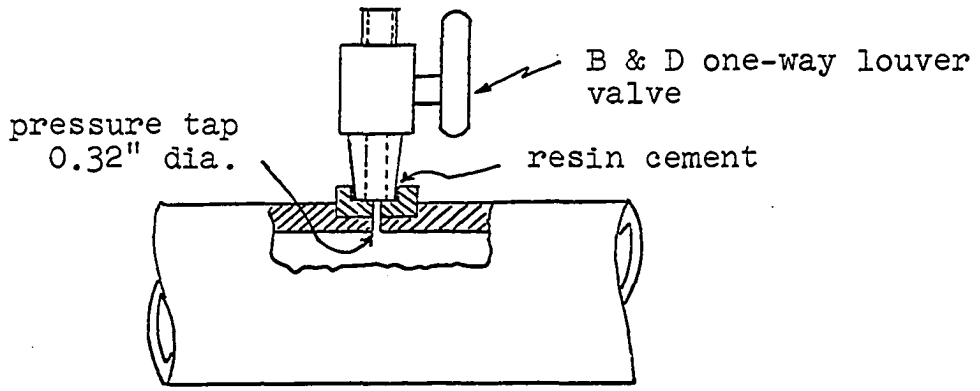

Fig. 13. Construction of the pressure tap at various axial positions.

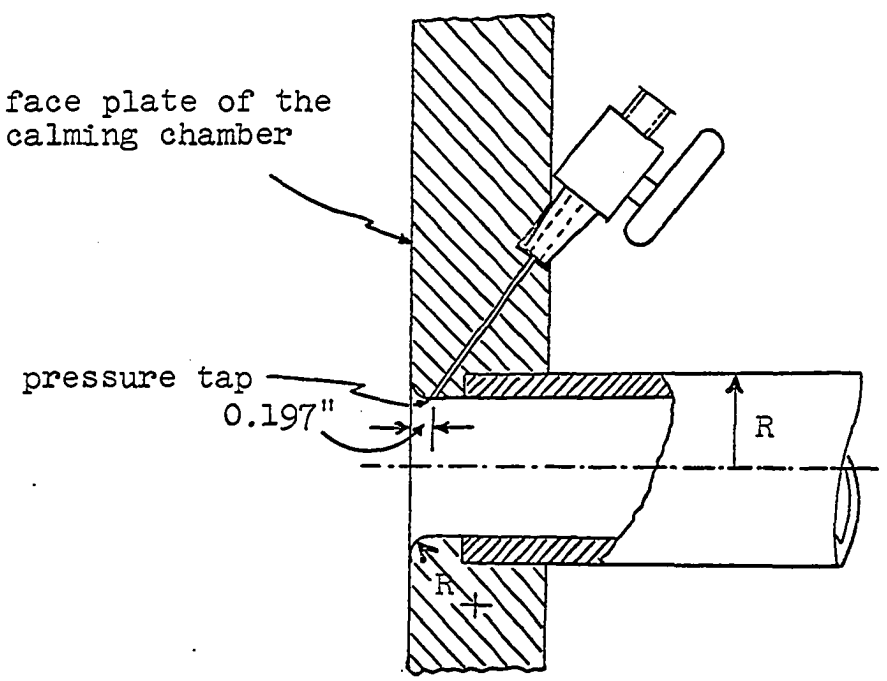

Fig. 14. Construction of the pressure tap at the entrance of the test section.

inside surface of the face plate is illustrated in Figure 14. The pressure taps were placed closer near the entrance than in the region far downstream to measure the more rapidly varying pressures near the entrance. The inlet of the test section was carefully rounded with curvature equal to the radius of the tube as shown in Figure 14.

Table 2. Distances of the pressure taps from the inside surface of the face plate of the calming chamber

Tap No.	Distance in inches	Tap No.	Distance in inches
1	0.197	7	28.375
2	1.375	8	40.375
3	2.857	9	58.375
4	4.375	10	82.375
5	10.375	11	106.375
6	16.375	12	143.375

A plexiglass orifice was inserted at the end of the test section to obtain the desired rate of flow. Two orifices were used which gave Reynolds numbers of 700 and 1610 based on the steady state average velocity. The flow was started by pulling a plunger held tight against the orifice by spring action (Figure 15). The pulling of the plunger was effected by winding a string, in conjunction with a light coiled spring, on a constant diameter sheave mounted on the shaft of a D.C. motor. The light coiled spring helped to generate

Fig. 15. Mechanism to start the flow. Plunger in the closed position.

Fig. 16. Mechanism to start the flow. Plunger in the open position.

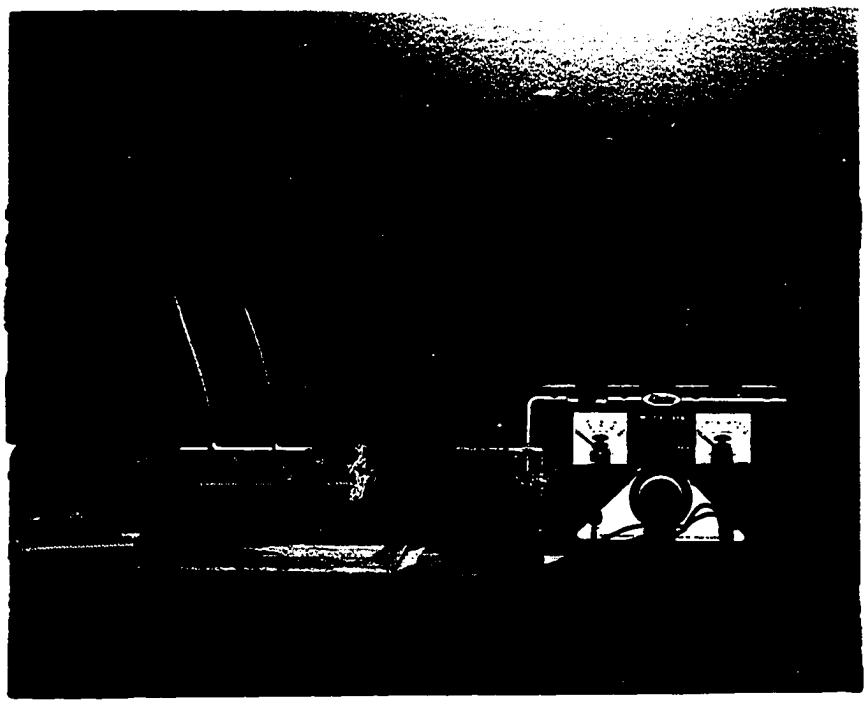

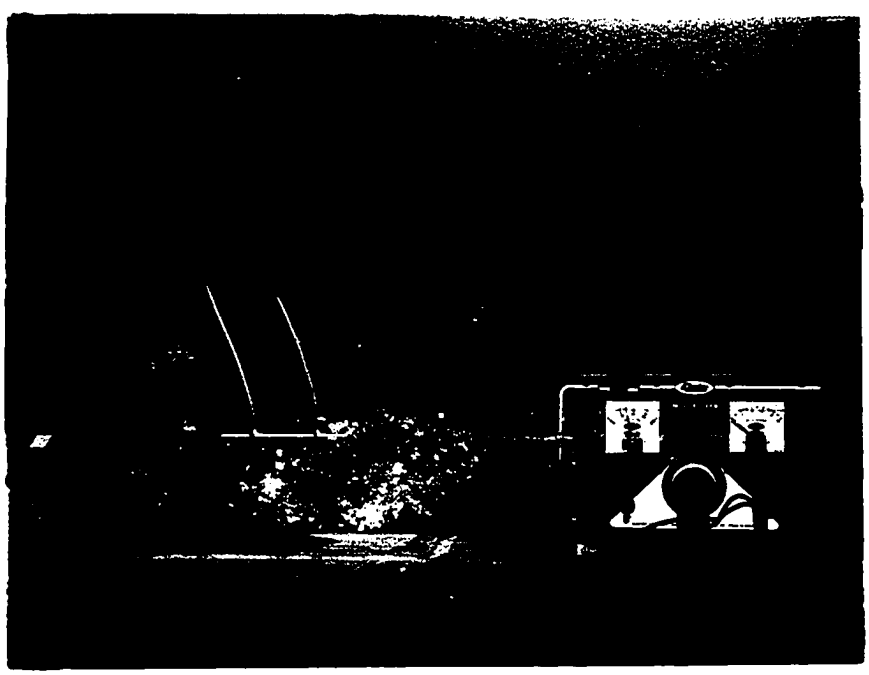

reproducibility in opening the end of the tube by absorbing the initial shock the plunger would experience when the string became taut. The position of the plunger, when the end of the tube was opened, is shown in Figure 16. The D.C. motor, which was a General Electric aircraft motor, was powered by Electro Model EFB Filtered D.C. Power Supply. The motor and the power supply unit can be seen on the right-hand side of Figures 15 and 16.

The fluid from the test section was collected in a large glass container and pumped back to the constant head tank by means of a Jabsco 1/8 hp self-priming pump.

The pressure sensing device was Model P-23Db physiological pressure transducer manufactured by Statham Laboratories, Inc. (see Figure 17). This type of pressure transducer has been widely used for dynamic pressure measurements in physiological systems. The frequency response of the transducer, as reported by the manufacturer, was approximately 200 cycles per second. The pressure transducer consisted of a thin metallic diaphragm with a fluid chamber on one side and a strain-gage bridge bonded on the other. The fluid chamber of the transducer was filled with the working fluid and connected to a pressure tap on the tube through the B & D one-way louver valve fixed thereon. The deformation of the diaphragm, due to pressure change in the fluid chamber, would cause the strain-gage bridge to produce an electrical signal proportional to the pressure change.

Fig. 17. Statham P-23Db physiological pressure transducer.

Fig. 18. Traveling microscope and the simple manometer.

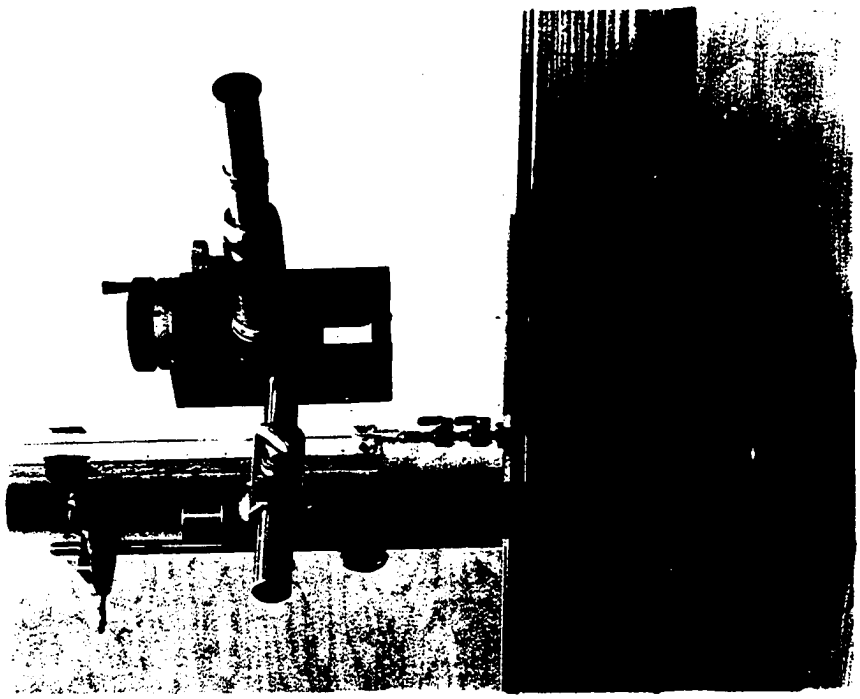

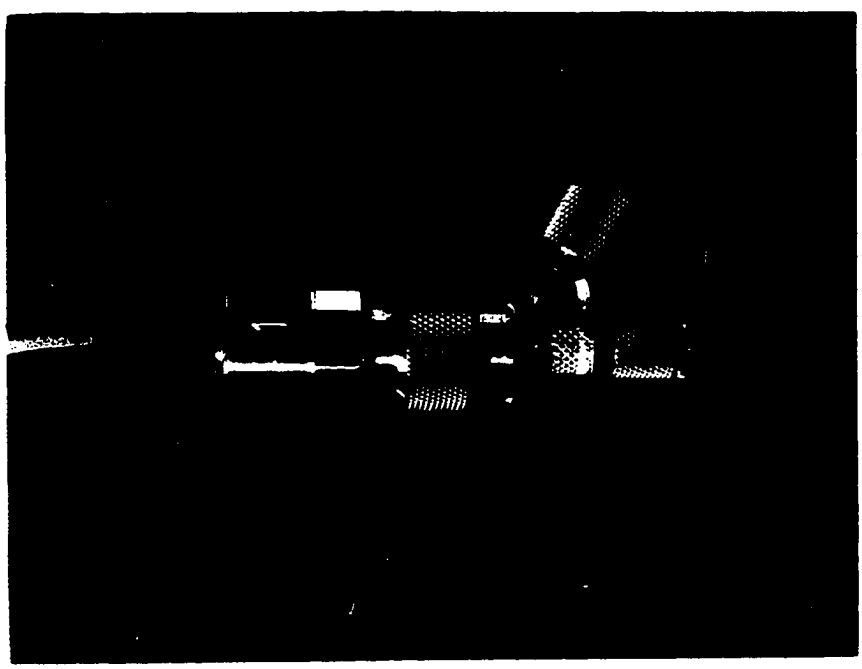

The signal from the strain-gage bridge of the transducer was amplified with a Dana D.C. amplifier and recorded on a Tektronix Type 502 Dual Beam Oscilloscope equipped with a Tektronix Type C-12 Polaroid camera (see Figure 12). The choice of the Dana D.C. amplifier was dictated by the necessity to eliminate the presence of small amplitude fluctuations, attributed to noise, which appeared on the pressure-time curve when a Brush amplifier (model BL-520) was used. With the Dana amplifier it was possible to select the range of high frequency response required to obtain a relatively sharp trace by filtering the fluctuations due to noise. The maximum possible frequency response on the Dana amplifier filter system was 1000 cycles per second. A schematic of the instrumentation is shown in Figure 10.

A simple open-end manometer and a Gaertner traveling microscope (Series No. 2119-P) were used to calibrate the pressure transducer. The manometer was constructed of a 1/8 in. inside diameter glass tube fixed to a graduated wooden ruler. To the lower end of the glass tube a B & D male louver valve was attached so the manometer could be directly connected to the female louver valve fixed to the pressure tap on the test section. The traveling microscope with a least count of 0.0001 had a capability of measuring the displacement up to 2 in. (see Figure 18). The details of the calibration procedure are presented in section C of this chapter.

C. Experimental Procedure

The procedure described in the following relates to the measurement of pressures at various axial positions along the test section in which a fluid, initially at rest, was set in motion under a constant head. The fluid used was water.

1. Preparation of the pressure transducer

It was observed that the presence of air bubbles in the fluid chamber of the pressure transducer had a strongly adverse effect on its frequency response. A device to subject the pressure transducer to a sudden change in pressure was built and the frequency response of transducer was checked. The device, shown in Figure 19, consisted of a 1 in. diameter brass tube, to which the transducer was connected at the lower end through a B & D one-way louver valve. The tube was partly filled with water and the upper end was closed with a thin plastic membrane. The fluid chamber of the pressure transducer was filled with water and the strain gage side of the transducer was connected to the amplifier and the oscilloscope equipped with a Polaroid camera. The sudden change in pressure on the transducer was generated by pressurizing the space above the liquid surface in the brass tube, by the rubber bulb of a sphygmomanometer, until the plastic membrane ruptured. From the transient damped pressure-time trace recorded by the

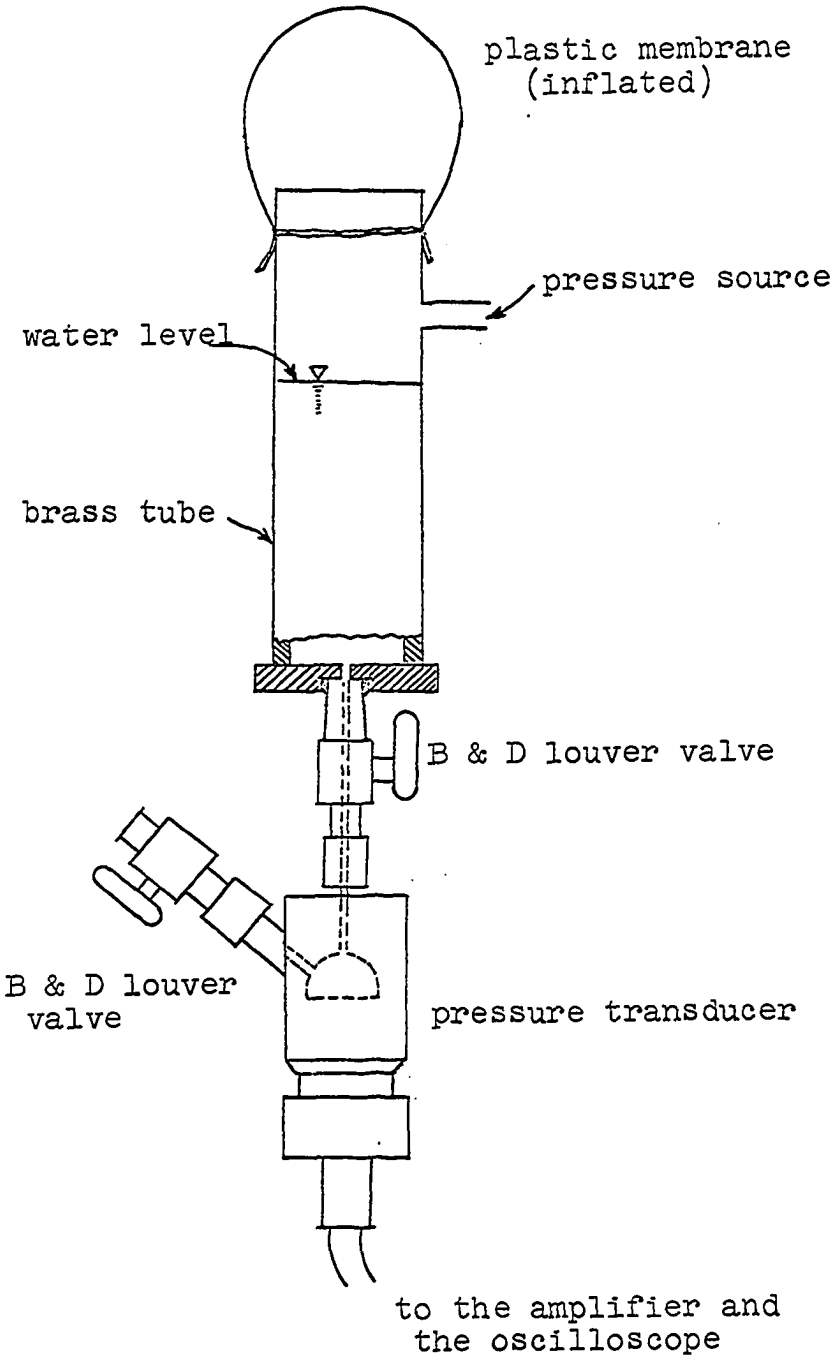

Fig. 19. "Pop" test equipment.

Polaroid camera the frequency response of the pressure transducer was estimated.

By performing a few "pop" tests described above it was learned that the removal of minute air bubbles trapped in the fluid chamber of the pressure transducer resulted in marked increase in the frequency response. To achieve as high a frequency response as possible the fluid chamber of the transducer was first flushed with distilled water to which a small quantity of a mild detergent was added. This operation, not only cleaned the surface of the metallic diaphragm, but also improved the adhesion between the fluid and the walls of the chamber. The air bubbles, if there were any, were removed by gently forcing water to and fro through the fluid chamber of the transducer by means of a hypodermic syringe. This step was taken regardless of whether air bubbles were visible or not. The frequencies recorded from the "pop" tests were consistently in the range of 150-180 cycles per second.

In actual use in the flow tests, the pressure transducer was fixed to the pressure tap, on the test section, where the pressure variation was to be recorded. The air bubbles, possibly trapped while the transducer was being fixed to the pressure tap, were removed by using the hypodermic syringe once again. The pressure transducer was then ready to use in the recording of the pressure-time curve.

2. Recording of the pressure-time curve

Before the actual measurement of pressures, the water in the flow system was allowed to circulate for approximately an hour to reach a steady state temperature. Two pressure transducers were simultaneously used for the pressure measurements. One of the transducers was attached to the first pressure tap at the inlet, and the other to the last tap at the end of the tube. A time lapse of about 5 minutes was allowed for the transducers to attain the temperature of the fluid. This procedure was followed whenever the transducer was shifted to a different axial location, since the transducers were found to be temperature-sensitive.

Appropriate sensitivity settings were selected on the amplifiers and the oscilloscope. The selection was dictated by the amount of measurable deflection and the degree of clarity of the recorded curve. The shutter of the Polaroid camera was kept open, and the oscilloscope was placed on single sweep. When the end of the tube was opened by pulling the plunger with the help of the D.C. motor the oscilloscope was triggered, and the pressure-time curve was photographed by the camera. The transducer at the first tap was then shifted to the second, to the third, and so on. The transducer attached to the last tap at the end of the tube was always retained at that position. If only one transducer was used in the experiment it would have been difficult to

decide whether the flow was started exactly the same way each time the plunger was pulled. To check the reproducibility of the starting of flow the signal from the transducer retained at the last tap was examined intermittently during the experiment. Also, the pressure-time trace at a randomly chosen tap was recorded for repeated startings of the flow and all traces superimposed on the same photograph. Some examples of such photographs, shown in Figure 20, indicate satisfactory reproducibility. In Figure 20 the maximum deviation from the average curve was estimated to be $\pm$ 4 per cent.

The pressure-time curve at each pressure tap was recorded at two different sweep rates. A slower sweep rate was chosen to record the complete pressure-time curve up to fully established flow. A faster sweep rate was selected to extend the pressure-time curve, for better readability, in the initial period of the flow development. The two sweep rates were different for the two rates of flow considered. For the Reynolds number 1610, sweep rates of 50 milliseconds per centimeter and 0.2 second per centimeter were used. For the Reynolds number 700, sweep rates of 20 milliseconds per centimeter and 0.1 second per centimeter were used. At each location the pressure-time curves using both the sweep rates were recorded on the same photograph. Some examples of the pressure-time curves for the Reynolds number 1610

Fig. 20. Demonstration of reproducibility.

Frames A and B are exposed at tap 8. Each contains four exposures superposed on one another. Frames C and D are exposed at tap 12. Each contains three superpositions.

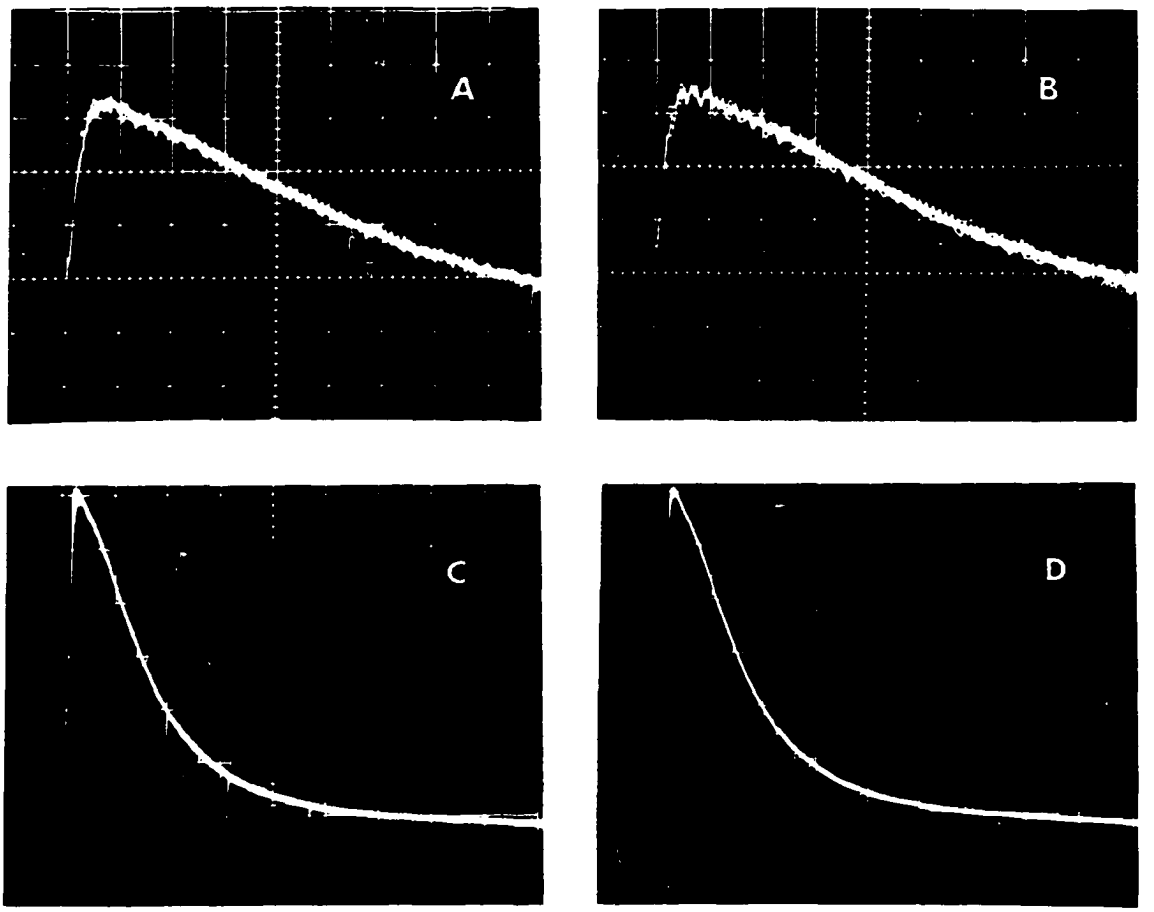
A
B
C
D

are shown in Figure 21. The lower curves were obtained with the sweep rate of 0.2 second per centimeter and the upper curves were obtained with the sweep rate of 50 milliseconds per centimeter.

The pressure-time curve, as can be seen in one of the frames in Figure 21, is characterized by a rapid drop in pressure from the available hydrostatic pressure and then a gradual increase in pressure to a steady value, independent of time, at which stage the flow is considered to be fully developed. The deflection of the pressure-time curve from the line of reference (corresponding to a state of rest) in the steady state region gives steady state pressure drop when multiplied by the appropriate calibration factor. Figure 21 presents pressure-time curves at tap numbers 1, 3, 4, 6, 8 and 9 with appropriate adjustments of the sensitivity on the amplifier and the oscilloscope. The reference line corresponding to the state at which the fluid is at rest is not shown in Figure 21. In the frames 2-6 the reference line is the lower most horizontal grid line. In the frame 1 the first and third horizontal grid lines from below are the reference lines for the slower and faster traces respectively. It can be observed in these curves that the peak pressure drop occurred nearly at the same instant (40 milliseconds from the start of the flow) at all the axial locations, and the magnitude of pressure drop increased as we moved downstream. Also, the time required to reach a steady value of

Fig. 21. Some examples of pressure-time curves. Re 1610.

Frame 1 Pressure-time curve at tap 1
Frame 2 Pressure-time curve at tap 3
Frame 3 Pressure-time curve at tap 4
Frame 4 Pressure-time curve at tap 6
Frame 5 Pressure-time curve at tap 8
Frane 6 Pressure-time curve at tap 9

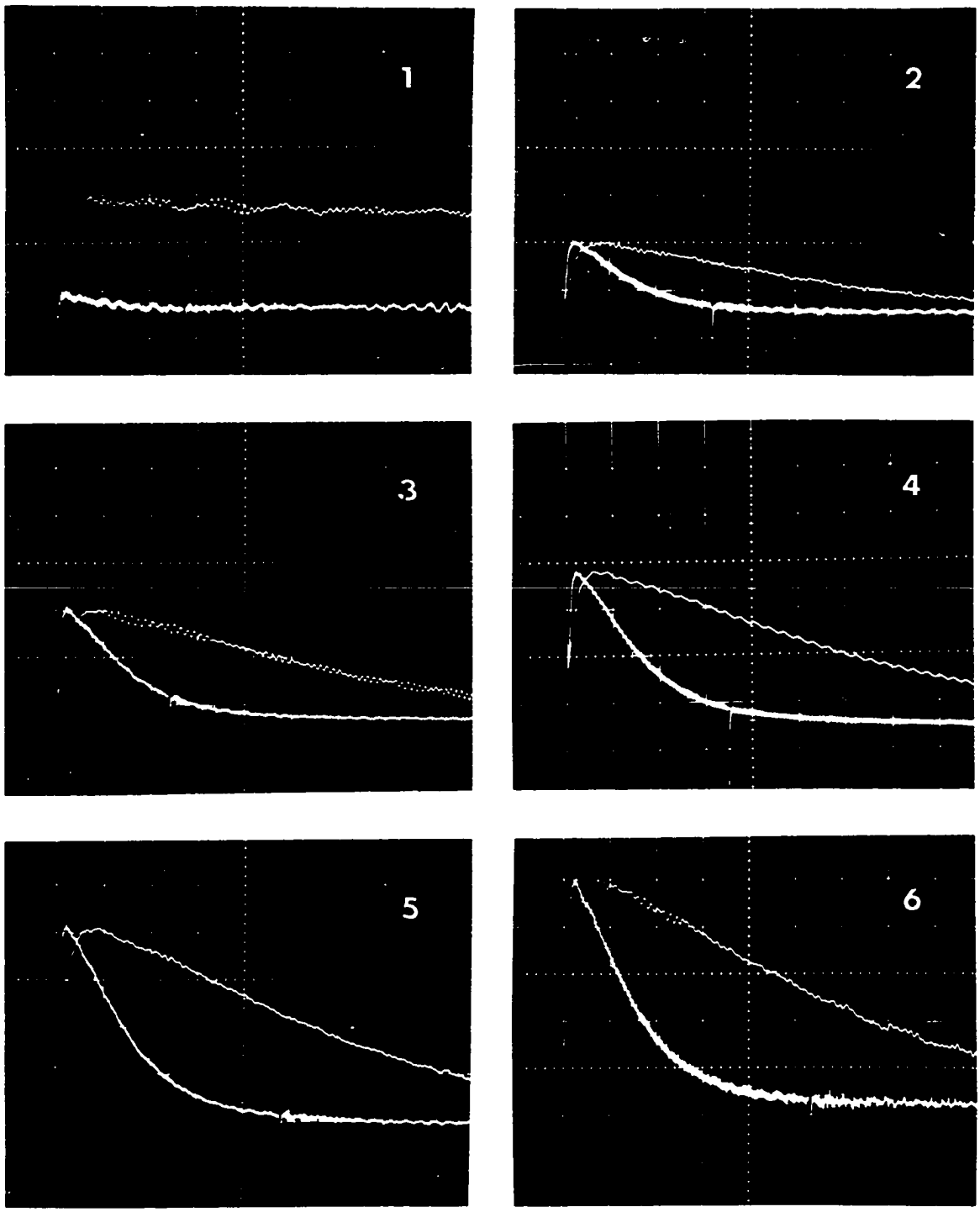
1
2
3
4
5
6

pressure increased as we moved downstream from the inlet to the subsequent axial positions.

From the pressure-time curves at various axial locations the pressures at various instants along the length of the test section were determined and plotted as pressure versus length curves. These curves are presented in section D of this chapter.

3. Calibration of the pressure transducer

The pressure transducer was calibrated by determining the deflection of the pressure-time curve in the steady state region and relating this deflection to the actual pressure drop for steady flow through the test section at the corresponding locations. The actual steady-flow pressure drop was measured in inches of water, by using the previously described simple manometer and a traveling microscope for both flow rates considered. The steady-flow pressure drops encountered in the experiment at various axial locations were in the range 0 to 0.53 inches of water. To determine the actual pressure corresponding to the line of reference in the pressure-time curves the hydrostatic head was measured. Slight variation in the hydrostatic head at each location was considered likely due to possible misalignment in laying the test section and diversity in the height of the louver valves. In view of the small magnitudes of pressure drops encountered in the experiment this variation could not be

overlooked. The local variation of the hydrostatic head was taken into account in determining the local pressure drop and in plotting the pressure versus length curves at various instants. The local hydrostatic pressure head and the pressure drop for the two flow rates are presented in Table 3. The hydrostatic pressure head at taps 1, 9, 10, 11, and 12 were not measured due to difficulties encountered in setting up the manometer and the traveling microscope.

The deflections in the steady state region of the pressure-time curves were then related with the actual pressure drops and expressed in the form of calibration curves presented in Figure 22. These curves were obtained for various sensitivity positions, on the amplifier and the oscilloscope, associated with the pressure-time curves. Although the pressure transducer was calibrated against known steady state values of pressure drop, the resulting calibration factors were used in determining the pressure drop in unsteady flow because the frequency response of the transducer was considered to be sufficiently high.

There were some inherent advantages in regard to the calibration procedure just described. Firstly, it did not require a delicate device to produce known values of pressure in the range 0-0.53 inches of water. Secondly, since the pressure drops were measured at the time of recording the pressure-time curves, the time lapse between the

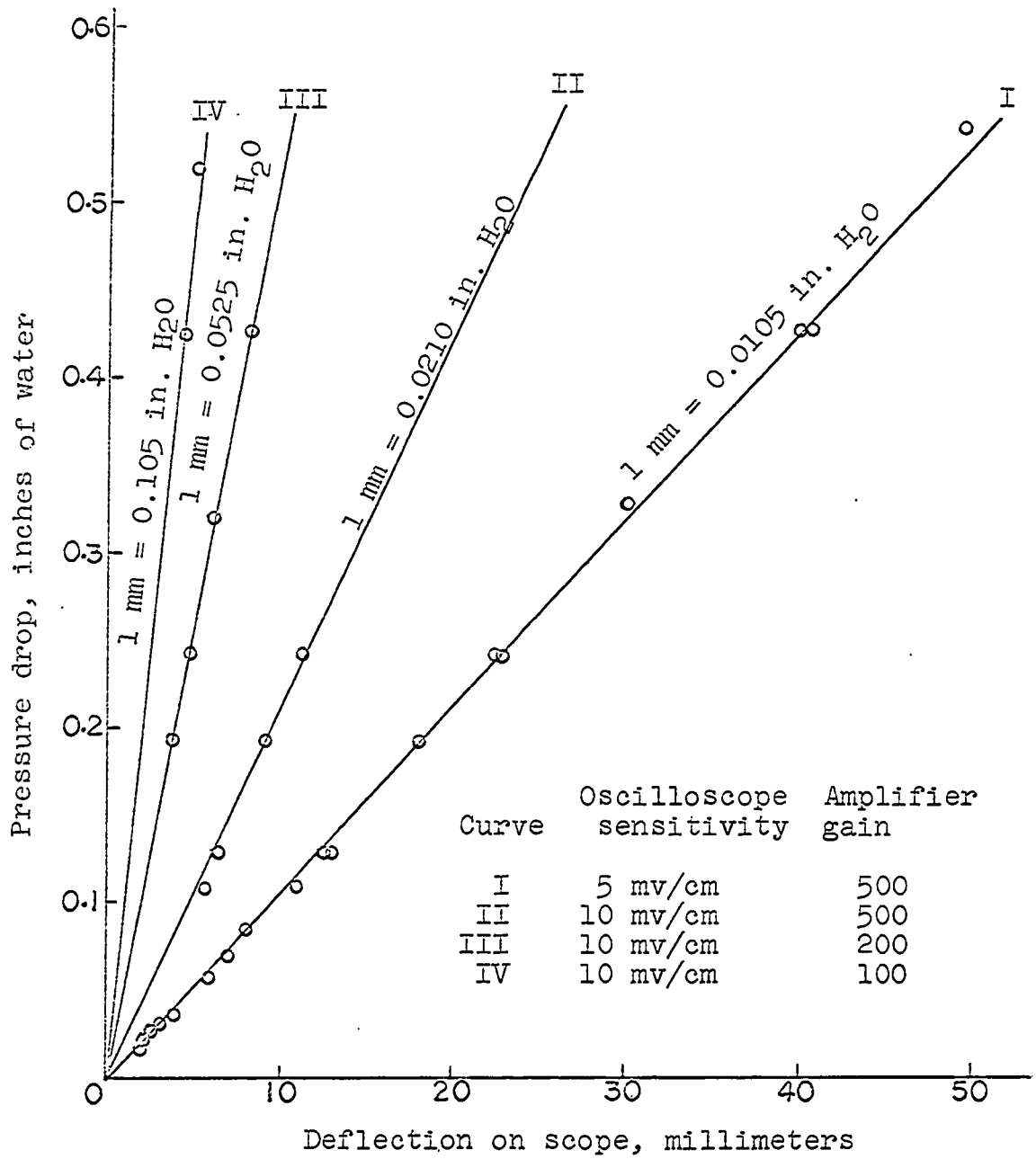

Fig. 22. Calibration curves.

Table 3. Local hydrostatic pressure head and pressure drop in steady flow

Tap No.	Hydrostatic pressure heads in inches of water	Steady state pressure drop in inches of water	
		Re = 1610	Re = 700
2	7.816	0.0580	0.0210
3	7.820	0.0700	0.0238
4	7.817	0.0850	0.0309
5	7.807	0.1091	0.0408
6	7.804	0.1290	0.0559
7	7.791	0.1917	0.0900
8	7.772	0.2429	0.1190
9	-	0.3211	0.1642
10	-	0.4266	0.2296
11	-	0.5226	0.2900

calibration and the actual performance of the experiment was at a minimum thus avoiding possible calibration drift.

4. Measurement of the rate of steady flow

A 50 ml graduated cylinder and a stop watch were used to measure the rate of flow after it was fully developed. Two flow rates were considered in the experiment. For each flow rate an average of ten measurements was obtained. The temperature of the water was 28.5° C throughout the duration of the experiment. The average inside diameter of the tube was 0.374 inch. One flow rate was 0.609 cubic inches per second, and the resulting Reynolds number was 1610. The other

flow rate was 0.265 cubic inches per second and the Reynolds number 700.

D. Experimental Results

From the pressure-time curve at each tap the pressure drops at various instants after the flow was commenced were determined. From these data, curves relating pressure drop and axial length, at various instants, were obtained. For the two flow rates considered these curves in dimensionless form are presented in Figures 23 and 24. The data obtained from the pressure-time curves, converted into dimensionless pressure drops, are given in Appendix D.

As shown in Figures 23 and 24, the pressure gradient, at any instant, first varied up to a certain length of the tube and then remained constant. This length beyond which the pressure gradient remained constant is defined as the entrance length for this investigation. From Figures 23 and 24 it is hard to determine the entrance length because of the scale to which these figures are drawn. The variation of the instantaneous pressure gradient in the proximity of the inlet can be clearly seen when the figures are drawn to an enlarged scale. This is discussed in detail in Chapter VI. Also, the pressure gradient line, which was initially horizontal sweeps across the pressure-length plane until it reached an extreme position at the instant corresponding to

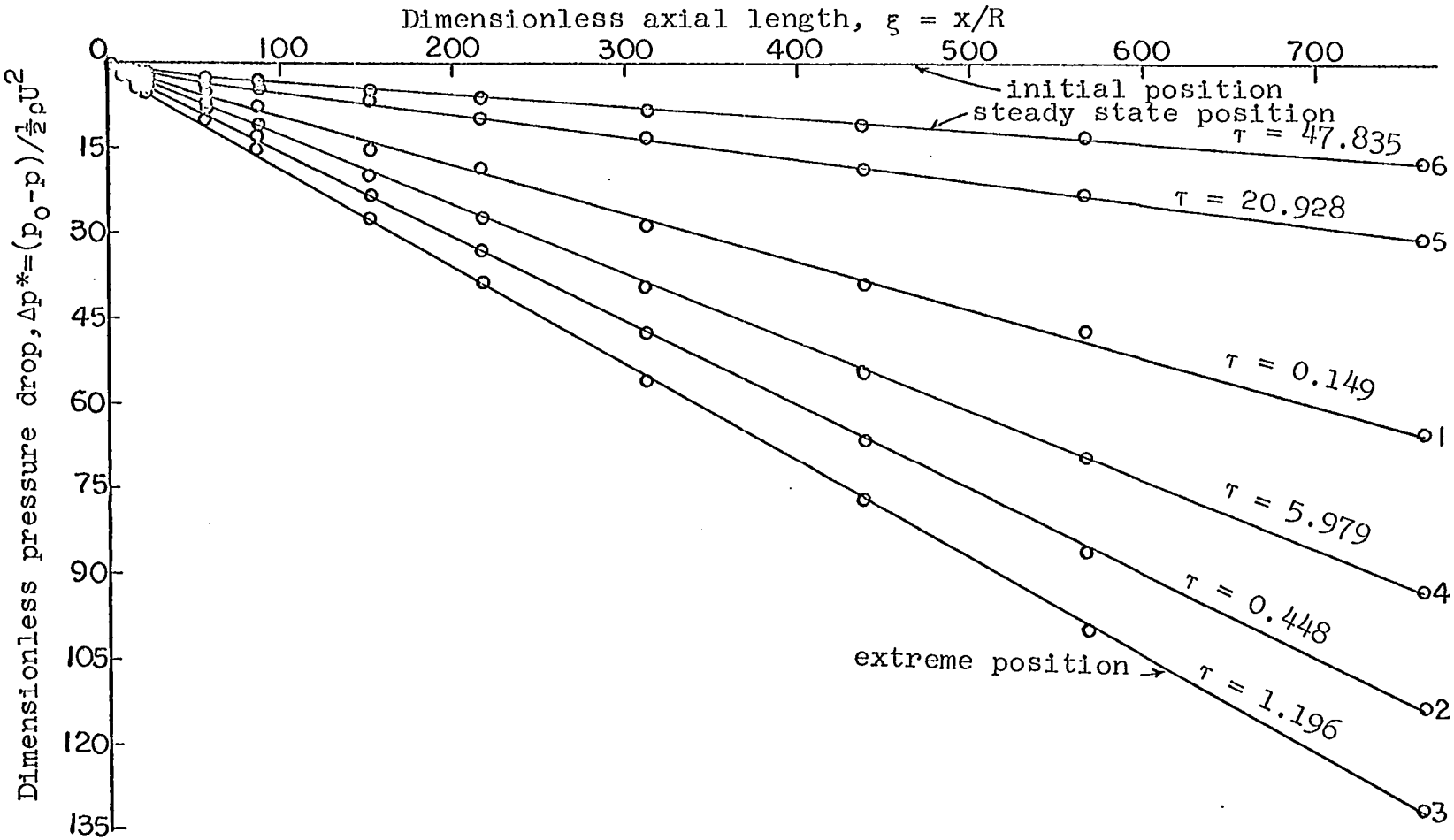

Fig. 23. Axial variation of pressure at various instants, Re = 1610.

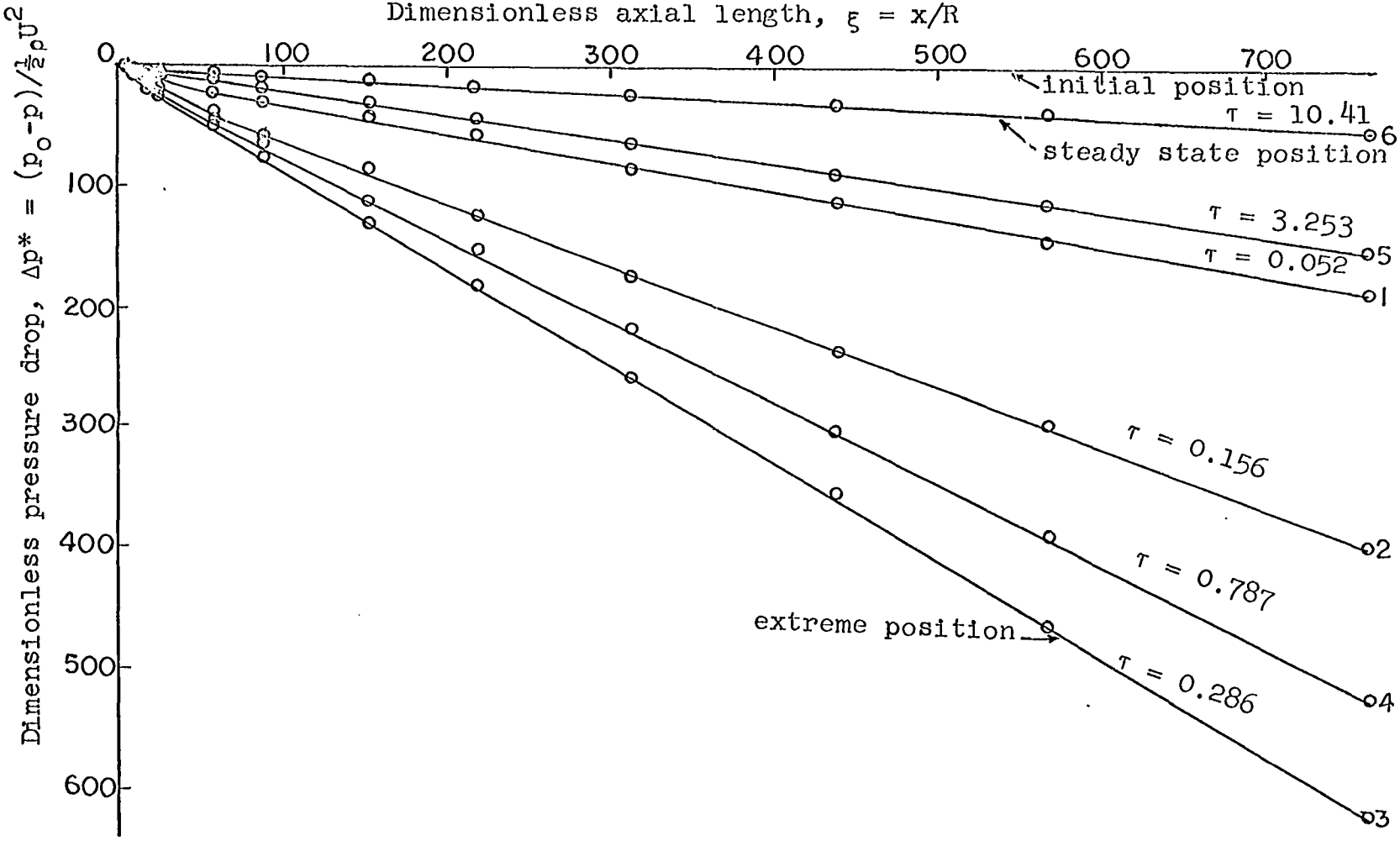

Fig. 24. Axial variation of pressure at various instants, Re = 700.

the peak pressure drop and then approaches the position of the steady-state pressure gradient.

The instantaneous value of the mean velocity in the tube is difficult to measure and no completely satisfactory flow meters are available for this measurement. Thus a method based on the relationship between the pressure gradient and flow was used.

To determine the unsteady entrance velocity the pressure gradient in the fully developed region was expressed as a function of time. Figures 25 and 26 show the pressure gradient-time relationship for the two rates of flow considered. The variable along the horizontal axis is expressed as dimensionless time τ, and the variable along the vertical axis as dimensionless pressure gradient $dp^*/d\xi$, where $p^* = p/\frac{1}{2}\rho U^2$. The method of determining the unsteady entrance velocity is described in Chapter V.

For steady flow with the Reynolds number 1610, the measured volume rate of flow and the volume rate of flow determined by using the Hagen-Poiseuille equation were compared. By the Hagen-Poiseuille equation the flow rate is given by the equation

$$Q = \frac{\Delta P}{L} \frac{\pi R^4}{8\mu} \tag{40}$$

where $\frac{\Delta P}{L}$ = Pressure gradient in the fully developed region

R = radius of the tube

μ = absolute viscosity of the fluid

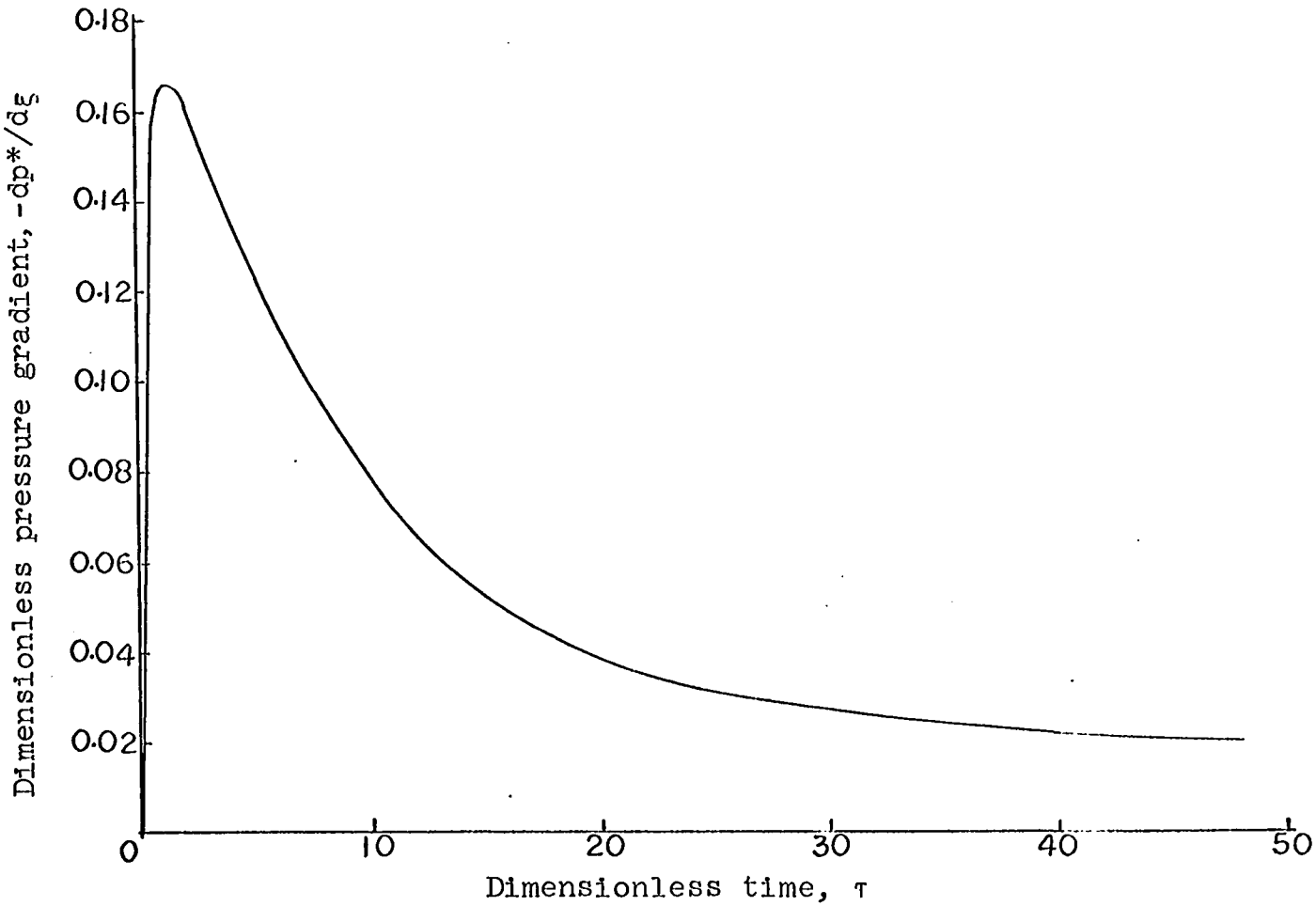

Fig. 25. Variation of pressure gradient with time, Re = 1610.

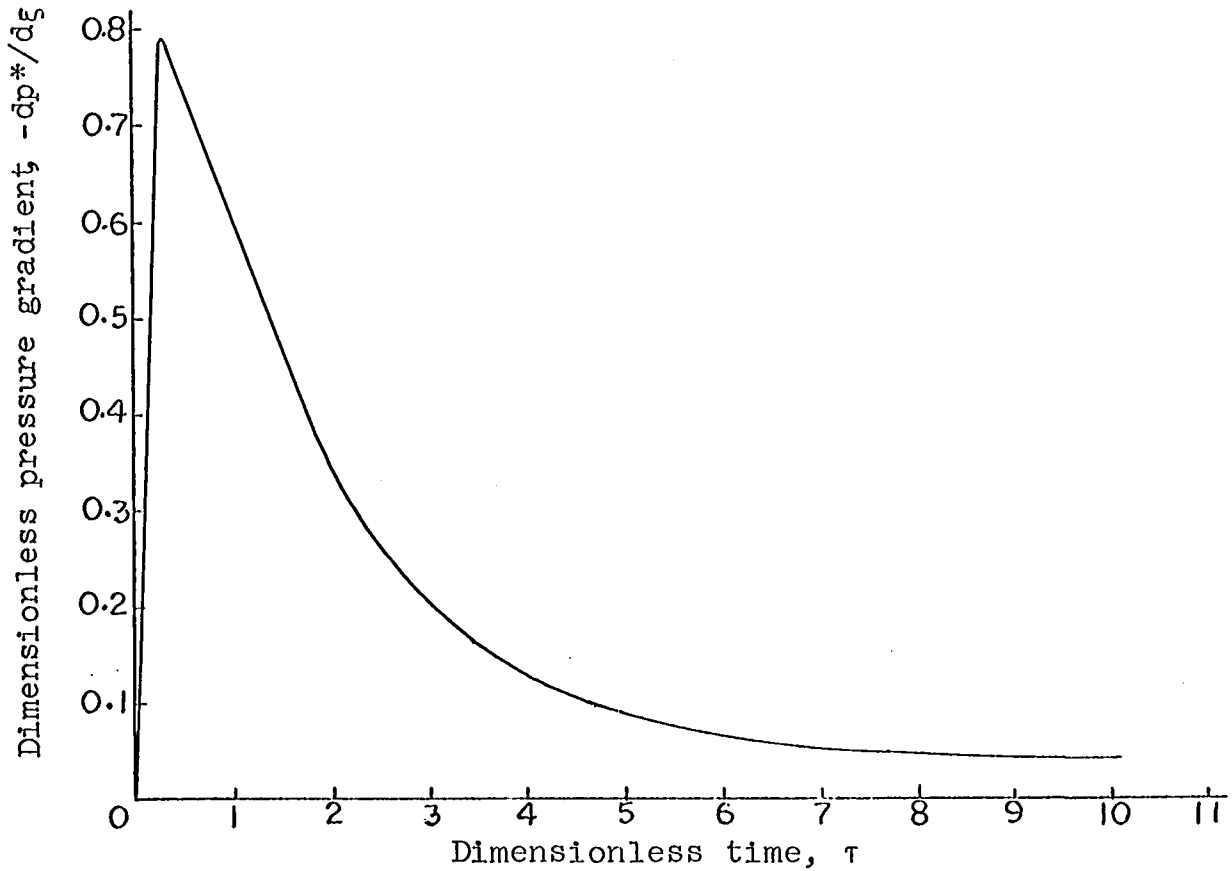

Fig. 26. Variation of pressure gradient with time, Re = 700.

From the pressure-time curves recorded at the taps 10 and 12 the pressure drop was determined to be 0.26 inches of water or 0.26 x 0.03613 pounds per square inch. The distance between the taps (see Table 2) was 61 inches. The viscosity of water at 28.5° C is 17.3×10^{-6} pound-second per square foot or $17.3 \times 10^{-6}/144$ pound-second per square inch. The radius of the tube was 0.374/2 inch or 0.187 inch.

Then

$$Q = \frac{0.26 \times 0.03613}{61} \frac{\pi (0.187)^4}{8(17.3 \times 10^{-6})/144}$$

$$= 0.615 \text{ cubic inches per second.}$$

The volume flow rate of 0.615 cubic inches per second, determined from the Hagen-Poiseuille equation, agreed well with the measured flow rate of 0.609 cubic inches per second. This agreement gave an added degree of confidence in the flow system.

V. DETERMINATION OF THE UNSTEADY ENTRANCE VELOCITY

To solve the set of Equations 37 it is necessary to specify the dimensionless velocity, u_o^*, as a function of time and space. One of the assumptions associated with the boundary layer model for unsteady flow in the entrance region is that the entrance velocity is uniform over the cross-section of the inlet and therefore u_o^* is a function of time alone. The subject of discussion in this chapter is the determination of u_o^* for the specific tests run.

By the principle of continuity the volume rate of flow crossing the inlet is equal to the discharge obtained by integrating the velocity profile, at any downstream position, over the entire cross-section of the tube. An expression for the unsteady velocity can be derived by integration of the Navier-Stokes equations. If we choose to use the velocity profile in the fully developed region, the Navier-Stokes equations may be integrated, at least in principle, since the nonlinear (convective acceleration) terms become identically zero in the fully developed region. It can be observed in Figures 23 and 24 that the pressure gradient in the fully developed region is a function of time alone. The experimental data of the instantaneous pressure gradient (Figures 25 and 26) may be approximated by a function of time and this function can subsequently be used in solving the

Navier-Stokes equations. Thus the determination of the entrance velocity from the solution of the Navier-Stokes equations is tantamount to an indirect measurement of the entrance velocity from the experimentally determined instantaneous pressure gradient. In the present investigation this indirect method of determining the entrance velocity was utilized since it was not possible to measure directly the unsteady entrance velocity (or, unsteady discharge) with any available experimental means.

A. Determination of the Pressure Gradient Function

The shape of the pressure gradient versus time curve, as can be seen in Figures 25 and 26, is characterised by a rapid rise in the pressure gradient and then a gradual fall to a constant value independent of time. The general shape of this experimental curve may be approximated by the function $g(\tau) = A(1-e^{-\ell\tau}) + B\tau^{m}e^{-k\tau}$, where A, B, k, ℓ, and m are appropriate constants. The function $g(\tau)$ is 0 at $\tau = 0$ and approaches the value A as $\tau \to \infty$. The value, A, is the constant pressure gradient pertaining to the steady state, and it is fixed from the experimental data obtained for large time. In the function $g(\tau)$ the constants B, k, ℓ, and m are determined by trial and error.

For the flow corresponding to the Reynolds number 1610 the instantaneous pressure gradient in the fully developed

region was approximated by the function

$$g(\tau) = -\frac{\partial p^*}{\partial \xi} = 0.02(1-e^{-0.25\tau}) + 0.19\tau^{0.18}e^{-0.16\tau} \quad (41)$$

For the case of the Reynolds number 700 the function was determined to be

$$g(\tau) = -\frac{\partial p^*}{\partial \xi} = 0.047(1-e^{-0.62\tau}) + 2.0\tau^{0.52}e^{-1.17\tau} \quad (42)$$

The curves of the function $g(\tau)$ for both the Reynolds numbers are superposed on the corresponding experimental curves in Figures 27 and 28 to demonstrate the goodness of fit.

B. Solution of the Navier-Stokes Equations

For axial flow in the fully developed region, the Navier-Stokes equations in the nondimensional form reduce to

$$\frac{\partial u^*}{\partial \tau} = -\frac{1}{2}\frac{\partial p^*}{\partial \xi} + \frac{\nu}{UR}\left(\frac{\partial^2 u^*}{\partial r^{*2}} + \frac{1}{r^*}\frac{\partial u}{\partial r^*}\right) \quad (43)$$

where the dimensionless parameters

$u^* = u/U$

$r^* = r/R$

$p^* = p/\frac{1}{2}\rho U^2$

$\tau = tU/R$, and

$\xi = x/R$

From the definition of the Reynolds number $\frac{\nu}{UR} = \frac{2}{Re}$

Let

$$-\frac{1}{2}\frac{\partial p^*}{\partial \xi} = f(\tau)$$

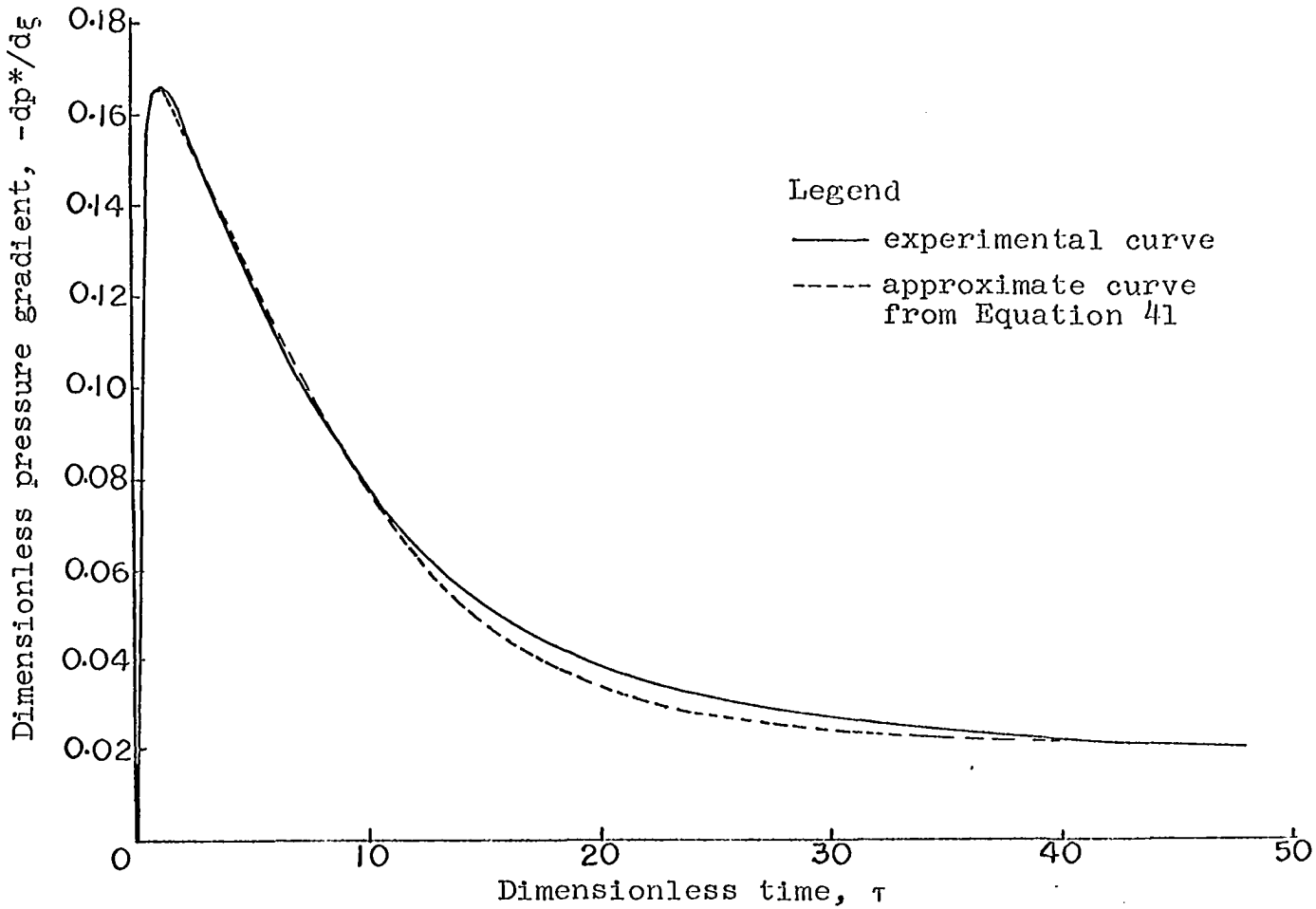

Fig. 27. Comparison of experimental and approximate pressure gradient curves, Re = 1610.

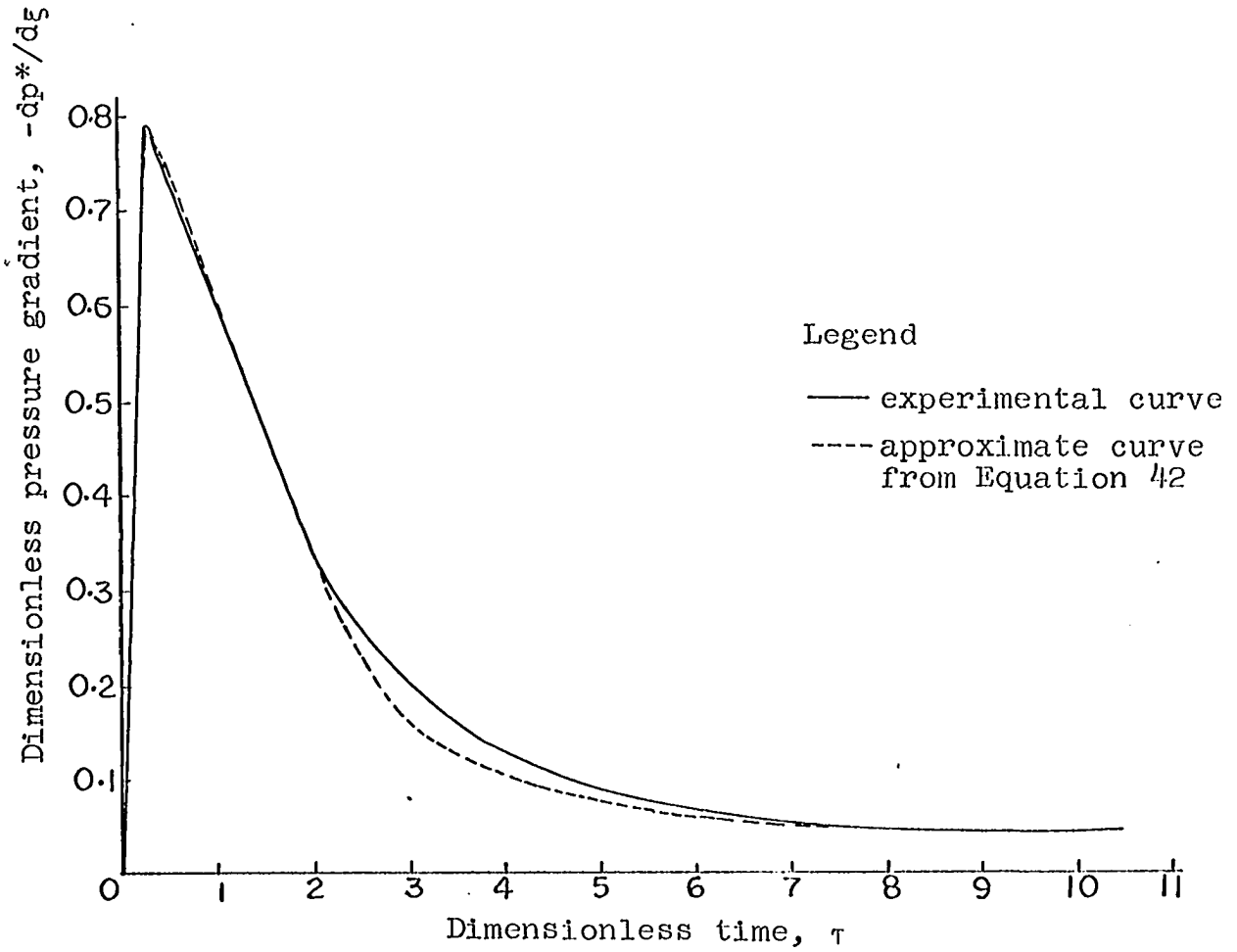

Fig. 28. Comparison of experimental and approximate pressure gradient curves, Re = 700.

so that

$$f(\tau) = \tfrac{1}{2}g(\tau)$$
$$= \tfrac{1}{2}\{A(1-e^{-\ell\tau})+B\tau^m e^{-k\tau}\}$$
$$= a(1-e^{-\ell\tau})+b\tau^m e^{-k\tau} \qquad (44)$$

where a = A/2 and b = B/2.

Then Equation 43 can be written as

$$\left(\frac{\partial^2 u^*}{\partial r^{*2}} + \frac{1}{r^*}\frac{\partial u^*}{\partial r^*}\right) - \frac{Re}{2}\frac{\partial u^*}{\partial \tau} = -\frac{Re}{2} f(\tau) \qquad (45)$$

The pertinent boundary and initial conditions are

$$u^* = 0 \text{ at } r^* = 1 \text{ for all } \tau \geq 0$$
$$u^* = 0 \text{ at } \tau = 0 \text{ for all } 0 \leq r^* \leq 1 \qquad (46)$$

Define the Laplace transforms with respect to a variable s as

$$\mathcal{L}(u^*) = \bar{u} = \int_0^\infty e^{-s\tau} u^* d\tau$$

$$\mathcal{L}\{f(\tau)\} = \bar{f} = \int_0^\infty e^{-s\tau} f(\tau) d\tau$$

The Laplace transform of Equation 45 is

$$\mathcal{L}\left\{\frac{\partial^2 u^*}{\partial r^{*2}} + \frac{1}{r^*}\frac{\partial u^*}{\partial r^*}\right\} - \mathcal{L}\left\{\frac{Re}{2}\frac{\partial u^*}{\partial \tau}\right\} = \mathcal{L}\left\{-\frac{Re}{2} f(\tau)\right\}$$

or,
$$\bar{u}_{r^*r^*} + \frac{1}{r^*}\bar{u}_{r^*} - s\frac{Re}{2}\bar{u} = -\frac{Re}{2}\bar{f} \qquad (47)$$

where suffix denotes differentiation. The corresponding boundary condition is

$$\bar{u} = 0 \text{ at } r^* = 1 \qquad (48)$$

The general solution of Equation 47 is

$$\bar{u} = A_1 I_o\left(\sqrt{s\frac{Re}{2}}\, r^*\right) + A_2 K_o\left(\sqrt{s\frac{Re}{2}}\, r^*\right) + \frac{\bar{f}}{s}$$

where A_1 and A_2 are functions of s, and I_o and K_o are modified Bessel functions of the first and second kind of zero order, respectively. Since $\bar{u}$ must be finite at $r^* = 0$, the function $A_2 = 0$. Then the solution of Equation 47 is

$$\bar{u} = A_1 I_o\left(\sqrt{s\frac{Re}{2}}\, r^*\right) + \frac{\bar{f}}{s} \tag{49}$$

With the boundary condition $\bar{u} = 0$ at $r^* = 1$ the solution becomes

$$\bar{u} = \frac{\bar{f}}{s} - \frac{\bar{f}}{s}\frac{I_o\left(\sqrt{s\frac{Re}{2}}\, r^*\right)}{I_o\left(\sqrt{s\frac{Re}{2}}\right)} \tag{50}$$

$$= \bar{u}_1 - \bar{u}_2$$

where $\bar{u}_1 = \frac{\bar{f}}{s}$, and

$$\bar{u}_2 = \frac{\bar{f}}{s}\frac{I_o\left(\sqrt{s\frac{Re}{2}}\, r^*\right)}{I_o\left(\sqrt{s\frac{Re}{2}}\right)}$$

According to Carslaw and Jaeger (4) the inverse Laplace transform of $\bar{u}$ is

$$u^* = \mathcal{L}^{-1}(\bar{u}) = \mathcal{L}^{-1}(\bar{u}_1) - \mathcal{L}^{-1}(\bar{u}_2)$$

$$= u_1^* - u_2^* \tag{51}$$

Then $$u_1^* = \mathcal{L}^{-1}\left(\frac{f}{s}\right) = \int_o^T f(T)\, dT \tag{52}$$

where T is a dummy variable, and

$$u_2^* = \mathcal{L}^{-1}\left\{\frac{\bar{f}}{s}\frac{I_o\left(\sqrt{s\frac{Re}{2}}\, r^*\right)}{I_o\left(\sqrt{s\frac{Re}{2}}\right)}\right\}$$

We express $\bar{u}_2$ as the product $\bar{f}\bar{G}$, where

$$\bar{G} = \frac{I_o\left(\sqrt{s\,\frac{Re}{2}}\; r^*\right)}{s\; I_o\left(\sqrt{s\,\frac{Re}{2}}\right)}$$

so that

$$G = \mathcal{L}^{-1}(\bar{G}) = \mathcal{L}^{-1}\left\{\frac{I_o\left(\sqrt{s\,\frac{Re}{2}}\; r^*\right)}{s\; I_o\left(\sqrt{s\,\frac{Re}{2}}\right)}\right\}$$

By definition of the Laplace transform

$$u_2^* = \mathcal{L}^{-1}(\bar{f}\bar{G})$$

By the convolution theorem we can write

$$u_2^* = \int_o^\tau f(\tau - T)G(T)dT = \int_o^\tau f(T)G(\tau - T)dT \tag{53}$$

where

$$G(T) = \mathcal{L}^{-1}(G) = \frac{1}{2\pi i}\oint e^{sT}\,\frac{I_o\left(\sqrt{s\,\frac{Re}{2}}\; r^*\right)}{s\; I_o\left(\sqrt{s\,\frac{Re}{2}}\right)} \tag{54}$$

By expansion of the functions $I_o\left(\sqrt{s\frac{Re}{2}}\; r^*\right)$ and $I_o\left(\sqrt{s\frac{Re}{2}}\right)$ it can be seen that s = 0 is not a branch point. By applying the results of the Cauchy's residue theorem Equation 54 becomes

$$G(T) = 1 - 2\sum_{n=1}^{\infty}\frac{J_o(\alpha_n r^*)}{\alpha_n J_1(\alpha_n)}\, e^{-2\,\frac{\alpha_n^2}{Re}\,T} \tag{55}$$

where α_n are the roots of $J_o\left(\sqrt{s\,\frac{Re}{2}}\right)$ (see Appendix B for details). From Equations 51 and 55, with convolution theorem, we have

$$u^* = u_1^* - u_2^* = 2\sum_{n=1}^{\infty}\frac{J_o(\alpha_n r^*)}{\alpha_n J_1(\alpha_n)}\int_o^\tau f(\tau - T)e^{-2\,\frac{\alpha_n^2}{Re}T}\,dT$$

$$= 2\sum_{n=1}^{\infty}\frac{J_o(\alpha_n r^*)}{\alpha_n J_1(\alpha_n)}\, F_n(\tau) \tag{56}$$

where

$$F_n(\tau) = \int_0^\tau f(\tau-T)e^{-2\frac{\alpha_n^2}{Re}T}dT \tag{57}$$

Equation 44 can be written as

$$f(\tau-T) = a(1-e^{-\ell(\tau-T)})+b(\tau-T)^m e^{-k(\tau-T)}$$

Substitution of this result in Equation 57 gives

$$F_n(\tau) = a\int_0^\tau e^{-2\frac{\alpha_n^2}{Re}T}dT - ae^{-\ell\tau}\int_0^\tau e^{(\ell-\frac{2\alpha_n^2}{Re})T}dT$$

$$+b\int_0^\tau(\tau-T)^m e^{-k(\tau-T)-2\frac{\alpha_n^2}{Re}T}\,dT$$

$$= \left(\frac{aRe}{2\alpha_n^2} - \frac{aRe}{2\alpha_n^2}e^{-\frac{2\alpha_n^2}{Re}\tau}\right) - \frac{aRe}{\ell Re-2\alpha_n^2}\left(e^{-\frac{2\alpha_n^2}{Re}\tau}-e^{-\ell\tau}\right) \tag{58}$$

$$+ bI_n(\tau)$$

where

$$I_n(\tau) = \int_0^\tau(\tau-T)^m e^{-k(\tau-T)-2\frac{\alpha_n^2}{Re}T}dT \tag{59}$$

We can also write

$$F_n(\tau) = \frac{aRe}{2\alpha_n^2} + G_n(\tau) \tag{60}$$

where,

$$G_n(\tau) = bI_n(\tau) - \frac{aRe}{2\alpha_n^2}e^{-2\frac{\alpha_n^2}{Re}\tau}$$

$$- \frac{aRe}{\ell Re-2\alpha_n^2}\left(e^{-\frac{2\alpha_n^2}{Re}\tau}-e^{-\ell\tau}\right) \tag{61}$$

With Equation 60 the expression for velocity becomes

$$u^* = 2\sum_{n=1}^{\infty}\frac{J_o(\alpha_n r^*)}{\alpha_n J_1(\alpha_n)}\left(\frac{aRe}{2\alpha_n^2} + G_n(\tau)\right) \tag{62}$$

Observe that $G_n(\tau) \to 0$ as $\tau \to \infty$. Therefore, the steady state solution may be obtained from

$$u^* = aRe \sum_{n=1}^{\infty} \frac{J_o(\alpha_n r^*)}{\alpha_n J_1(\alpha_n)} \tag{63}$$

Now, let us evaluate $I_n(\tau)$. By the convolution theorem we can replace the variable τ-T with T. Then

$$I_n(\tau) = \int_o^\tau T^m e^{-kT} \cdot 2\frac{\alpha_n^2}{Re}(\tau-T)_{dT}$$

$$= e^{-2\frac{\alpha_n^2}{Re}\tau} \int_o^\tau T^m e^{-(k-2\frac{\alpha_n^2}{Re})T} dT \tag{64}$$

With Equations 58 and 64 we can determine the dimensionless velocity from Equation 56 as

$$u^* = 2 \sum_{n=1}^{\infty} \frac{J_o(\alpha_n r^*)}{\alpha_n J_1(\alpha_n)} \{\frac{aRe}{2\alpha_n^2} - \frac{aRe}{2\alpha_n^2} e^{-\frac{\alpha_n^2}{Re}\tau} - \frac{aRe}{\ell Re - 2\alpha_n^2} e^{-2\frac{\alpha_n^2}{Re}\tau}$$

$$+ \frac{aRe}{\ell Re - 2\alpha_n^2} e^{-\ell\tau} + be^{-2\frac{\alpha_n^2}{Re}\tau} \int_o^\tau T^m e^{-(k-2\frac{\alpha_n^2}{Re})T} dT\} \tag{65}$$

Equation 65 gives the velocity profile in the fully developed region. We have to integrate this velocity profile to obtain the unsteady discharge. The method of determining the unsteady discharge is discussed in the following.

C. Velocity Calculations

Define the dimensionless discharge, Q*, as the ratio Q/Q_s where, Q is the instantaneous discharge and Q_s is the steady state discharge. Then, if u is the velocity in the

fully developed region,

$$Q^* = \frac{Q}{Q_s} = \frac{2\pi \int_0^R ur\, dr}{\pi R^2 U} = 2 \int_0^1 \frac{u}{U} \frac{r}{R}\, d\left(\frac{r}{R}\right)$$

$$= 2 \int_0^1 u^* r^*\, dr^* \tag{66}$$

With the velocity profile given by Equation 65

$$Q^* = 2 \int_0^1 2 \sum \frac{J_o(\alpha_n r^*)}{\alpha_n J_1(\alpha_n)} \left(\frac{aRe}{2\alpha_n^2} + G_n(\tau)\right) r^*\, dr^*$$

$$= 4 \sum_{n=1}^{\infty} \frac{1}{\alpha_n J_1(\alpha_n)} \left(\frac{aRe}{2\alpha_n^2} + G_n(\tau)\right) \int_0^1 J_o(\alpha_n r^*) r^* dr^*$$

$$= 4 \sum_{n=1}^{\infty} \frac{1}{\alpha_n J_1(\alpha_n)} \left(\frac{aRe}{2\alpha_n^2} + G_n(\tau)\right) \frac{1}{\alpha_n} J_1(\alpha_n)$$

$$= 2\, aRe \sum_{n=1}^{\infty} \frac{1}{\alpha_n^4} + 4 \sum_{n=1}^{\infty} \frac{1}{\alpha_n^4} G_n(\tau) \tag{67}$$

As $\tau \to \infty$ the second term on the right hand side becomes zero, and the dimensionless discharge in the steady state will be given by

$$Q^* = 2\, aRe \sum_{n=1}^{\infty} \frac{1}{\alpha_n^4} \tag{68}$$

In Equation 68, as $n \to \infty$ the right hand side should approach 1. Equation 68 can be written as

$$Q^* = 2aRe \left\{\frac{1}{\alpha_1^4} + \frac{1}{\alpha_2^4} + \frac{1}{\alpha_3^4} + \frac{1}{\alpha_4^4} + \ldots.\right\} \tag{69}$$

The first four roots of $J_o(\alpha_n)$ are:

$$\alpha_1 = 2.4048 \qquad \alpha_3 = 6.6537$$

$$\alpha_2 = 5.5201 \qquad \alpha_4 = 11.7915 \tag{70}$$

With Equations 69 and 70 the dimensionless discharge in the steady state for the Reynolds number 1610 is

$$Q^* = 2 \times 0.01 \times 1610 \left\{\frac{1}{(2.4048)^4} + \frac{1}{(5.5201)^4} + \frac{1}{(8.6537)^4} + \ldots\right\} = 0.9994 \tag{71}$$

From the discharge measured in the experiment

$$Q^* = \frac{0.609}{0.609} = 1.0 \tag{72}$$

Comparison of Equations 71 and 72 indicates that the dimensionless discharge determined from theory approaches 1 as expected.

Using Equations 61 and 67 we can write the dimensionless unsteady discharge as

$$\begin{aligned} Q^* = 2aRe \sum_{n=1}^{\infty} \frac{1}{\alpha_n^4} + 4 \sum_{n=1}^{\infty} \frac{1}{\alpha_n^2} \Big\{ be^{-2\frac{\alpha_n^2}{Re}\tau} \int_o^\tau T^m e^{-kT + \frac{2\alpha_n^2}{Re}T} dT \\ - \frac{aRe}{2\alpha_n^2} e^{-\frac{2\alpha_n^2}{Re}\tau} - \frac{aRe}{\ell Re - 2\alpha_n^2} \left(e^{-\frac{2\alpha_n^2}{Re}\tau} - e^{-\ell\tau}\right) \Big\} \\ = 4 \sum_{n=1}^{\infty} \Big\{ \frac{aRe}{2\alpha_n^4} - \frac{aRe}{2\alpha_n^4} e^{-\frac{2\alpha_n^2}{Re}\tau} - \frac{aRe\, e^{-\frac{2\alpha_n^2}{Re}\tau}}{(\ell Re - 2\alpha_n^2)\alpha_n^2} \\ + \frac{aRe\, e^{-\ell\tau}}{(\ell Re - 2\alpha_n^2)\alpha_n^2} + \frac{b}{\alpha_n^2} \int_o^\tau \left(T^m e^{-kT + \frac{2\alpha_n^2}{Re}T - \frac{2\alpha_n^2}{Re}\tau}\right) dT \Big\} \end{aligned} \tag{73}$$

By the principle of continuity, and by the fact that the entrance velocity, u_o, is uniform over the cross-section of the inlet, we can express the unsteady discharge by the equation

$$Q = \pi R^2 u_o \tag{74}$$

The steady state discharge is given by

$$Q_s = \pi R^2 U$$

Then the dimensionless discharge becomes

$$Q^* = \frac{Q}{Q_s} = \frac{\pi R^2 u_o}{\pi R^2 U} = \frac{u_o}{U} = u_o^* \tag{75}$$

The ratio u_o/U has been defined as the dimensionless unsteady entrance velocity, u_o^*. From Equations 73 and 75 we will have

$$u_o^* = 4 \sum_{n=1}^{\infty} \{\frac{aRe}{2\alpha_n^4} - \frac{aRe}{2\alpha_n^4} e^{-\frac{2\alpha_n^2}{Re}\tau} - \frac{aRe\ e^{-\frac{2\alpha_n^2}{Re}\tau}}{(\ell Re - 2\alpha_n^2)\alpha_n^2}$$

$$+ \frac{aRe\ e^{-\ell\tau}}{(\ell Re - 2\alpha_n^2)\alpha_n^2} + \frac{b}{\alpha_n^2} \int_0^{\tau} (T^m e^{-kT} + \frac{2\alpha_n^2}{Re} T - \frac{2\alpha_n^2}{Re}\tau) dT\} \tag{76}$$

For a given Reynolds number and the corresponding pressure-gradient function $f(\tau) = a(1-e^{-\ell\tau}) + b\tau^m e^{-k\tau}$, the unsteady entrance velocity can be determined from Equation 76. For the pressure gradient functions described in Equations 41 and 42, the integral of the last term in Equation 76 cannot be obtained explicitly. Hence, the evaluation of u_o^* by Equation 76 was programmed on the computer. In the evaluation of u_o^* the first sixty roots (i.e., n = 1,60) of the Bessel function $J_o(\alpha_n)$ were considered. The summation of the series was stopped when the difference in the sums up to any consecutive roots was less than 0.00001. That is, when $|s_{n+1} - s_n| < 0.00001$. The values of the roots of $J_o(\alpha_n)$

were supplied by the Computer Science Library of the Iowa State University. The listing of the computer program used in the determination of u_o^* and the results are presented in Appendix C. The unsteady entrance velocities for the Reynolds numbers 1610 and 700 are shown in Figures 29 and 30.

As expected Figures 29 and 30 show that the curves representing the velocity development are not similar in shape to those for the pressure gradient. While the pressure gradient increased rapidly there was no corresponding exceedingly rapid rise in the velocity. In the case of the Reynolds number 1610 the pressure gradient reached the steady state approximately at $\tau = 47$, but at this τ the corresponding velocity was approximately 72 per cent of the steady state velocity. The behavior was similar in the case of the Reynolds number 700. The lagging of the velocity development confirms that the velocity does not respond to the pressure gradient instantaneously.

In the set of Equations 37 we also need to know $du_o^*/d\tau$. Differentiation of u_o^* in the Equation 76, with respect to τ gives

$$\frac{du_o^*}{d\tau} = 4 \sum_{n=1}^{\infty} \{\frac{2\alpha_n^2}{Re} \frac{aRe}{2\alpha_n^4} e^{-\frac{2\alpha_n^2}{Re}\tau} + \frac{2\alpha_n^2}{Re} \frac{aRe}{(\ell Re-2\alpha_n^2)\alpha_n^2} e^{-\frac{2\alpha_n^2}{Re}\tau}$$

$$- \frac{a\ell Re}{(\ell Re-2\alpha_n^2)\alpha_n^2} e^{-\ell\tau} + \frac{b}{\alpha_n^2} \tau^m e^{-k\tau+\frac{2\alpha_n^2}{Re}\tau - \frac{2\alpha_n^2}{Re}\tau}\}$$

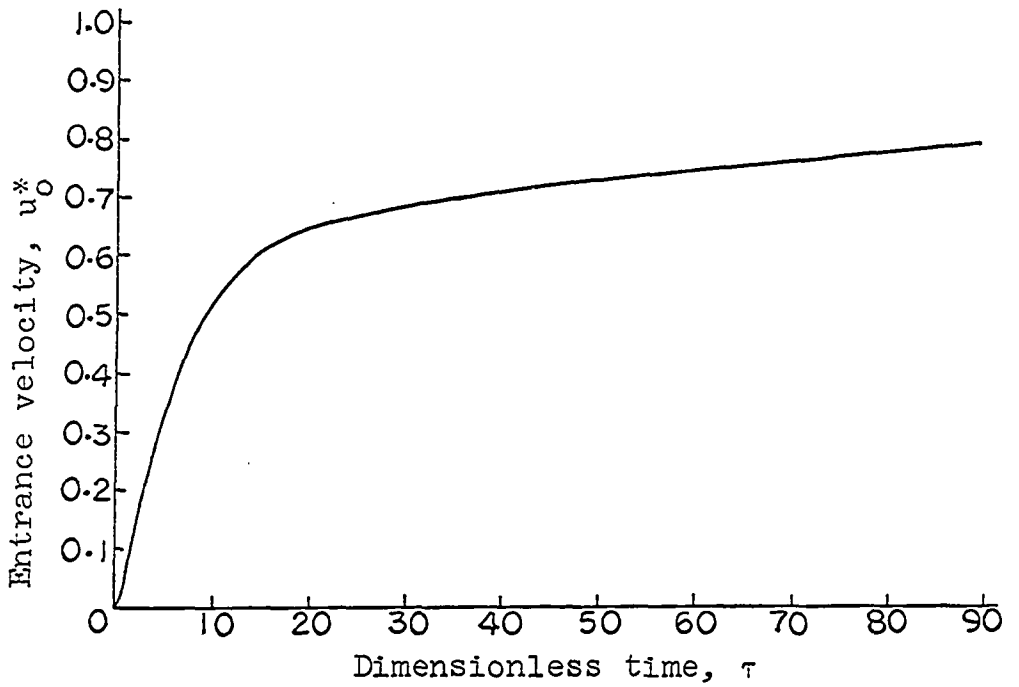

Fig. 29. Unsteady entrance velocity, Re = 1610.

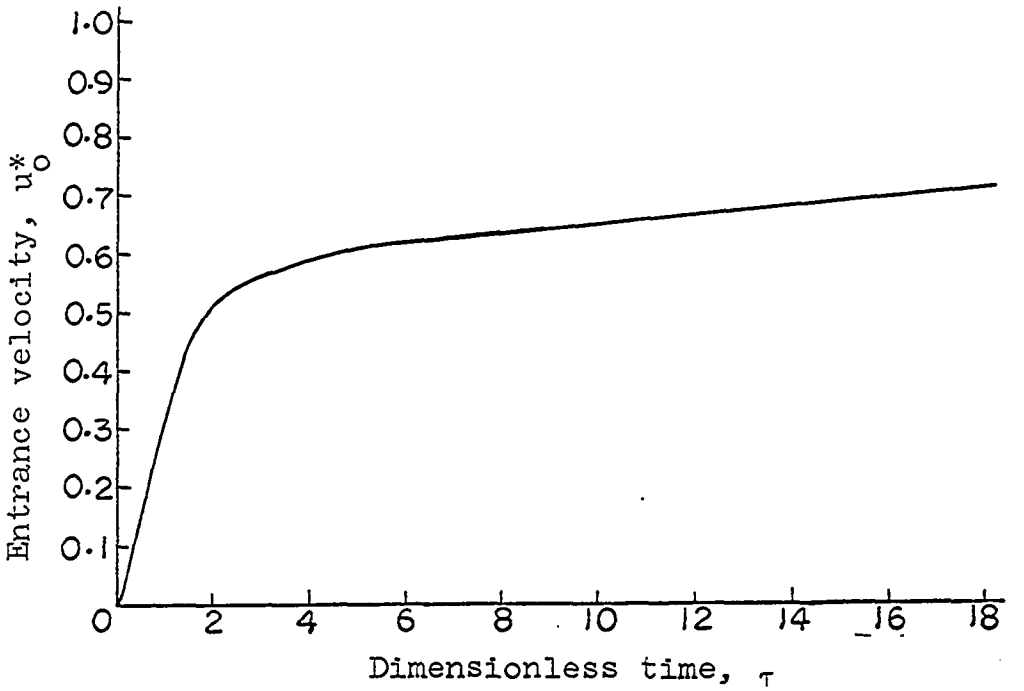

Fig. 30. Unsteady entrance velocity, Re = 700.

$$= 4 \sum_{n=1}^{\infty} \{ \frac{a}{\alpha_n^2} e^{-\frac{2\alpha_n^2}{Re}\tau} + \frac{2a}{\imath Re - 2\alpha_n^2} e^{-\frac{2\alpha_n^2}{Re}\tau}$$

$$- \frac{a \imath Re}{(\imath Re - 2\alpha_n^2)\alpha_n^2} e^{-\imath\tau} + \frac{b}{\alpha_n^2} \tau^m e^{-k\tau} \} \qquad (77)$$

Equation 77 can be written as

$$\frac{du_o^*}{d\tau} = 4(\frac{a}{\alpha_1^2} e^{-\frac{2\alpha_1^2}{Re}\tau} + \frac{a}{\alpha_2^2} e^{-\frac{2\alpha_2^2}{Re}\tau} + \ldots.)$$

$$+4 \, (\frac{2a}{\imath Re - 2\alpha_1^2} e^{-\frac{2\alpha_1^2}{Re}\tau} + \frac{2a}{\imath Re - 2\alpha_2^2} e^{-\frac{2\alpha_2^2}{Re}\tau} + \ldots)$$

$$-4 \, (\frac{a \imath Re}{(\imath Re - 2\alpha_1^2)\alpha_1^2} e^{-\imath\tau} + \frac{a \imath Re}{(\imath Re - 2\alpha_2^2)\alpha_2^2} e^{-\imath\tau} + \ldots)$$

$$+4 \, (\frac{b}{\alpha_1^2} \tau^m e^{-k\tau} + \frac{b}{\alpha_2^2} \tau^m e^{-k\tau} + \ldots) \qquad (78)$$

Using the roots of the Bessel function $J_o(\alpha_n)$ each series in the parenthesis of Equation 78 was evaluated. The summation of each series was cutoff when the difference between the consecutive terms of the series was less than 0.00001 with $\tau = 0$. With this method of evaluation, for the flow corresponding to the Reynolds number 1610, we have obtained

$$\frac{du_o^*}{d\tau} = 0.09308 \, \tau^{0.18} e^{-0.16\tau} - 0.00843 \, e^{-0.25\tau}$$

$$+ 0.00712 \, e^{-0.0072\tau} + 0.00155 \, e^{-0.038\tau} + \ldots. \qquad (79)$$

In the same manner, for the flow corresponding to the

Reynolds number 700, we have obtained

$$\frac{du_o^*}{d\tau} = 0.98734\ \tau^{0.52} e^{-1.175\tau} - 0.00096\ e^{-0.62\tau} + 0.01669\ e^{-0.017\tau} + \ldots \quad (80)$$

Using u_o^* and the corresponding $du_o^*/d\tau$, for the Reynolds numbers 1610 and 700, Equations 37 were solved by employing the NODE program as outlined in Chapter III. More terms than shown in Equations 79 and 80 were used for $du_o^*/d\tau$. The unsteady velocity u_o^* at any instant, for use in the NODE program, was obtained by interpolating between the appropriate discrete values of τ. The interpolation was done with the subroutines ALI and ATSM incorporated into the NODE program. The results pertaining to this solution are presented in the next chapter.

VI. RESULTS AND DISCUSSION

The solution of the system of Equations 37 obtained with the help of the NODE program described earlier is presented in the following in the form of families of characteristics. The boundary layer development, the velocity profiles at various instants and axial positions, and the instantaneous entrance lengths are determined from these characteristics. The instantaneous entrance lengths obtained from the computer solution are compared with those estimated from the experimental results. Also, the steady state solution for the entrance length is compared with some of the solutions available in the fluid mechanics literature.

A. Boundary Layer Growth, Instantaneous Entrance Length and Velocity Profile

The families of characteristics presented in Figures 31 and 36 are from the solution for the cases of the Reynolds numbers 1610 and 700, respectively. The solution for the flow with the Reynolds number 1610 will be discussed in detail. In Figure 31 we have a family of characteristics in the ξ-τ space obtained with various initial values along the τ and ξ axes. The boundary layer thickness, η, varies along each characteristic. These characteristics can be replotted with τ and ξ versus η, as shown in Figures 32 and 33, respectively. If the boundary layer thickness is desired

at any point on a characteristic, it can be determined from the corresponding replotted curve.

For example, let the development of the boundary layer along the tube at $\tau = 30$ be required. In Figure 31 the line $\tau = 30$ cuts various characteristics at A, B, C, D and E, and ξ_A, ξ_B, ξ_C, ξ_D and ξ_E are the corresponding axial positions. The boundary layer thickness at A, B, and C can be obtained from the appropriate characteristics in Figure 32. These are the boundary layer thicknesses at ξ_A, ξ_B and ξ_C. The boundary layer thickness at C, D and E can be obtained from the appropriate characteristics in Figure 33. In Figure 33 it can be observed that the boundary layer thickness corresponding to the points C, D and E is constant, although the points are at various axial distances. This nature of the boundary layer growth can be observed for any τ. The boundary layer growth at various values of τ is presented in Figure 34.

Consistent with the mode of development of the boundary layer described above, the ξ-τ space of Figure 31 is divided into two regions by the characteristic passing through the origin. The two regions are designated as Region I and Region II. In Region I the boundary layer thickness (η) is a function of both axial position (ξ) and time (τ). At a fixed τ, η is a function of ξ and at a fixed ξ, η is a function of τ. This behavior, which can be observed in

Figure 34, is in contrast with the result obtained for the case of constant entrance velocity in that the boundary layer thickness, at a fixed axial position, is constant for all time (Figure 6). The time-dependence of the boundary layer thickness at a fixed axial position can be attributed to the time-dependence of the entrance velocity. In Region II the boundary layer thickness, at any particular time, is independent of the axial position. At any instant, the axial distance beyond which the boundary layer thickness no longer depends upon the axial position is the so-called entrance length. Thus, the characteristic through the origin that divides the ξ-τ space into Region I and Region II gives the instantaneous entrance length. The entrance lengths at τ = 10, 20 and 30 are shown in Figure 34.

Figure 34 indicates that, at a position corresponding to a point on the characteristic through the origin, there is an abrupt transition from the boundary layer thickness being a function of time and axial distance to a function of time alone. In reality such an abrupt transition does not exist. Although the solution of the integral momentum equation indicates an abrupt change in the boundary layer thickness along the characteristic through the origin, a gradual transition seems likely.

At any axial position the development of velocity profile with respect to time can be obtained by considering Equations

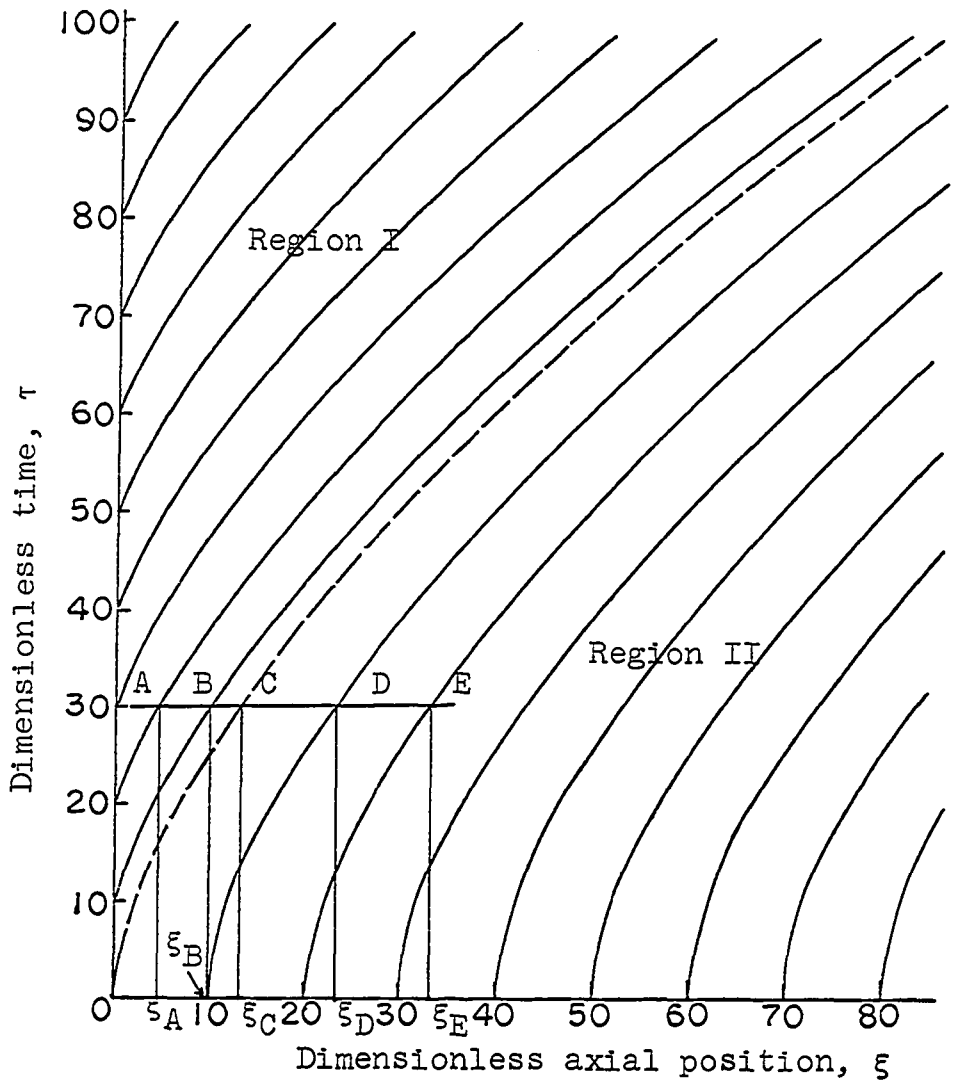

Fig. 31. Characteristics in ξ-τ space, Re = 1610.

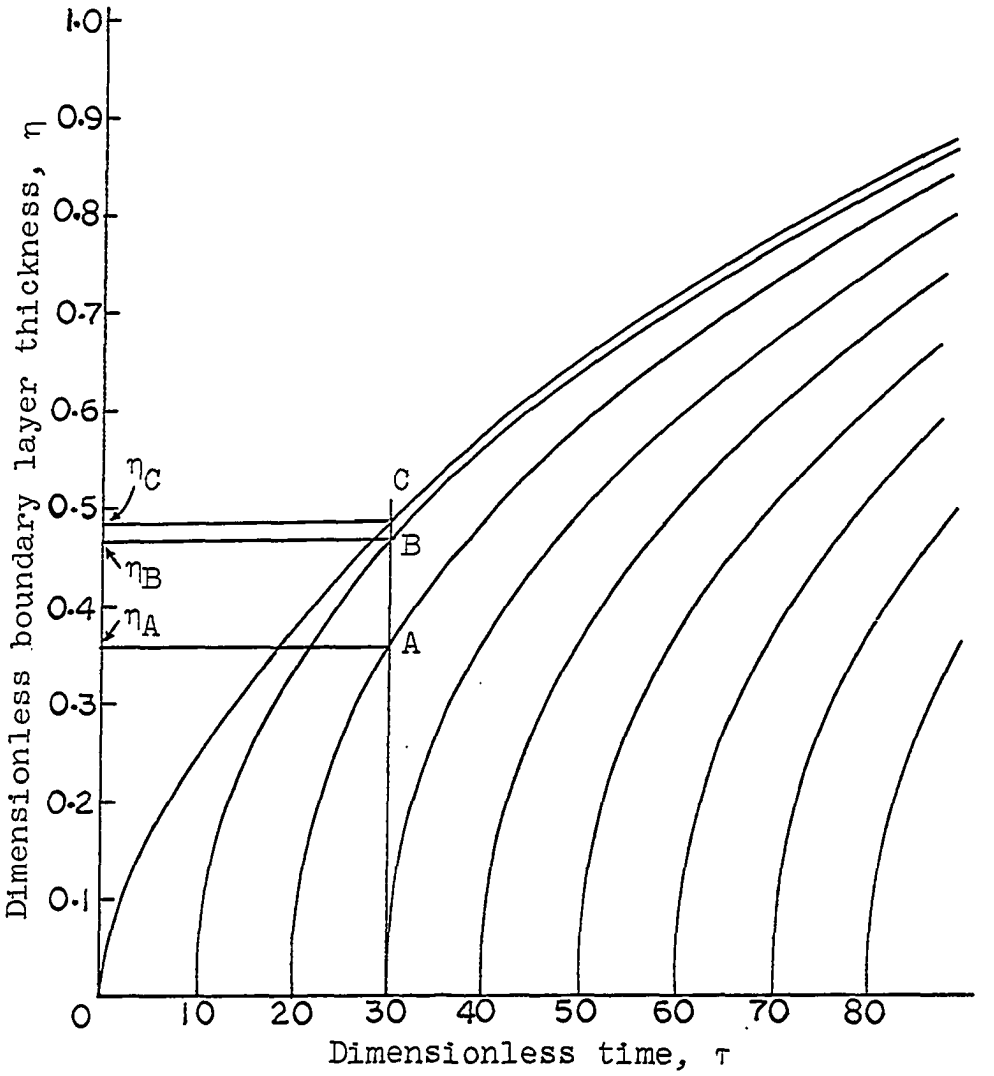

Fig. 32. Variation of boundary layer thickness with time, Re = 1610.

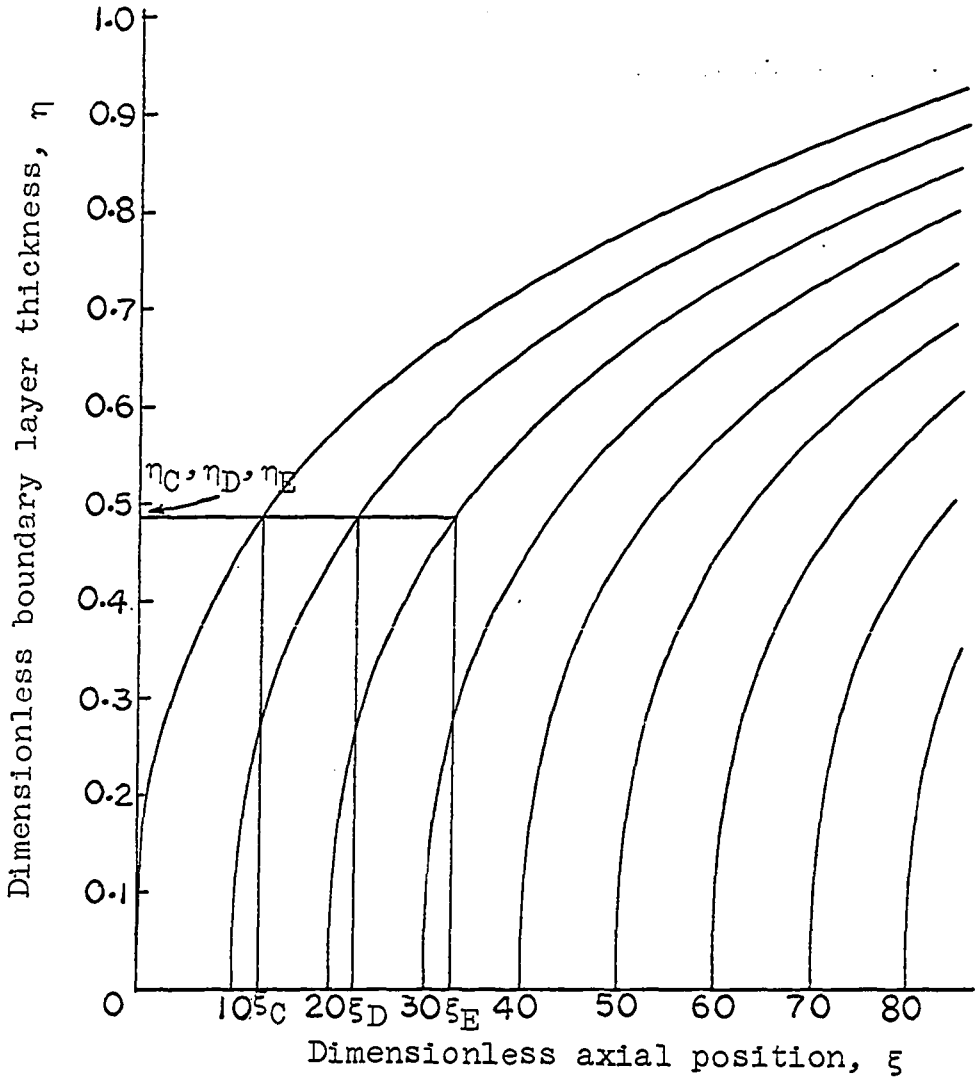

Fig. 33. Variation of boundary layer thickness with axial position, Re = 1610.

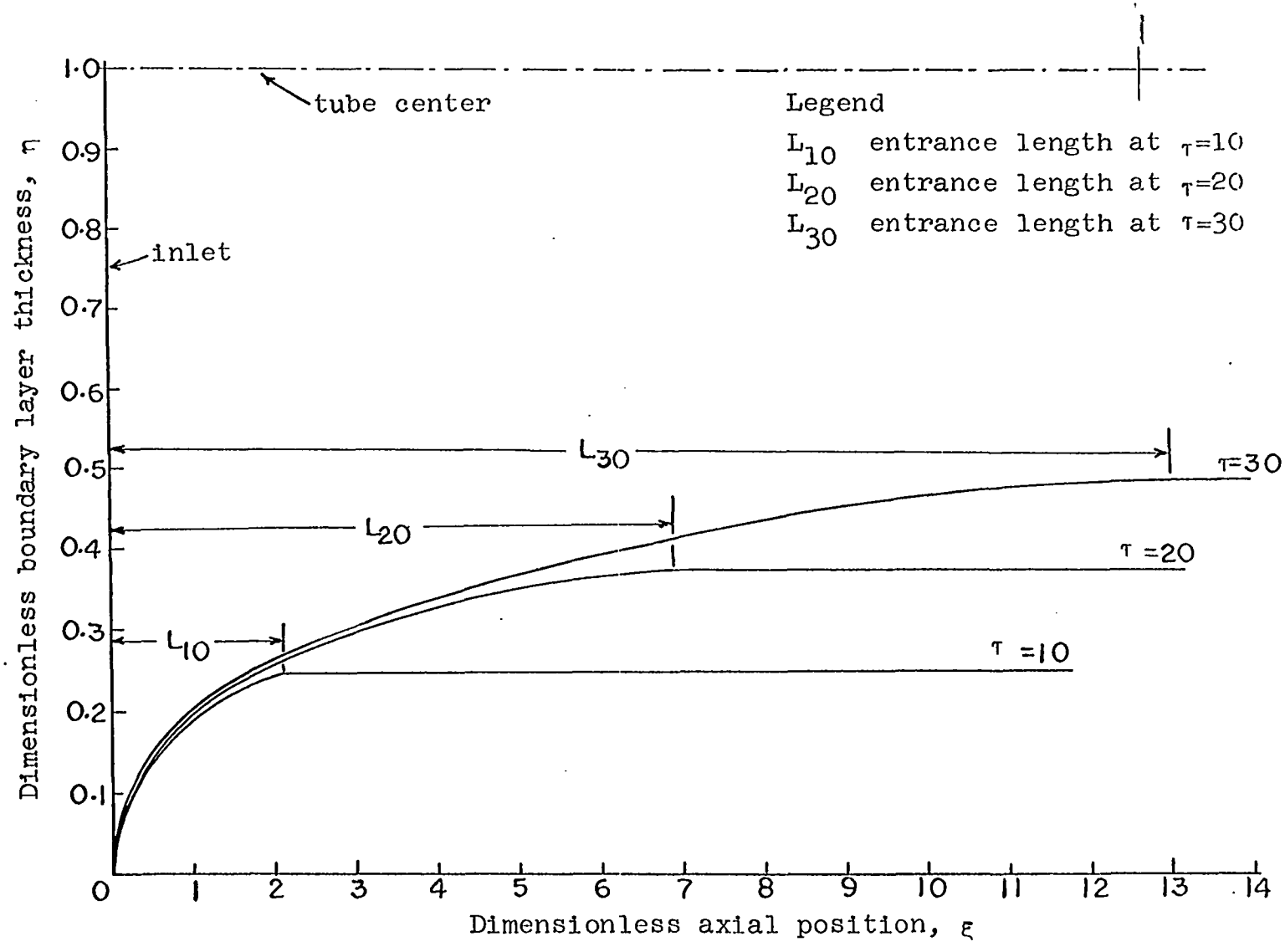

Fig. 34. Boundary layer development and instantaneous entrance lengths, Re=1610.

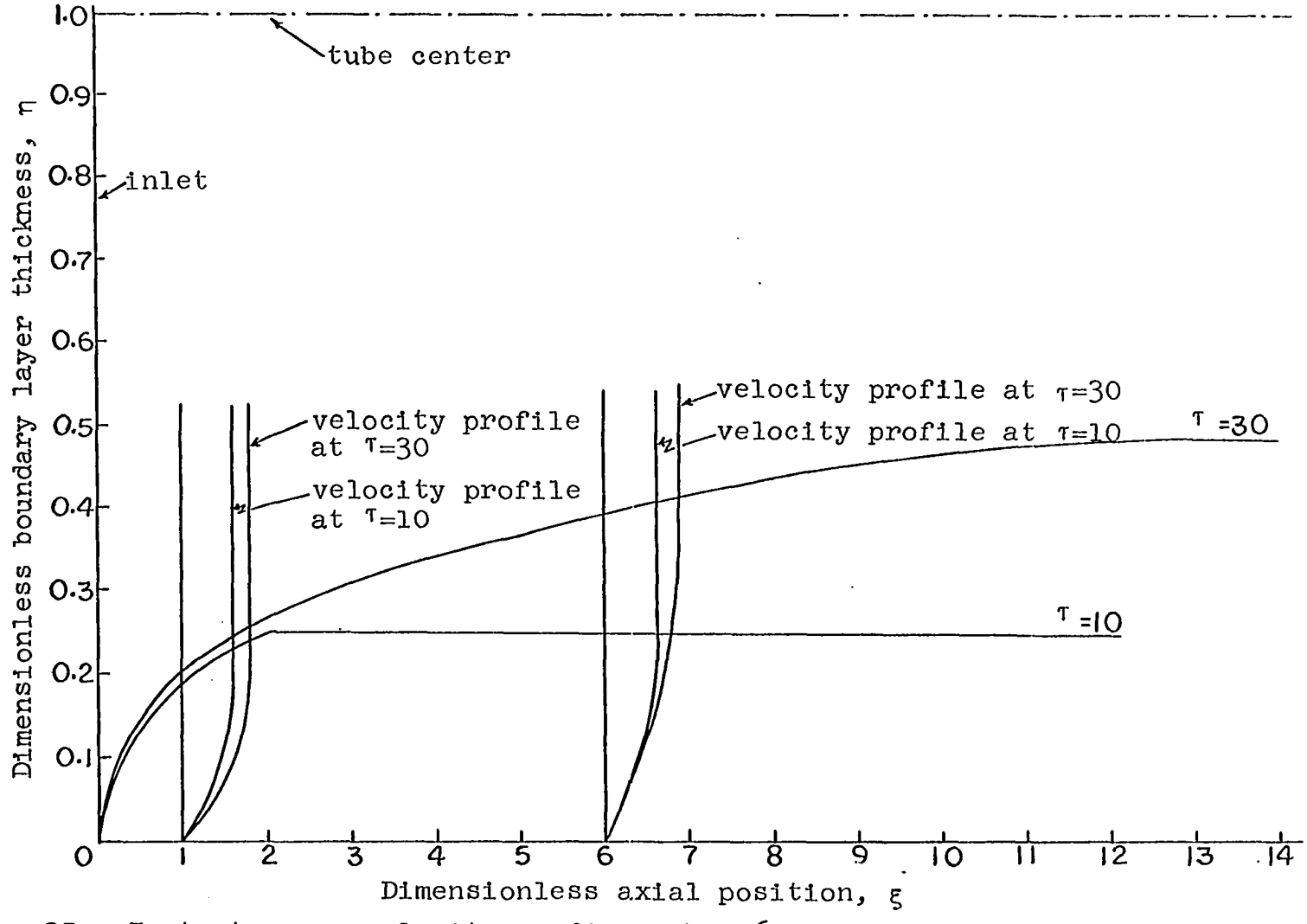

Fig. 35. Instantaneous velocity profiles, Re=1610.

9 and 21:

$$\frac{u}{u_1} = 2\frac{y}{\delta} - \frac{y^2}{\delta^2} \tag{9}$$

$$\frac{u_o}{u_1} = 1 - \frac{2}{3}\frac{\delta}{R} + \frac{1}{6}\frac{\delta^2}{R^2} \tag{21}$$

Equation 9 can be written as

$$\frac{u/U}{u_1/U} = 2\frac{y/R}{\delta/R} - \frac{y^2/R^2}{\delta^2/R^2} \tag{81}$$

Equation 21 can be written as

$$\frac{u_o/U}{u_1/U} = 1 - \frac{2}{3}\frac{\delta}{R} + \frac{1}{6}\frac{\delta^2}{R^2} \tag{82}$$

The quantities u_o/U, u/U and δ/R have been defined as u_o^*, u^* and η respectively. Now, by defining u_1/U and y/R as u_1^* and y^*, respectively, and by eliminating u_1^* from Equations 81 and 82 we can write

$$u^* = \frac{u_o^*}{1 - \frac{2}{3}\eta + \frac{1}{6}\eta^2}\left(2\frac{y^*}{\eta} - \frac{y^{*2}}{\eta^2}\right) \tag{83}$$

From Equation 83 we can determine the dimensionless velocity, u^*, in the boundary layer at any distance y^* from the wall. u_o^* and η required in Equation 83 are determined from Figures 29 and 34, respectively. It can be observed that at $y^* = \eta$ Equation 83 gives $u^* = u_o^*/(1 - \frac{2}{3}\eta + \frac{1}{6}\eta^2) = u_1^*$. That is, at the edge of the boundary layer the velocity in the boundary layer equals the velocity in the irrotational core. The velocity profiles determined from Equation 83, for various times and axial positions, are illustrated in Figure 35.

The procedure described in the foregoing discussion is repeated for the characteristics associated with the Reynolds number 700 (Figure 36). Figures 37 and 38 present the characteristics replotted with τ and ξ against η, and Figures 39 and 40 illustrate the boundary layer growth, and velocity profiles respectively.

B. Comparison of Theoretical and Experimental Results

In Table 4 the theoretical, time-dependent entrance lengths for the Reynolds numbers 1610 and 700 are presented. From the experimental pressure-drop data tabulated in Tables 7 and 8 in Appendix D the experimental entrance lengths at various instants were determined by identifying the lengths beyond which the pressure gradient remained constant. Figure 41 illustrates the method of determining the entrance length from the experimental data for a particular time. The entrance length is measured from the position of the first tap on the test section since the curvature of the inlet joins the inside wall of the test section tangentially at this position (see Figure 14). It is difficult to determine the instantaneous entrance length precisely because the instantaneous pressure gradient, which varies near the entrance, changes over smoothly to a constant value at a downstream position. Figures 42 and 43 illustrate the

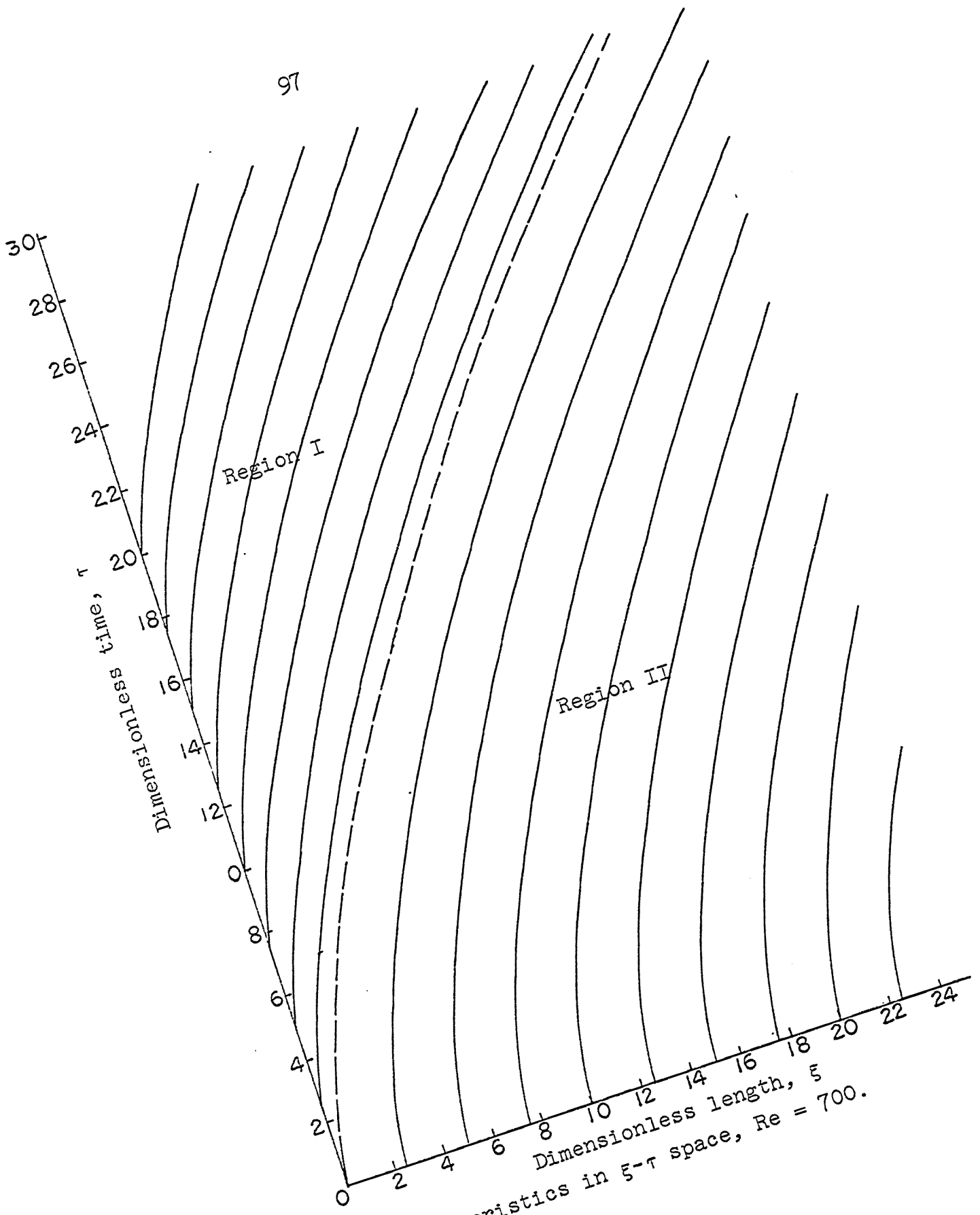

Fig. 36. Characteristics in ξ-τ space, Re = 700.

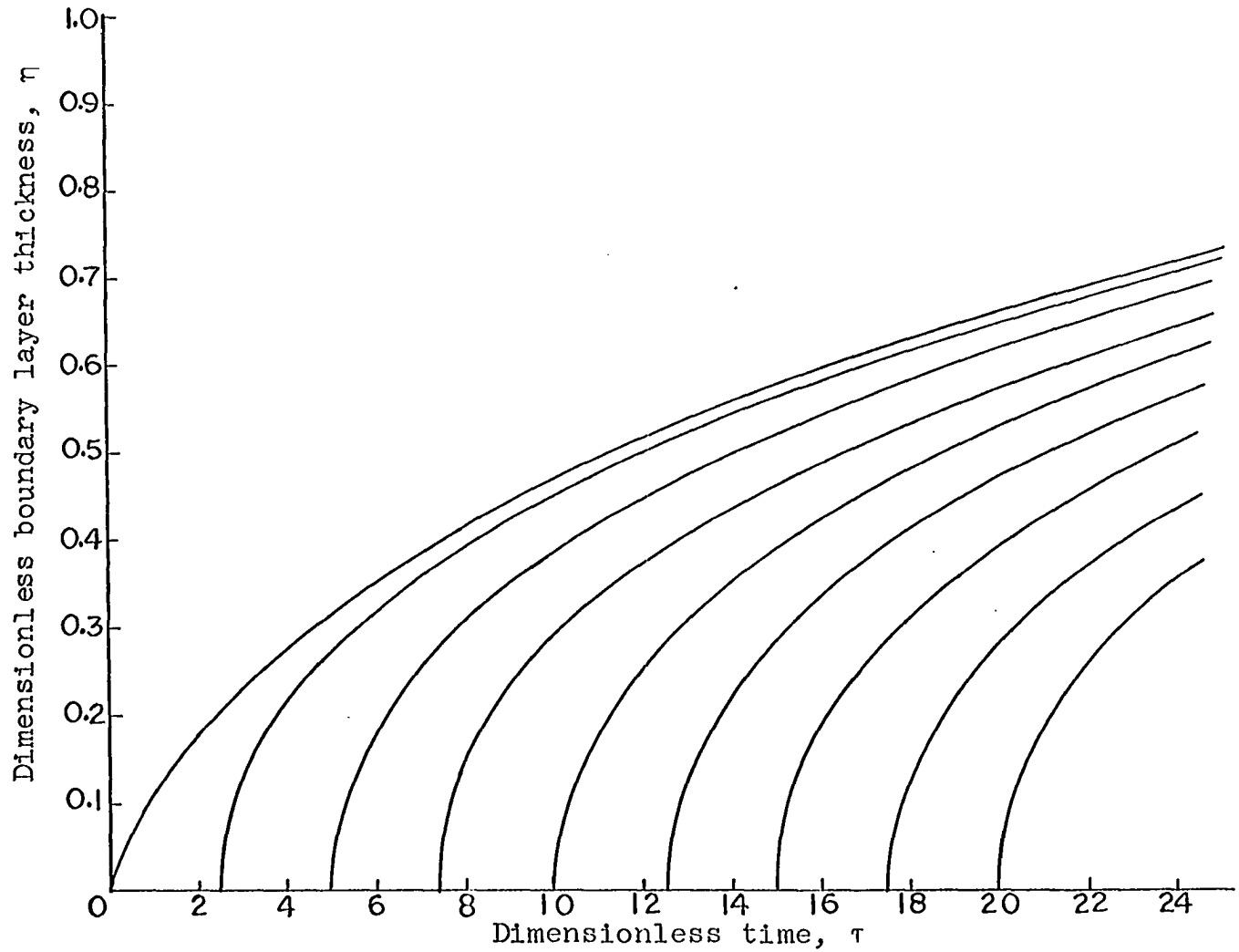

Fig. 37. Variation of boundary layer thickness with time, Re = 700.

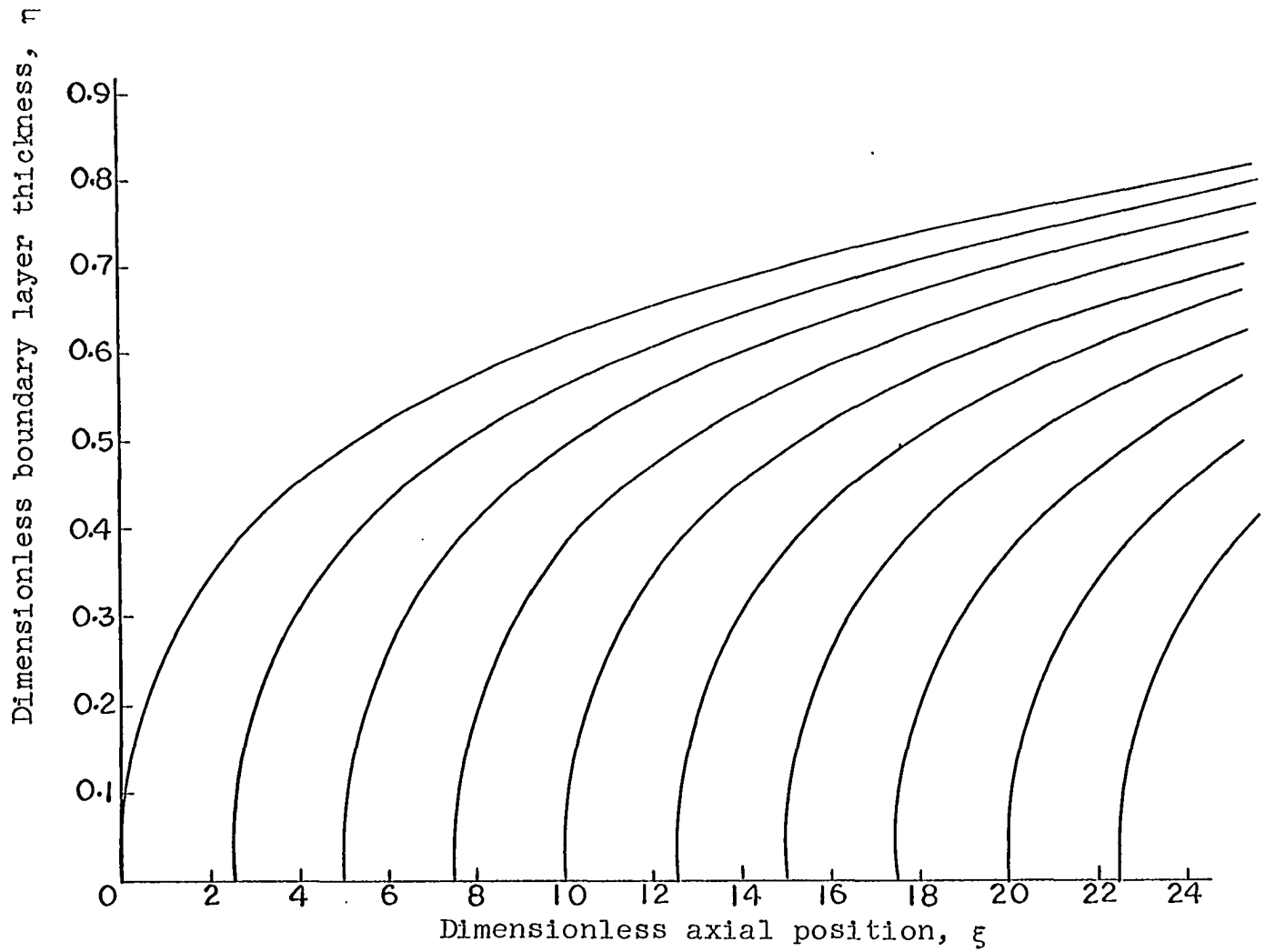

Fig. 38. Variation of boundary layer thickness with axial position, Re = 700.

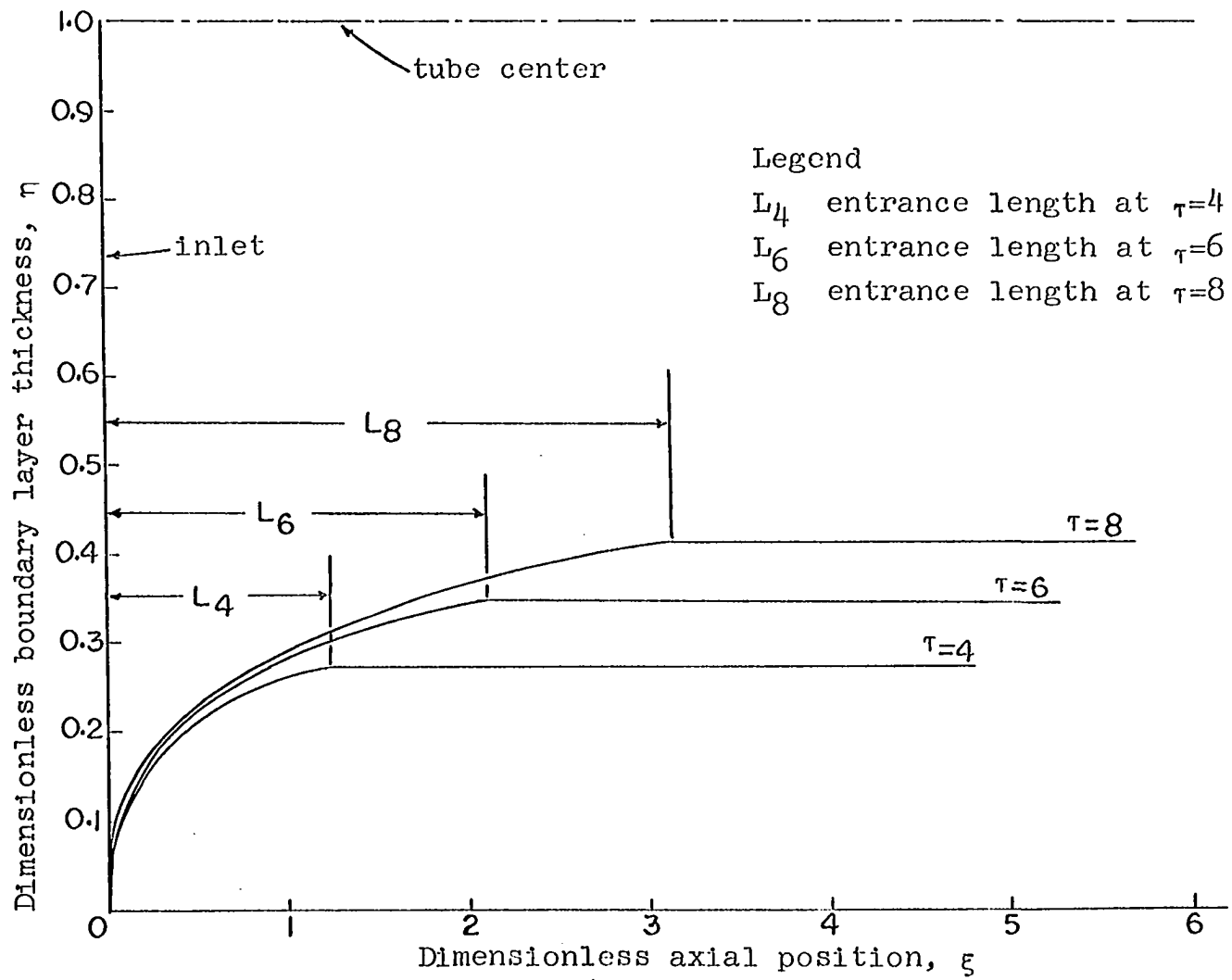

Fig. 39. Boundary layer development and instantaneous entrance lengths, Re=700.

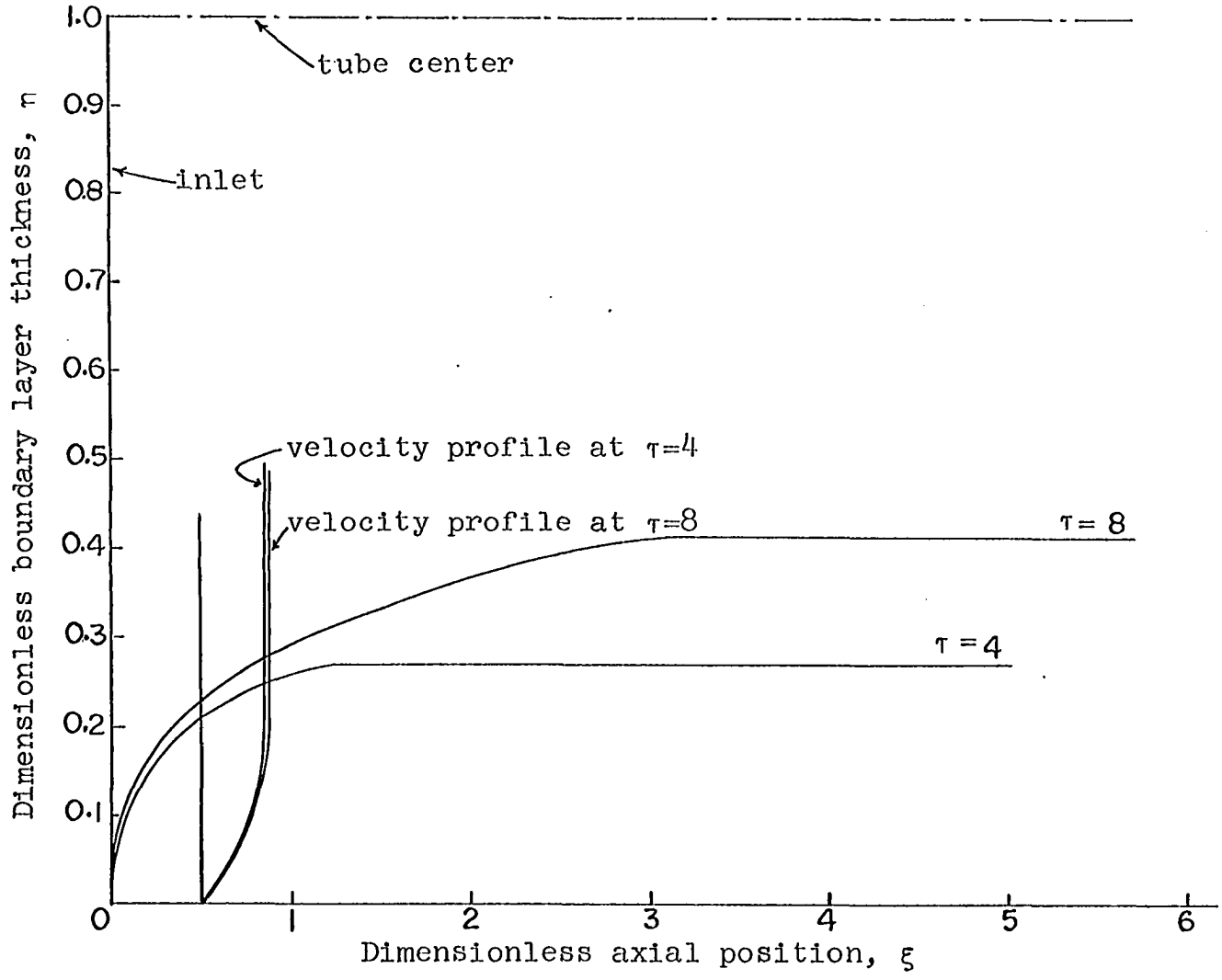

Fig. 40. Instantaneous velocity profiles, Re = 700.

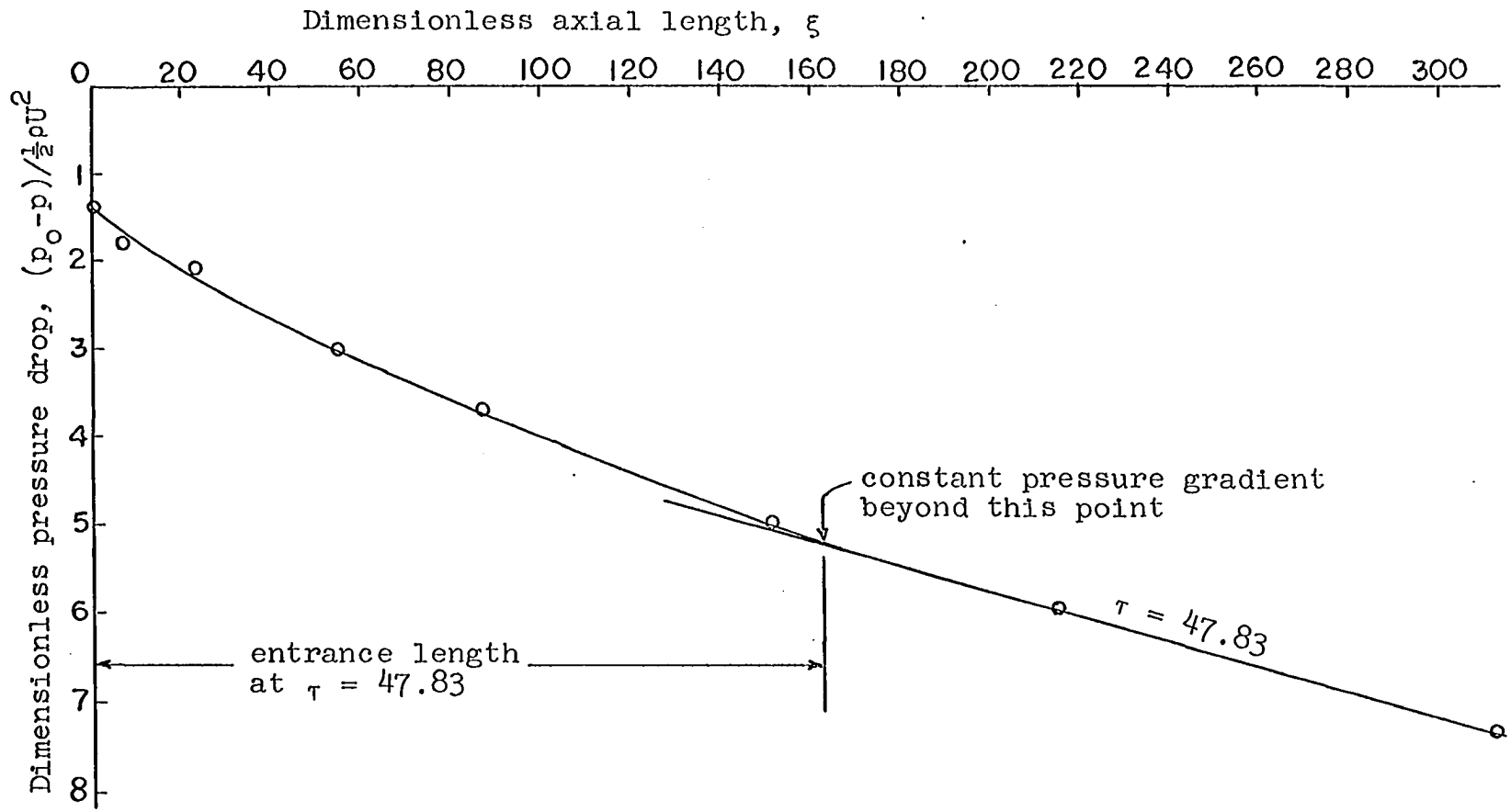

Fig. 41. Method of determination of the entrance length from the experimental pressure drop.

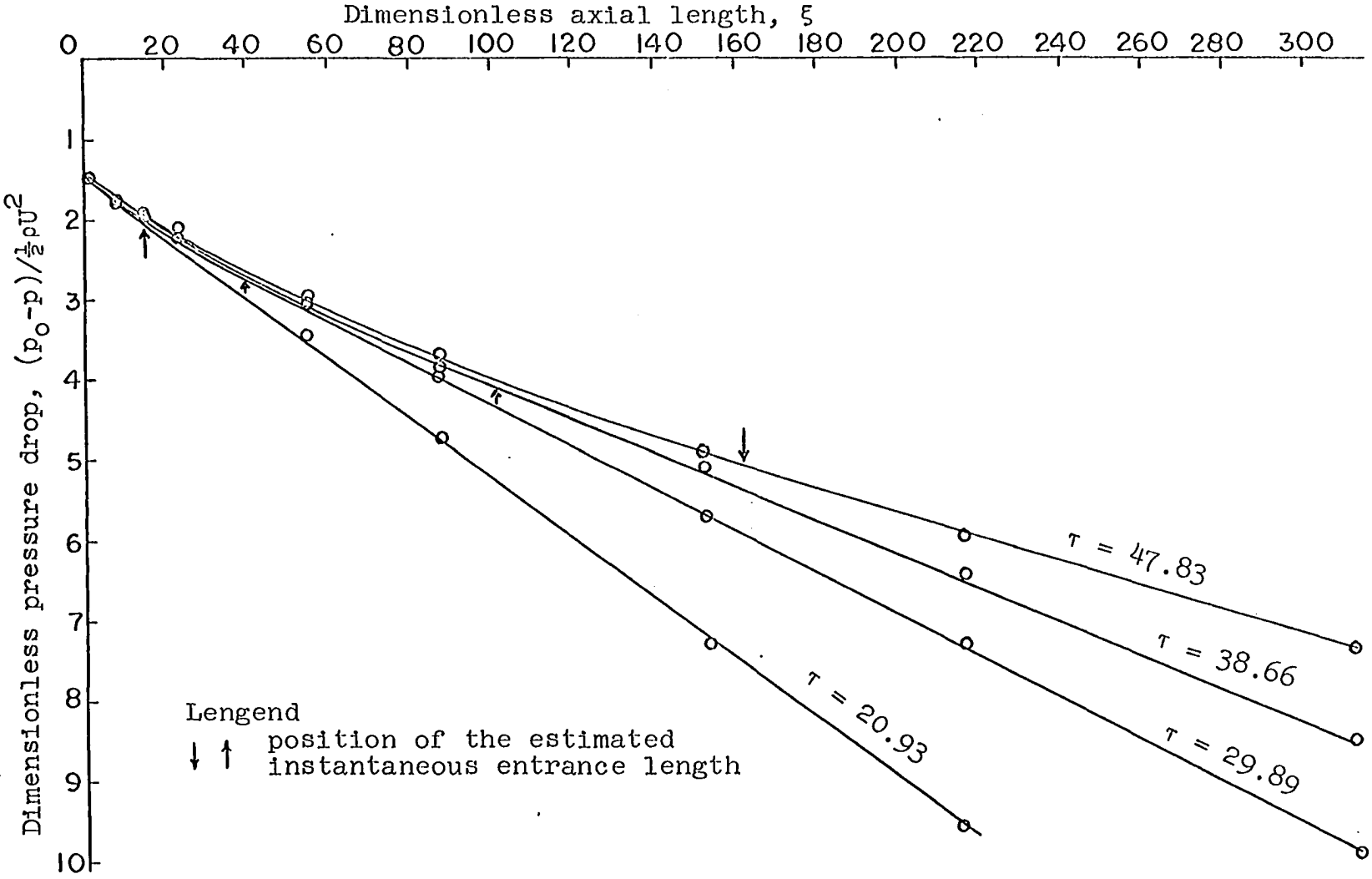

Fig. 42. Entrance lengths for large time from the experimental data, Re = 1610.

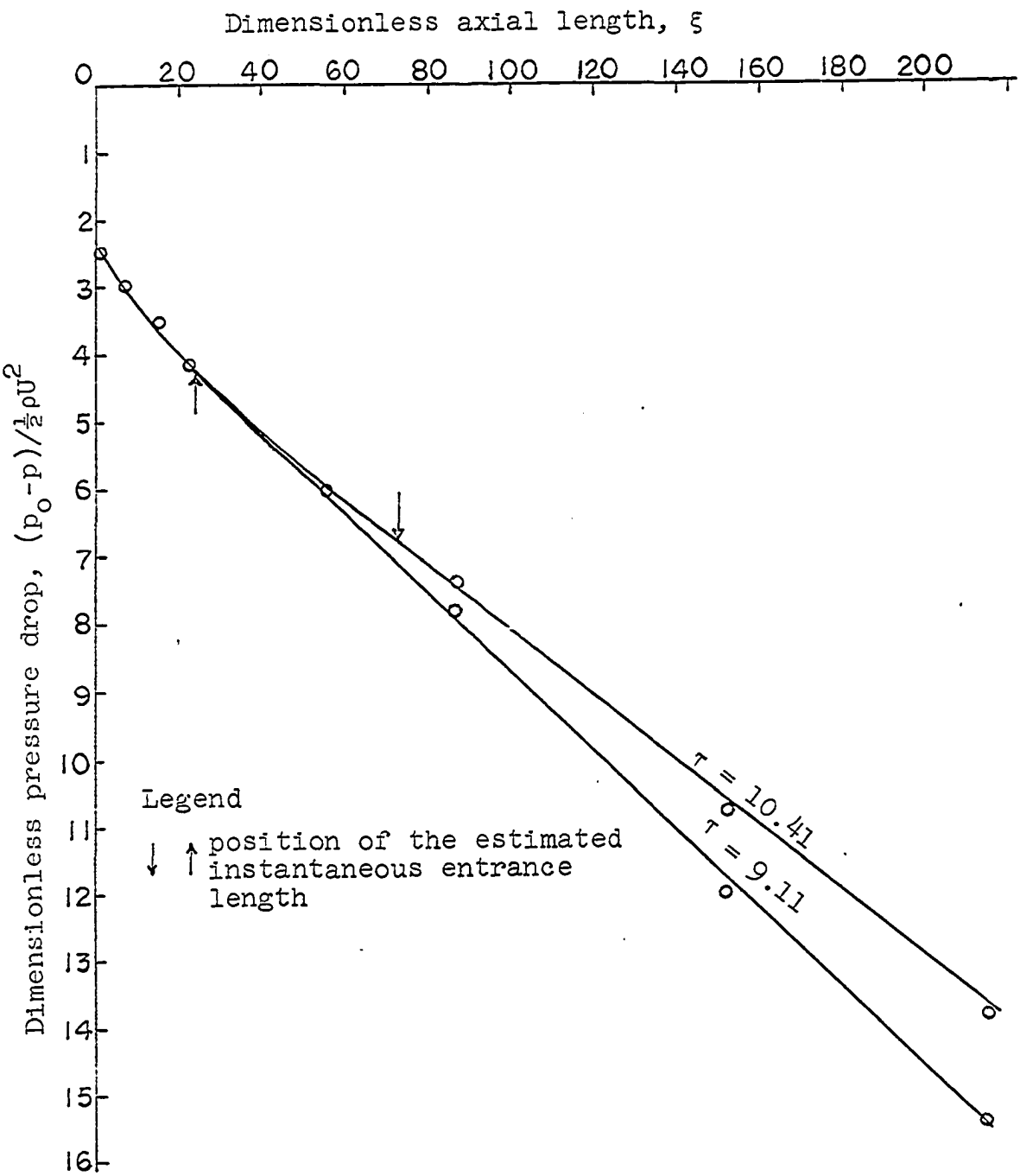

Fig. 43. Entrance lengths for large time from the experimental data, Re = 700.

Table 4. Dimensionless, theoretical, time-dependent entrance lengths. Reynolds number 1610 and 700

Re = 1610		Re = 700	
Time (τ)	Entrance length (ξ)	Time (τ)	Entrance length (ξ)
0.16	0.0003	0.15	0.0009
0.28	0.0009	0.28	0.0042
0.59	0.0049	0.33	0.0059
1.78	0.0546	0.38	0.0086
2.03	0.0719	0.73	0.0383
4.39	0.3677	0.84	0.0519
6.36	0.7799	1.59	0.2007
9.39	1.6704	3.20	0.7348
13.76	3.4030	4.37	1.2327
19.47	6.2905	6.46	2.2639
26.25	10.4226	8.84	3.6247
33.75	15.7243	9.69	4.1502
41.73	22.0936	10.56	4.7129
45.85	25.6543	13.29	6.6374
54.26	33.4944	17.23	9.7997
71.52	51.7794	19.29	11.6484
80.25	62.1035	24.67	17.0124
88.98	73.1304	31.30	24.5547
97.69	84.7950	40.00	35.6162
114.84	109.6140	48.29	47.0921

experimental entrance lengths thus determined for relatively large times for the Reynolds numbers 1610 and 700, respectively. In Figures 44 and 45 are determined entrance lengths for relatively small times for the Reynolds numbers 1610 and 700, respectively. A comparison of the theoretical and

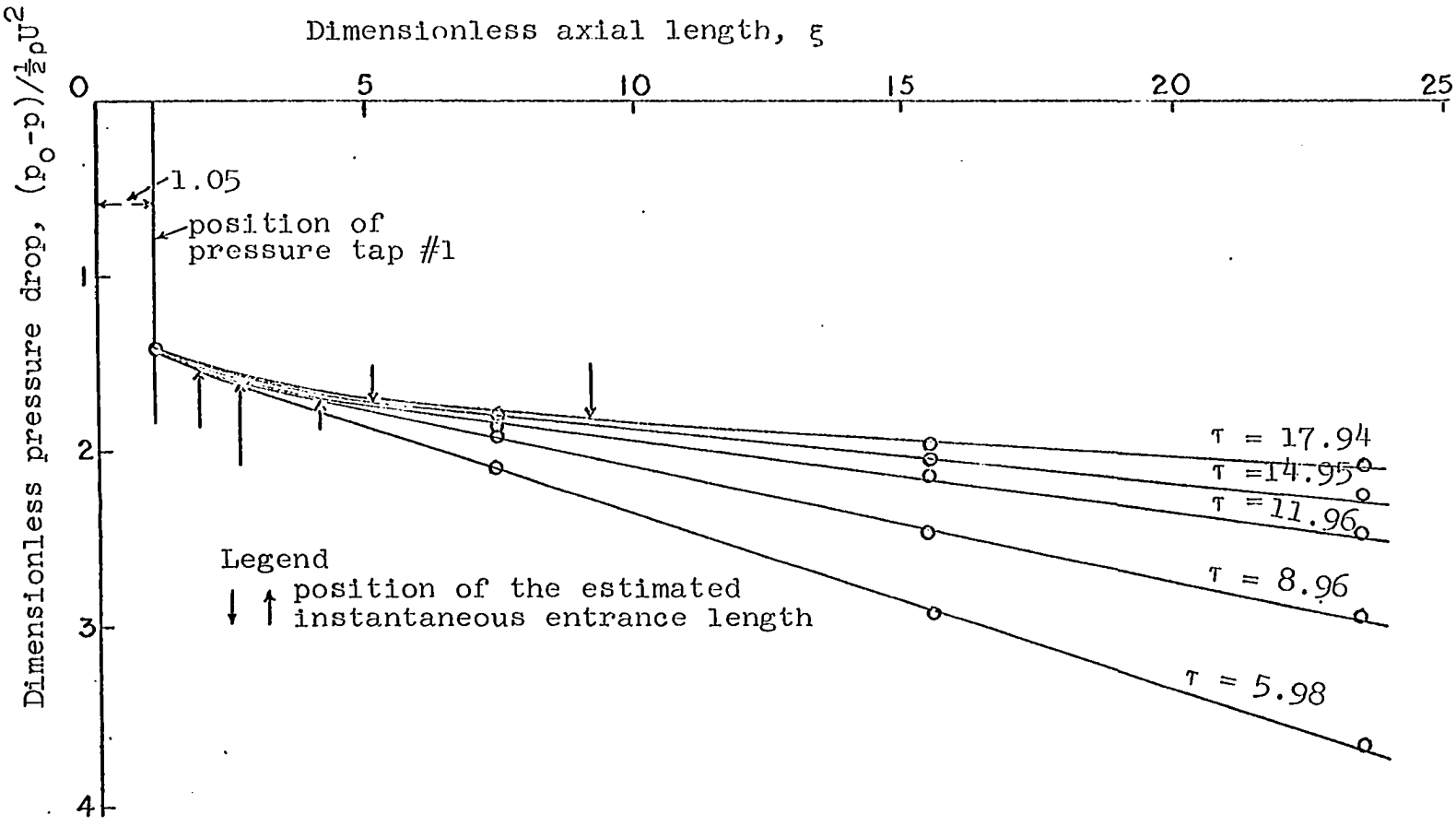

Fig. 44. Engrance lengths for small time from the experimental data, Re = 1610.

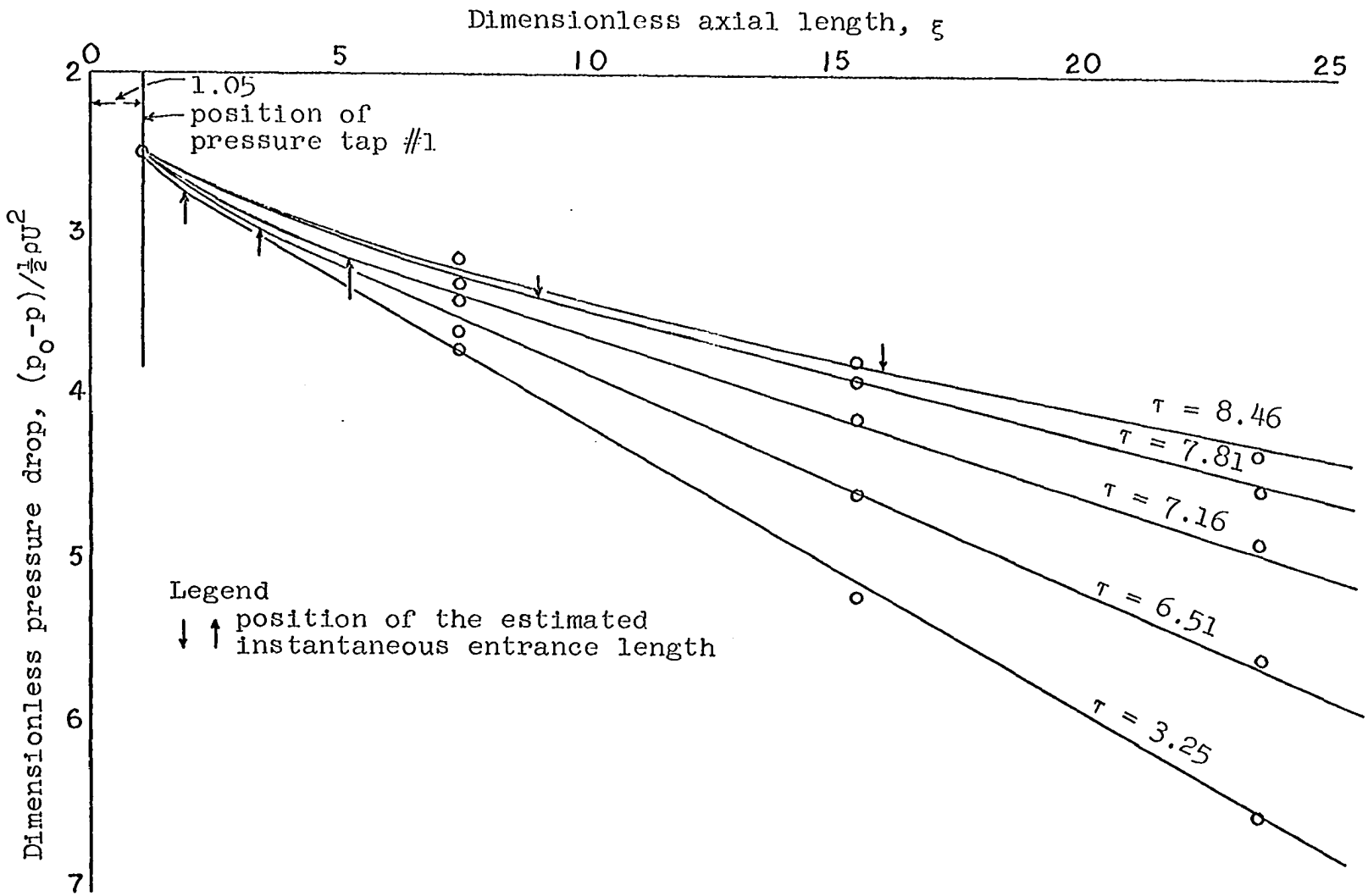

Fig. 45. Entrance lengths for small time from the experimental data, Re =700.

experimental entrance lengths for the times ranging from relatively large to relatively small values is made in Table 5.

Table 5. Comparison of theoretical and experimental dimensionless entrance lengths

Reynolds number	Dimensionless time (τ)	Entrance length (ξ)	
		Theoretical	Experimental
1610	47.83	27.8	163
	38.66	19.7	101
	29.89	13.3	40
	20.93	8.4	16
	17.94	5.7	9.2
	14.95	4.1	5.1
	11.96	3.1	3.3
	8.96	1.5	1.7
	5.98	0.7	0.7
700	10.41	4.6	73
	9.11	3.9	25
	8.46	3.5	15
	7.81	2.9	8
	7.16	2.6	4.2
	6.51	2.3	2.4
	3.25	0.8	0.9

As can be observed in Table 5, for large times, the theoretical entrance lengths are not in agreement with the experimentally determined values. The deviation from the experimental entrance length is as much as 50 to 600 per cent in the case of the Reynolds number 1610. For the Reynolds

number 700 the deviation is even higher. From the observed discrepancy it is evident that the theory using the integral momentum technique does not predict the entrance length accurately for large times.

The results presented in Table 5 also indicate that, for small times, when the boundary layer thickness is relatively small in comparison with tube radius, theory and experiment are in close agreement. With the data of Table 5, dimensionless time versus entrance length curves are plotted and presented in Figures 46 and 47 for the Reynolds numbers 1610 and 700, respectively. It can be observed in these curves that the theory and experiment agree well up to a certain time and then deviate from each other. The dimensionless boundary layer thickness up to which theory and experiment agree well is approximately 0.3.

C. Comparison of the Steady State Entrance Lengths

In the boundary layer and irrotational core model assumed for the entrance region flow, fully developed flow occurs when $\delta/R = 1$. The application of the integral momentum equation assumes that Poiseuille flow is established at this point although, in principle, infinite time and infinite distance are required for its establishment. In Figures 48 and 49 the experimental and theoretical entrance lengths are

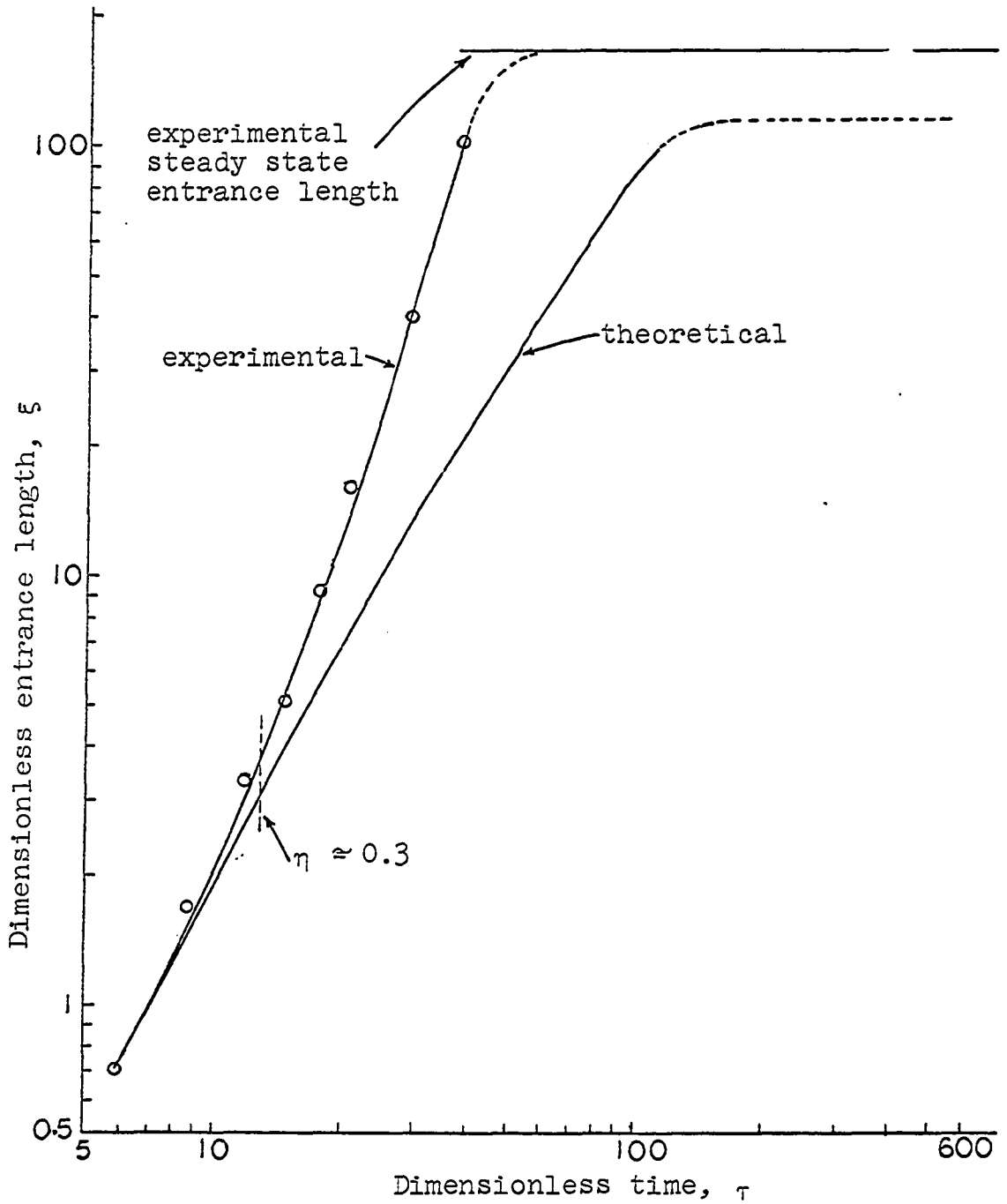

Fig. 46. Determination of the limiting value of the boundary layer thickness for which theory and experiment agree. Re = 1610.

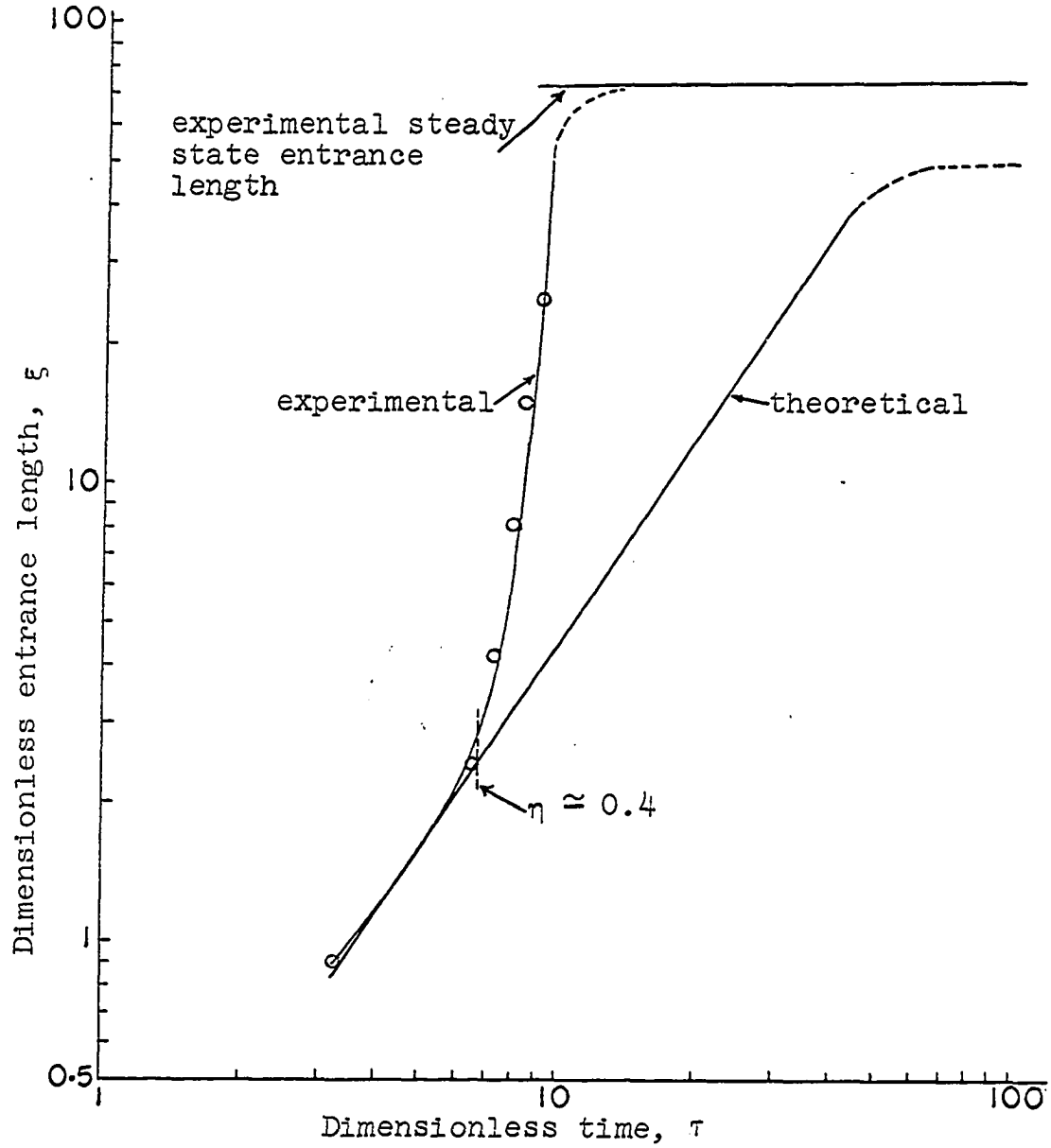

Fig. 47. Determination of the limiting value of the boundary layer thickness for which theory and experiment agree, Re = 700.

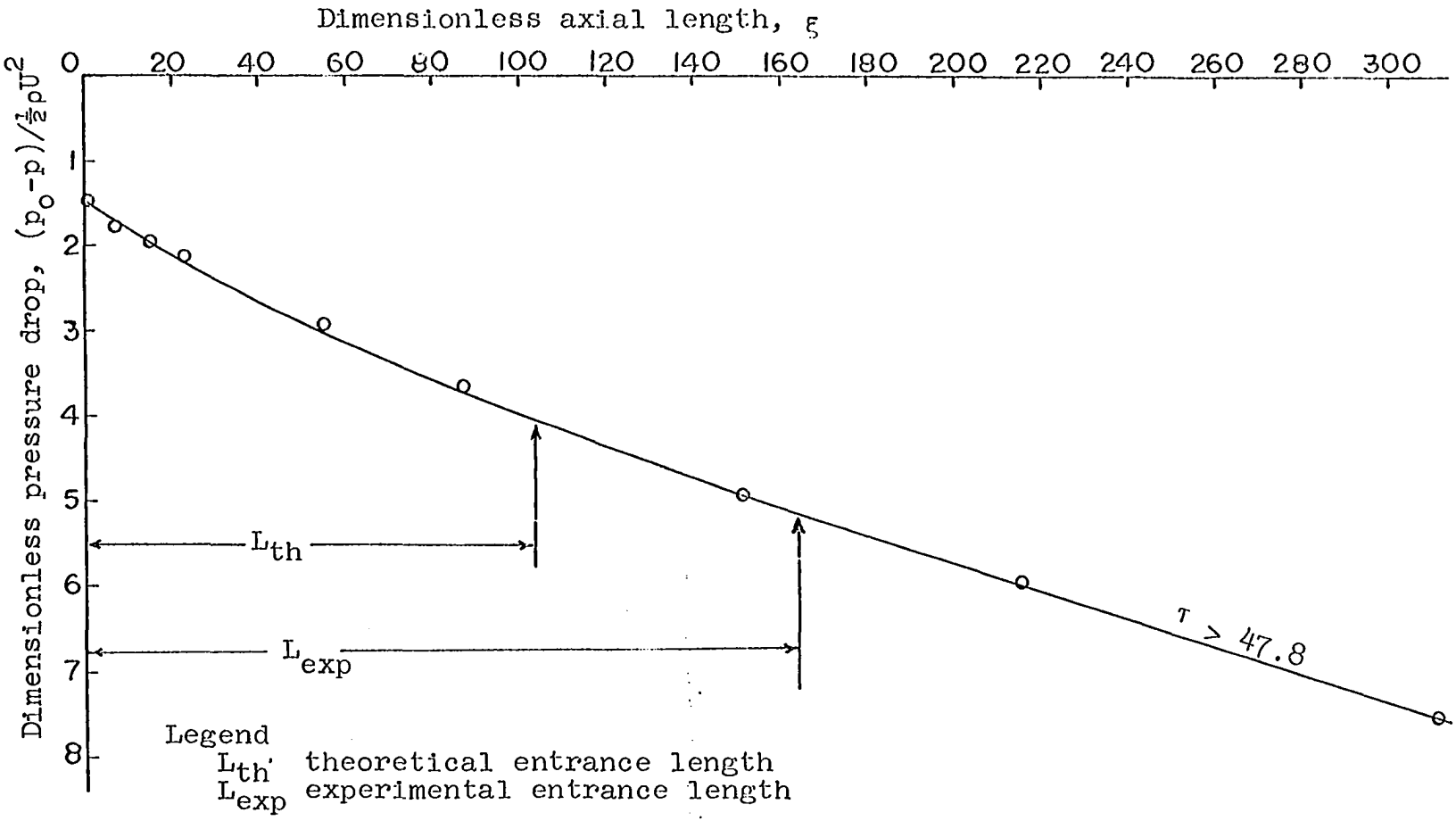

Fig. 48. Comparison of the theoretical and experimental entrance lengths for steady state, Re = 1610.

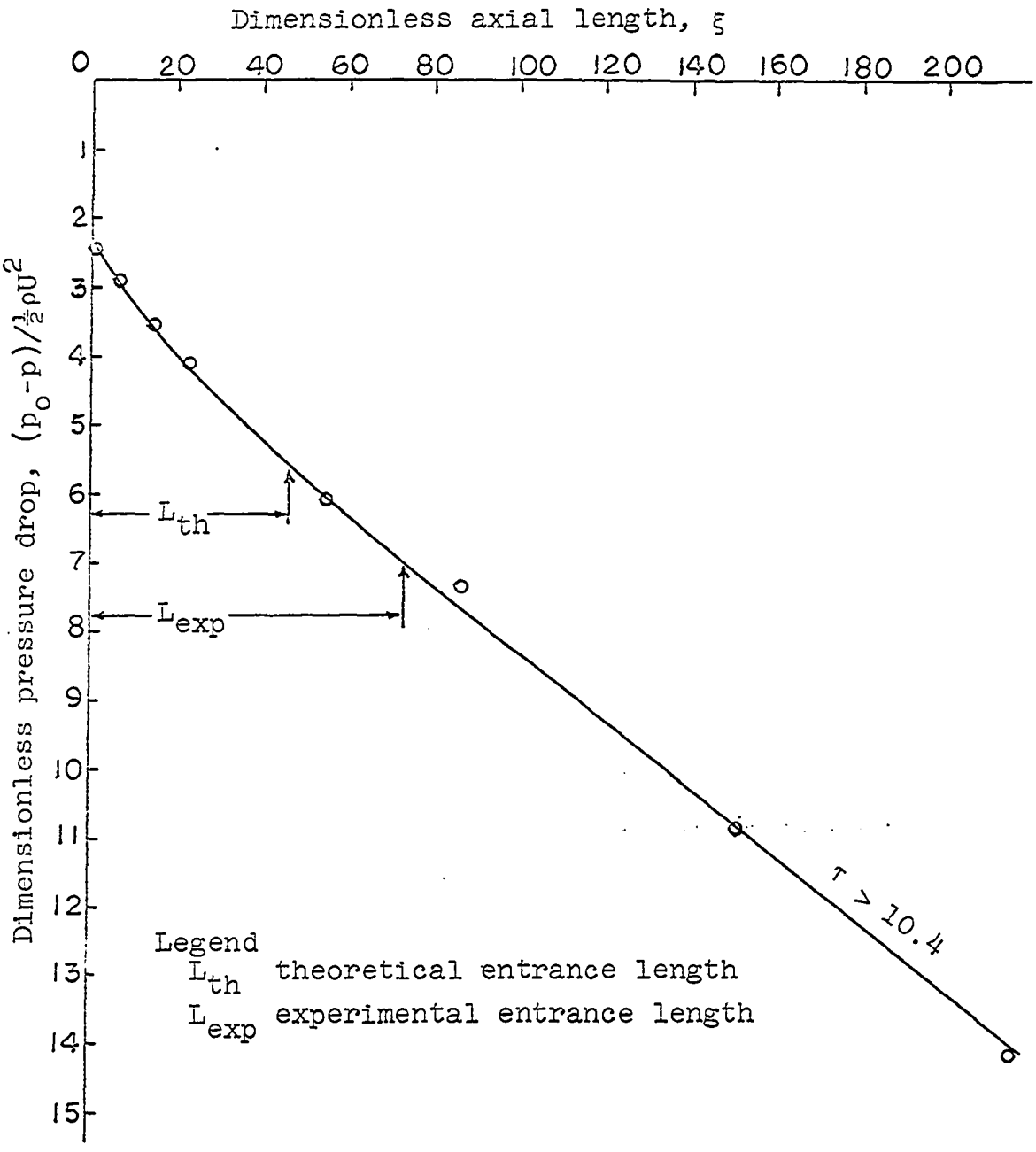

Fig. 49. Comparison of the theoretical and experimental entrance lengths for steady state, Re = 700.

shown for the Reynolds numbers 1610 and 700, respectively. The theoretical value of the steady state entrance length is determined from the computer solution at $\delta/R = 1$. In Table 6 the steady state entrance length expressed as a dimensionless parameter $\xi/2Re$ is compared with the entrance lengths obtained by various methods (20).

Table 6. Comparison of steady state entrance lengths

Source	$\xi/2$ Re
Boussinesque	0.065
Langhaar	0.057
Schiller	0.029
Modified cubic profile	0.030
Modified Pohlhausen method	0.0296
This investigation (theory, $\eta = 1$)	0.034
This investigation (experimental), Re = 1610	0.051
This investigation (experimental), Re = 700	0.052

It is observed from Table 6 that the theoretical methods employing the integral momentum equation give inaccurate entrance length in steady flow. The failure of the theory to predict accurately the entrance length in the steady flow is attributable to the assumption of the inviscid core in the central portion of the tube. The assumption of the inviscid core is good near the entrance where the boundary layer is thin, but as the boundary layer becomes thick downstream

the viscous effects from the tube wall are diffused into the flow field and the assumed inviscid core does not really exist, i.e., the velocity profile in the core is not flat as assumed. The experimental entrance length of the steady flow agrees with the theoretical entrance length obtained from the solutions of the Navier-Stokes equations (Boussinesque and Langhaar), rather than with those obtained from integral momentum methods.

VII. SUMMARY AND CONCLUSIONS

The problem of unsteady, laminar flow of a viscous, incompressible fluid in the entrance region of a circular tube was investigated. The unsteadiness of the flow was produced by rapidly setting the fluid in motion from a state of rest. The objectives of the investigation were to determine the boundary layer thicknesses, velocity profiles and instantaneous entrance lengths for this type of unsteady flow.

In the analytical treatment of the problem, the general integral momentum equation was applied to a fluid element in the entrance region. And by assuming a physical model, consisting of a growing boundary layer with a parabolic velocity profile and an accelerating irrotational core, Equation 24 was derived. Equation 24 is a first order quasi-linear partial differential equation. By the method of characteristics, this equation was reduced to a system of three ordinary differential equations (Equations 37), which were solved numerically. Assuming the entrance velocity to be a constant for all time the Equations 37 were reduced to Equations 39, which yielded a closed form solution. The closed form solution served to verify the computer program (Table 1).

The solution of Equations 37 was obtained in the form of a family of characteristics from which the boundary layer thicknesses at various instants were determined. A salient

feature of these characteristics was that the characteristic through the origin divided the characteristic space (the ξ-τ space, where ξ and τ are dimensionless axial distance and time respectively) into two regions in which the nature of the boundary layer development was significantly different. The two regions, designated as Region I and Region II are shown in Figures 31 and 36 for the Reynolds numbers of 1610 and 700. In Region I, the boundary layer thickness is a function of both axial distance and time, and in Region II, it is a function of time but independent of axial distance. The length of the tube beyond which the boundary layer thickness is independent of the axial distance is defined as the instantaneous entrance length. Since the characteristic through the origin is the boundary between the Region I and Region II, it gives the instantaneous entrance length. The boundary layer growth and entrance lengths for various times are presented in Figures 34 and 39. With Equations 9 and 21, and the boundary layer thickness determined from the characteristics, the velocity profiles were determined at various times and axial distances as shown in Figures 35 and 40.

The primary aim of the experiment was to determine the entrance lengths at various instants and compare these lengths with the theoretically determined values. It was also intended to develop a suitable experimental technique to study

unsteady flow problems of the type considered in the investigation. The pressures at various positions along the test section were measured while the fluid was rapidly set in motion and from this data the instantaneous pressure gradient curves were obtained as shown in Figures 23 and 24. From the pressure gradient curves the instantaneous entrance lengths were determined by identifying the axial distances beyond which the pressure gradient remained constant with respect to position. The entrance lengths thus determined from the experiment were compared with those obtained in the theoretical treatment of the problem. The experiments were carried out at the Reynolds numbers of 1610 and 700 determined on the basis of steady state velocity. From the unsteady pressure gradients in the fully developed region the unsteady entrance velocity was determined as described in Chapter V, and this velocity was used in the solution of the Equations 37. The experimental apparatus and technique seem to be satisfactory to study the unsteady flow problems of the type considered in this investigation.

From a comparison of the experimental and theoretical results the following conclusions are drawn:

With the use of the integral momentum equation it is possible to theoretically predict the instantaneous entrance length for small time, that is, when the boundary layer thickness is relatively small as compared to the radius of

the tube. The limiting value of the boundary layer thickness for which theory and experiment agree is estimated to be approximately 0.3R. For large times, as the boundary layer thickness becomes greater than 0.3R, the theory fails to predict the instantaneous entrance length accurately.

The failure to accurately predict the instantaneous entrance length for large time may be attributed to the assumption of the inviscid core in the central portion of the tube. For large times, as the boundary layer grows into the central portion of the tube, the viscous effects from the wall are diffused into the core fluid thus making the core no longer inviscid. The velocity profiles in the core fluid do not conform to the assumption of flat profiles, and the theory based on the integral momentum equation fails.

VIII. REFERENCES

1. Atabek, H. B. Unsteady and oscillatory flows in the entrance regions of co-axial tubes, tubes, and channels. Unpublished Ph.D. thesis. Minneapolis, Minnesota, Library, University of Minnesota. 1961.

2. Atabek, H. B., Chang, C. C. and Fingerson, L. M. Measurement of laminar oscillatory flow in the inlet length of a circular tube. Physics in Medicine and Biology 9: 219-227. 1964.

3. Campbell, W. D. and Slattery, J. C. Flow in the entrance of a tube. American Society of Mechanical Engineers Transactions Series D, 85: 41-44. 1963.

4. Carslaw, H. S. and Jaeger, J. C. Operational methods in applied mathematics. 2nd edition. New York, N.Y., Dover Publications, Inc. 1963.

5. Garabedian, P. R. Partial differential equations. 1st edition. New York, N.Y., John Wiley and Sons, Inc. 1964.

6. Gerbes, W. Zur instationären, laminaren Strömung einer inkompressiblen, zähen Flussigkeit in kreiszylindrischen Röhren. Zeitschrift für Angewandte Physik 3: 267-271. 1951.

7. Gill, S. A process for the step-by-step integration of differential equations in an automatic digital computing machine. Cambridge Philosophical Society Proceedings 47: 96-108. 1951.

8. Goldstein, S. Modern developments in fluid dynamics. 1st edition. New York, N.Y., Dover Publications, Inc. 1965.

9. Han, L. S. Hydrodynamic entrance length for incompressible flow in rectangular ducts. American Society of Mechanical Engineers Transactions Series E, 82: 403-409. 1960.

10. Hildebrand, F. B. Advanced calculus for applications. 3rd edition. Englewood Cliffs, N.J., Prentice-Hall, Inc. 1963.

11. Hornbeck, R. W. Laminar flow in the entrance region of a pipe. Applied Scientific Research Section A, 13: 224-232. 1964.

12. Ito, H. Theory of laminar flow through a pipe with non-steady pressure gradients. Tohoku University, Sendai, Japan, Institute of High Speed Mechanics Report 30: 163-180. 1953.

13. Langhaar, H. L. Steady flow in the transition length of a straight tube. American Society of Mechanical Engineers Transactions 64: 55-58. 1942.

14. Lundgren, T. S., Sparrow, E. M. and Starr, S. B. Pressure drop due to the entrance region in ducts of arbitrary cross-section. American Society of Mechanical Engineers Transactions Series D, 86: 620-626. 1964.

15. Pearson, J. D. Numerical solution of the Navier-Stokes equations for the entrance region of suddenly accelerated parallel plates. Unpublished Ph.D. thesis. Ames, Iowa, Library, Iowa State University of Science and Technology. 1966.

16. Rogge, T. R. and Young, D. F. Transient flow in parallel-plate channels and circular tubes with prescribed discharge. Iowa State University of Science and Technology Engineering Research Institute Report 58. 1967.

17. Schiller, L. Die Entwicklung der laminaren Geschwindigkeitsverteilung and ihre Bedeutung für Zahigkeitsmessungen. Zeitschrift für Angewandte Mathematik und Mechanik 2: 96-106. 1922.

18. Schlichting, H. Boundary layer theory. 4th edition. New York, N.Y., McGraw-Hill Book Co., Inc. 1962.

19. Schuh, H Calculation of unsteady boundary layers in two-dimensional laminar flow. Zeitschrift für Flugwissenschaften 5: 122-131. 1953.

20. Shapiro, A. H., Siegel, R. and Kline, S. J. Friction factor in the laminar entry region of a smooth tube. U.S. National Congress of Applied Mechanics Proceedings 2: 733-741. 1954.

21. Sneddon, I. N. Elements of partial differential equations. 1st edition. New York, N.Y., McGraw-Hill Book Co., Inc. 1957.

22. Stewartson, K. On the impulsive motion of a flat plate in a viscous fluid. Quarterly Journal of Mechanics and Applied Mathematics 4: 182-198. 1951.

23. Szymanski, P. Sur l'ecoulement non permanent du fluide visqueux dans le tuyau. International Congress of Applied Mechanics Proceedings 1: 249-254. 1930.

24. Wang, Y. L. and Longwell, P. A. Laminar flow in the inlet section of parallel plates. American Institute for Chemical Engineers Journal 10: 323-326. 1964.

IX. ACKNOWLEDGEMENTS

The author wishes to express his deep gratitude to Dr. Donald F. Young whose advice and guidance were invaluable during the course of this investigation.

Sincere appreciation is due to Dr. Thomas R. Rogge, Mrs. Marilyn Mohling and Mrs. June Smith for their help in computer programming. The author takes this opportunity to thank Dr. Kenneth G. McConnell and Dr. G. A. Nariboli for their numerous helpful suggestions at various stages of this investigation.

The author is indebted to Dr. Harry J. Weiss, chairman, Department of Engineering Mechanics and to the administration of the Engineering Research Institute, Iowa State University for making the funds available to complete this work.

The participation of Dr. G. K. Serovy of the Department of Mechanical Engineering and Dr. Robert J. Lambert of the Department of Mathematics in the Graduate Committee is sincerely appreciated.

Thanks to Sulochana, the author's wife, for her patience and encouragement which helped to complete this investigation.

X. APPENDIX A

LISTING OF THE COMPUTER PROGRAM FOR THE SOLUTION OF THE SYSTEM OF EQUATIONS 37 REYNOLDS NUMBER 700

```
      COMMON VAR(14,3),A(4),B(4),C(4),H,BYHAL,ENDVA,FLAG,X,N,
     1T,PHSIG,NODUM,NODUB,ENDNO,IO,XLAB(5),YLAB(5),GLAB(5),
     1DATLAB(5),XICO(500),ETACO(500),TAUCO(500),NPTS,
     1TAU2(27),QSTAR(27),ARG(27),VAL(27)
      INTEGER ENDNO,T,PHSIG
C     VAR(1,1)=XI,VAR(1,2)=ETA,VAR(1,3)=TAU
      IO=3
      READ(1,1) N,H,T,BYHAL,ENDVA,PHSIG,NODUM,NODUB,ENDNO,
     1XLAB,YLAB,GLAB,DATLAB
    1 FORMAT(I5,F5.0,I5,F5.0,E5.0,4I5,/,20A4)
      TAU2(1)=0.
      QSTAR(1)=.000001
      READ(1,20) (TAU2(I),I=2,27)
      READ(1,20)(QSTAR(I),I=2,27)
   20 FORMAT (8F10.0)
      VAR(1,1)=0.
      VAR(1,2)=0.
      VAR(1,3)=0.0
      X=0.
      H=1000.
      NPTS=0
      CALL NODE
      CALL GRAPH (NPTS,XICO,TAUCO,4,21,8.0,10.0,0,0,0,0,
     1XLAB,YLAB,GLAB,DATLAB)
      DO 10 MM=1,8
      X=0.
      H=50.
      VAR(1,1)=0.0
      VAR(1,2)=0.0
      VAR(1,3)=2.5*MM
      NPTS=0
      WRITE(3,9)
      CALL NODE
      CALL GRAPH (NPTS,XICO,TAUCO,4,21,0,0,0,0,0,0,0,0,0,0)
   10 CONTINUE
      DO 12 MM=1,16
      X=0.
      H=1000.
      VAR(1,1)=2.5*MM
      VAR(1,2)=0.
      VAR(1,3)=0.
      WRITE(3,9)
    9 FORMAT(///////)
```

```
      NPTS=0
      CALL NODE
      CALL GRAPH (NPTS,XICO,TAUCO,4,21,0,0,0,0,0,0,0,0,0,0)
   12 CONTINUE
   11 STOP
      END
```

```
      SUBROUTINE COMPD
      COMMON VAR(14,3),A(4),B(4),C(4),H,BYHAL,ENDVA,FLAG,X,N,
     1T,PHSIG,NODUM,NODUB,ENDNO,IO,XLAB(5),YLAB(5),GLAB(5),
     1DATLAB(5),XICO(500),ETACO(500),TAUCO(500),NPTS,
     1TAU2(27),QSTAR(27),ARG(27),VAL(27)
      INTEGER ENDNO,T,PHSIG
      D=0.6*VAR(1,2)-0.183333*VAR(1,2)*VAR(1,2)
      E=0.333333-0.166667*VAR(1,2)
      FF=0.066667-0.05*VAR(1,2)
      G=1.0-0.666667*VAR(1,2)+0.166667*VAR(1,2)*VAR(1,2)
      P=0.333333*VAR(1,2)-0.083333*VAR(1,2)*VAR(1,2)
      PEE=0.9873424*(VAR(1,3)**0.52)*EXP(-1.175*VAR(1,3))-
     10.000964*EXP(-0.625*VAR(1,3))+
     10.016692*EXP(-0.01653*VAR(1,3))+
     10.003584*EXP(-0.08706*VAR(1,3))+
     10.001908*EXP(-0.21394*VAR(1,3))
      IF(VAR(1,3)-95.) 3,2,2
    2 QUE=0.
      GO TO 5
    3 QUE=0.001856*EXP(-0.39723*VAR(1,3))-
     10.022064*EXP(-0.63694*VAR(1,3))-
     10.000584*EXP(-0.93303*VAR(1,3))-
     10.0001976*EXP(-1.28557*VAR(1,3))-
     10.0000924*EXP(-1.69448*VAR(1,3))
      IF(VAR(1,3)-22.) 6,5,5
    5 AAR=0.
      ESS=0.
      GO TO 8
    6 AAR=-0.0000504*EXP(-2.15977*VAR(1,3))-
     10.0000304*EXP(-2.68143*VAR(1,3))-
     10.0000195*EXP(-3.25943*VAR(1,3))-
     10.0000132*EXP(-3.894*VAR(1,3))-
     10.0000092*EXP(-4.58457*VAR(1,3))
      ESS=-0.0000067*EXP(-5.332*VAR(1,3))-
     10.0000049*EXP(-6.1357*VAR(1,3))-
     10.0000038*EXP(-6.996*VAR(1,3))
C     R=TIME DERIVATIVE OF UNSTEADY VELOCITY QSTAR
    8 R=PEE+QUE+AAR+ESS
      CALL ATSM(27,1,27)
      CALL ALI(Q,27,EPS,IER)
      QOVER=Q/G
C     S=4/REYNOLDS NUMBER
      S=0.005714
      VAR(8,1)=2.0*VAR(1,2)*Q*Q*((D*E)+(FF*G))
      VAR(8,2)=S*Q*G*G-VAR(1,2)*P*G*G*R
      VAR(8,3)=Q*VAR(1,2)*E*G
      RETURN
      END
```

```
 SUBROUTINE COMPY
 COMMON VAR(14,3),A(4),B(4),C(4),H,BYHAL,ENDVA,FLAG,X,N,
1T,PHSIG,NODUM,NODUB,ENDNO,IO,XLAB(5),YLAB(5),GLAB(5),
1DATLAB(5),XICO(500),ETACO(500),TAUCO(500),NPTS,
1TAU2(27),QSTAR(27),ARG(27),VAL(27)
 INTEGER ENDNO,T,PHSIG
 CALL COMPD
 RETURN
 END
```

```
      SUBROUTINE COMPT
      COMMON VAR(14,3),A(4),B(4),C(4),H,BYHAL,ENDVA,FLAG,X,N,
     1T,PHSIG,NODUM,NODUB,ENDNO,IO,XLAB(5),YLAB(5),GLAB(5),
     1DATLAB(5),XICO(500),ETACO(500),TAUCO(500),NPTS,
     1TAU2(27),QSTAR(27),ARG(27),VAL(27)
      INTEGER ENDNO,T,PHSIG
      WRITE(3,5) X,VAR(1,1),VAR(1,2),VAR(1,3)
    5 FORMAT (6E16.6)
      NPTS=NPTS+1
      XICO(NPTS)=VAR(1,1)
      ETACO(NPTS)=VAR(1,2)
      TAUCO(NPTS)=VAR(1,3)
      IF(X-ENDVA) 6,10,10
    6 IF(VAR(1,3)-100.)7,7,10
   10 FLAG=-1.0
    7 RETURN
      END
```

```
      SUBROUTINE COMPE
C     INTERVAL CHECK
      COMMON VAR(14,3),A(4),B(4),C(4),H,BYHAL,ENDVA,FLAG,X,N,
     1T,PHSIG,NODUM,NODUB,ENDNO,IO,XLAB(5),YLAB(5),GLAB(5),
     1DATLAB(5),XICO(500),ETACO(500),TAUCO(500),NPTS,
     1TAU2(27),QSTAR(27),ARG(27),VAL(27)
      INTEGER ENDNO,T,PHSIG
      IF (FLAG-.5)1,1,2
    1 WRITE (IO,4)
    4 FORMAT(@0@,10X,@HALVED@)
      RETURN
    2 WRITE (IO,3)
    3 FORMAT(@0@,10X,@DOUBLED@)
      RETURN
      END
```

```
      SUBROUTINE PREDI
C  PREDICT  Y-VALUE
      COMMON VAR(14,3),A(4),B(4),C(4),H,BYHAL,ENDVA,FLAG,X,N,
     1T,PHSIG,NODUM,NODUB,ENDNO,IO,XLAB(5),YLAB(5),GLAB(5),
     1DATLAB(5),XICO(500),ETACO(500),TAUCO(500),NPTS,
     1TAU2(27),QSTAR(27),ARG(27),VAL(27)
      INTEGER ENDNO,T,PHSIG
      DO 450 I=1,N
  450 VAR(1,I)=(1.547651E0*VAR(2,I))-(1.867505E0*VAR(3,I)) +
     1 (2.017207E0*VAR(4,I)) - (.6973528*VAR(5,I)) + H*
     2  ((2.002248*VAR(9,I)) - (2.031688*VAR(10,I)) +
     3(1.818611E0*VAR(11,I)) - (.7143201E0*VAR(12,I)))
      RETURN
      END
```

```
      SUBROUTINE CORRT(PERR)
C    CORRECT Y-VALUE
       COMMON VAR(14,3),A(4),B(4),C(4),H,BYHAL,ENDVA,FLAG,X,N,
     1T,PHSIG,NODUM,NODUB,ENDNO,IO,XLAB(5),YLAB(5),GLAB(5),
     1DATLAB(5),XICO(500),ETACO(500),TAUCO(500),NPTS,
     1TAU2(27),QSTAR(27),ARG(27),VAL(27)
       INTEGER ENDNO,T,PHSIG
       DO 462 I=1,N
  460  TEMP=VAR(2,I)+H*((.375*VAR(8,I))+(.7916667E0*VAR(9,I))
     1-(.2083333E0*VAR(10,I))+(.0416667E0*VAR(11,I)))
       IF (PHSIG)463,464,463
  463  TEMPA=ABS((TEMP-VAR(1,I))/TEMP)
       GO TO 465
  464  TEMPA=ABS(TEMP-VAR(1,I))
  465  VAR(1,I)=TEMP
       IF (PERR-TEMPA)461,462,462
  461  PERR=TEMPA
  462  CONTINUE
       RETURN
       END
```

```
      SUBROUTINE INITA
C  OBTAIN STARTING POINTS WITH RUNGE-KUTTA-GILL METHOD
      COMMON VAR(14,3),A(4),B(4),C(4),H,BYHAL,ENDVA,FLAG,X,N,
     1T,PHSIG,NODUM,NODUB,ENDNO,IO,XLAB(5),YLAB(5),GLAB(5),
     1DATLAB(5),XICO(500),ETACO(500),TAUCO(500),NPTS,
     1TAU2(27),QSTAR(27),ARG(27),VAL(27)
      INTEGER ENDNO,T,PHSIG
C     RUNGE-KUTTA-GILL  COEFFICIENTS
C      A(1)=.5
C      A(2)=.2928932E0
C      A(3)=1.707107E0
C      A(4)=.1666667E0
C      B(1)=1.
C      B(2)=A(2)
C      B(3)=A(3)
C      B(4)=.3333333E0
C      C(1)=.5
C      C(2)=A(2)
C      C(3)=A(3)
C      C(4)=.5
  401 DO 402 I=1,N
  402 VAR(6,I)=0.
      J=4
      GO TO 410
  403 DO 407 K=1,4
      DO 404 I=1,N
  500 CK=H*VAR(8,I)
  501 R=(A(K)*CK)-(B(K)*VAR(6,I))
  502 VAR(1,I)=VAR(1,I)+R
  404 VAR(6,I)=VAR(6,I)+(3.*R)-(C(K)*CK)
      IF (K-1)405,405,413
  413 IF (K-3)406,405,406
C     NEW VALUE OF X
  405 X=X+(H/2.)
      CALL COMPD
      GO TO 407
  406 CALL COMPY
  407 CONTINUE
      IF (NODUM)410,412,411
  412 NODUM=-1
  410 DO 408 I=1,N
      VAR(J+1,I)=VAR(1,I)
  408 VAR(J+8,I)=VAR(8,I)
      J=J-1
      IF (J)409,409,403
  409 RETURN
  411 CALL COMPT
      GO TO 410
      END
```

```
      SUBROUTINE NODE
C    NODE IS MAIN SUBPROGRAM  -- CONTROLLING SUBPROGRAM
      COMMON VAR(14,3),A(4),B(4),C(4),H,BYHAL,ENDVA,FLAG,X,N,
     1T,PHSIG,NODUM,NODUB,ENDNO,IO,XLAB(5),YLAB(5),GLAB(5),
     1DATLAB(5),XICO(500),ETACO(500),TAUCO(500),NPTS,
     1TAU2(27),QSTAR(27),ARG(27),VAL(27)
      INTEGER ENDNO,T,PHSIG
      CHECK1 = 16.21966 /(10**T)
      CHECK2 = CHECK1 / 200.
C     RUNGE-KUTTA-GILL  COEFFICIENTS
      A(1)=.5
      A(2)=.2928932E0
      A(3)=1.707107E0
      A(4)=.1666667E0
      B(1)=1.
      B(2)=A(2)
      B(3)=A(3)
      B(4)=.3333333E0
      C(1)=.5
      C(2)=A(2)
      C(3)=A(3)
      C(4)=.5
C     INITIALIZE
      FLAG=0.
  500 IF (BYHAL)502,501,502
  501 BYHAL=.5
  502 IF (ENDNO)503,504,503
C     ENDPOINT COMPUTES H
  503 H=(ENDVA-X)/ENDNO
C     PREPARE FOR RKG
  504 CALL COMPD
  505 CALL COMPT
      IF (FLAG)560,506,506
  506 CALL INITA
      NSWHF=1
      IF (ENDNO)507,508,507
  507 ENDNO=ENDNO-3
  508 M=3
  509 FLAG=0.
  510 X=X+H
  511 CALL PREDI
  512 CALL COMPD
  513 PERR=0.
  514 CALL CORRT(PERR)
  515 CALL COMPY
  516 IF (PERR-CHECK1            )517,517,535
C     NO HALVING NECESSARY
  517 NSWHF=0
      IF (NODUM)550,518,518
  518 IF (ENDNO)519,520,519
  519 ENDNO=ENDNO-1.
```

```
  520 CALL COMPT
      IF (FLAG)560,521,521
C     IS DOUBLING POSSIBLE
  521 IF (PERR- CHECK2                          )525,525,522
  522 M=3
  528 J=13
  523 DO 524 I=1,N
  524 VAR(J+1,I)=VAR(J,I)
      J=J-1
      IF (J)509,509,523
C     DOUBLING
  525 M=M-1
  526 IF (M)530,527,528
  527 IF (NODUB)522,529,522
  529 IF (ENDNO)530,531,530
  530 MOD=ENDNO/2
      MOD= ENDNO-MOD*2
      IF(MOD)528,531,528
  531 FLAG=2.
      CALL COMPE
      IF (FLAG)560,532,532
  532 DO 533 I=1,N
      VAR(2,I)=VAR(1,I)
      VAR(4,I)=VAR(5,I)
      VAR(5,I)=VAR(7,I)
      VAR(9,I)=VAR(8,I)
      VAR(11,I)=VAR(12,I)
  533 VAR(12,I)=VAR(14,I)
      H=2.*H
      IF (ENDNO)534,508,534
  534 ENDNO=ENDNO/2
      GO TO 508
C     HALVING
  535 FLAG=ABS(BYHAL)
      CALL COMPE
      IF (FLAG)560,561,561
  561 IF (NODUM)537,537,536
  536 CALL COMPT
      IF (FLAG)560,537,537
  537 IF (BYHAL-1.)548,517,517
  548 IF (ENDNO)543,542,543
  543 ENDNO=2 *ENDNO
  542 IF (NSWHF)538,540,538
C     REPEATED HALVING
  538 DO 539 I=1,N
      VAR(1,I)=VAR(5,I)
  539 VAR(8,I)=VAR(12,I)
      X=X-(4.*H)
      IF (ENDNO)549,549,544
  544 ENDNO=ENDNO+6.
  549 H=H*ABS(BYHAL)
```

```
      GO TO 506
  540 DO 541 I=1,N
      VAR(1,I)=VAR(2,I)
  541 VAR(8,I)=VAR(9,I)
      X=X-H
      GO TO 549
C     DUMMY OUTPUTTING
  550 X=X-(3.*H)
      IF (ENDNO)551,552,551
  551 ENDNO=ENDNO+2.
  552 K=3
      DO 553 I=1,N
      VAR(6,I)=VAR(1,I)
  553 VAR(13,I)=VAR(8,I)
  557 DO 554 I=1,N
      VAR(1,I)=VAR(K+1,I)
  554 VAR(8,I)=VAR(K+8,I)
      CALL COMPT
      IF (FLAG)560,562,562
  560 RETURN
  562 X=X+H
      K=K-1
      IF (K)558,558,555
  555 IF (ENDNO)556,557,556
  556 ENDNO=ENDNO-1
      GO TO 557
  558 DO 559 I=1,N
      VAR(1,I)=VAR(6,I)
  559 VAR(8,I)=VAR(13,I)
      NODUM=0
      GO TO 518
      END
```

```
      SUBROUTINE ALI(Y,NDIM,EPS,IER)
C
C
      COMMON VAR(14,3),A(4),B(4),C(4),D,BYHAL,ENDVA,FLAG,XX,N,
     1T,PHSIG,NODUM,NODUB,ENDNO,IO,XLAB(5),YLAB(5),GLAB(5),
     1DATLAB(5),XICO(500),ETACO(500),TAUCO(500),NPTS,
     1Z(27),F(27),ARG(27),VAL(27)
      EQUIVALENCE (X,VAR(1,3))
      IER=2
      XXX=.0001*X
      EPS=AMAX1(.00001,XXX)
      DELT2=0.
      IF(NDIM-1)9,7,1
C
C     START OF AITKEN-LOOP
    1 DO 6 J=2,NDIM
      DELT1=DELT2
      IEND=J-1
      DO 2 I=1,IEND
      H=ARG(I)-ARG(J)
      IF(H)2,13,2
    2 VAL(J)=(VAL(I)*(X-ARG(J))-VAL(J)*(X-ARG(I)))/H
      DELT2=ABS(VAL(J)-VAL(IEND))
      IF(J-2)6,6,3
    3 IF(DELT2-EPS)10,10,4
    4 IF(J-5)6,5,5
    5 IF(DELT2-DELT1)6,11,11
    6 CONTINUE
C     END OF AITKEN-LOOP
C
    7 J=NDIM
    8 Y=VAL(J)
    9 RETURN
C
C     THERE IS SUFFICIENT ACCURACY WITHIN NDIM-1 STEPS
   10 IER=0
      GOTO 8
C
C     TEST VALUE DELT2 STARTS OSCILLATING
   11 IER=1
   12 J=IEND
      GOTO 8
C
C     THERE ARE TWO IDENTICAL ARGUMENT VALUES IN VECTOR ARG
   13 IER=3
      GOTO 12
      END
```

```
C
      SUBROUTINE ATSM(IROW,ICOL,NDIM)
C
C
      COMMON VAR(14,3),A(4),B(4),C(4),D,BYHAL,ENDVA,FLAG,XX,M,
     1T,PHSIG,NODUM,NODUB,ENDNO,IO,XLAB(5),YLAB(5),GLAB(5),
     1DATLAB(5),XICO(500),ETACO(500),TAUCO(500),NPTS,
     1Z(27),F(27),ARG(27),VAL(27)
      EQUIVALENCE (X,VAR(1,3))
C
C     CASE IROW=1 IS CHECKED OUT
      IF(IROW-1)23,21,1
    1 N=NDIM
C
C     IF N IS GREATER THAN IROW, N IS SET EQUAL TO IROW.
      IF(N-IROW)3,3,2
    2 N=IROW
C
C     CASE IROW.GE.2
C     SEARCHING FOR SUBSCRIPT J SUCH THAT Z(J) IS NEXT TO X.
    3 IF(Z(IROW)-Z(1))5,4,4
    4 J=IROW
      I=1
      GOTO 6
    5 I=IROW
      J=1
    6 K=(J+I)/2
      IF(X-Z(K))7,7,8
    7 J=K
      GOTO 9
    8 I=K
    9 IF(IABS(J-I)-1)10,10,6
   10 IF(ABS(Z(J)-X)-ABS(Z(I)-X))12,12,11
   11 J=I
C
C     TABLE SELECTION
   12 K=J
      JL=0
      JR=0
      DO 20 I=1,N
      ARG(I)=Z(K)
      IF(ICOL-1)14,14,13
   13 VAL(2*I-1)=F(K)
      KK=K+IROW
      VAL(2*I)=F(KK)
      GOTO 15
   14 VAL(I)=F(K)
   15 JJR=J+JR
      IF(JJR-IROW)16,18,18
   16 JJL=J-JL
      IF(JJL-1)19,19,17
```

```
   17 IF(ABS(Z(JJR+1)-X)-ABS(Z(JJL-1)-X))19,19,18
   18 JL=JL+1
      K=J-JL
      GOTO 20
   19 JR=JR+1
      K=J+JR
   20 CONTINUE
      RETURN
C
C     CASE IROW=1
   21 ARG(1)=Z(1)
      VAL(1)=F(1)
      IF(ICOL-2)23,22,23
   22 VAL(2)=F(2)
   23 RETURN
      END
```

XI. APPENDIX B

The details of obtaining Equation 56 from Equation 54 in Chapter V are given in the following.

$$G(T) = \mathcal{L}^{-1}(G) = \frac{1}{2\pi i} \oint \frac{e^{sT} I_o(\sqrt{\frac{sRe}{2}} r^*)}{I_o(\sqrt{\frac{sRe}{2}})} \tag{54}$$

The integral in the Equation 54 can be evaluated by Cauchy's residue theorem, which is stated as

$$\oint f(z)dz = 2\pi i \sum_{k=1}^{n} \text{Res}(a_k)$$

where $\text{Res}(a_k)$ = residue of $f(z)$ at poles $z = a_k$

Let $$F(s) = e^{sT} \frac{I_o(\sqrt{\frac{sRe}{2}} r^*)/s}{I_o(\sqrt{\frac{sRe}{2}})} = e^{sT} \frac{N(s)}{D(s)} \tag{84}$$

so that $N(s) = I_o(\sqrt{\frac{sRe}{2}} r^*)/s$, and $D(s) = I_o(\sqrt{\frac{sRe}{2}})$. By Cauchy's residue theorem

$$\frac{1}{2\pi i} \oint F(s)ds = R_o + \sum_n R_n \tag{85}$$

where R_o = residue at $s = 0$

R_n = residue at $s = -\frac{\alpha_n^2}{Re/2}$, in which α_n are the roots of the Bessel function $J_o(\sqrt{sRe/2})$

The function $F(s)$ has simple poles at $s = 0$ and at $s = -2\alpha_n^2/Re$. That is, $F(s)$ is not finite at $s = 0$ and for $\sqrt{\frac{sRe}{2}} = i\,\alpha_n$. The residues are calculated as follows:

$$R_o = \lim_{s \to 0} sF(s) = \lim_{s \to 0} \frac{e^{st} I_o(\sqrt{\frac{sRe}{2}}\, r^*)}{I_o(\sqrt{\frac{sRe}{2}})} = 1 \tag{86}$$

Hildebrand (10) has shown that for simple poles the residue at $s = -\frac{2\alpha_n^2}{Re}$ is given by

$$R_n = e^{st} \frac{N(s)}{\left(\frac{dD}{ds}\right)} \Big|_{s=-2\alpha_n^2/Re}$$

From Equation 84

$$R_n = e^{st} \frac{I_o(\sqrt{\frac{sRe}{2}}\, r^*)/s}{\frac{d}{ds}\{I_o(\sqrt{\frac{sRe}{2}})\}} \Big|_{s=-\frac{2\alpha_n^2}{Re}}$$

$$= e^{st} \frac{I_o(\sqrt{\frac{sRe}{2}}\, r^*)/s}{I_1(\sqrt{\frac{sRe}{2}})\frac{Re/2}{2\sqrt{sRe/2}}} \Big|_{s=-\frac{2\alpha_n^2}{Re}}$$

$$= \frac{e^{-\frac{2\alpha_n^2}{Re}T} I_o(i\alpha_n r^*)}{-\frac{2\alpha_n^2}{Re} I_1(i\alpha_n)\frac{Re}{4i\alpha_n}} = -2\frac{e^{-\frac{2\alpha_n^2}{Re}T} I_o(i\alpha_n r^*)}{\alpha_n I_1(i\alpha_n)/i}$$

$$= -\frac{2\, e^{-\frac{2\alpha_n^2}{Re}T} J_o(\alpha_n r^*)}{\alpha_n J_1(\alpha_n)} \qquad (87)$$

From Equations 54, 85, 86 and 87

$$G(T) = 1 - 2\sum_{n=1}^{\infty} \frac{J_o(\alpha_n r^*)}{\alpha_n J_1(\alpha_n)} e^{-\frac{2\alpha_n^2}{Re}T} \qquad (88)$$

Equation 88 is the same as Equation 55 in Chapter V. From Equation 88 we can write

$$G(\tau - T) = 1 - 2\sum_{n=1}^{\infty} \frac{J_o(\alpha_n r^*)}{\alpha_n J_1(\alpha_n)} e^{-2\frac{\alpha_n^2}{Re}(\tau - T)}$$

With this result in Equation 53 of Chapter V we have

$$u_2^* = \int_0^\tau f(T)\{1-2\sum_{n=1}^{\infty}\frac{J_o(\alpha_n r^*)}{\alpha_n J_1(\alpha_n)}\, e^{-2\frac{\alpha_n^2}{Re}(\tau-T)}\}dT$$

$$= \int_0^\tau f(T)dT - 2\sum_{n=1}^{\infty}\frac{J_o(\alpha_n r^*)}{\alpha_n J_1(\alpha_n)}\int_0^\tau f(T)e^{-\frac{2\alpha_n^2}{Re}(\tau-T)}dT$$

$$= \int_0^\tau f(T)dT - 2\sum_{n=1}^{\infty}\frac{J_o(\alpha_n r^*)}{\alpha_n J_1(\alpha_n)}\int_0^\tau f(\tau-T)e^{-2\frac{\alpha_n^2}{Re}T}dT \qquad (89)$$

From Equation 52 in Chapter V and Equation 89 we have

$$u_2^* = u_1^* - 2\sum_{n=1}^{\infty}\frac{J_o(\alpha_n r^*)}{\alpha_n J_1(\alpha_n)}\int_0^\tau f(\tau-T)e^{-\frac{2\alpha_n^2}{Re}T}dT \qquad (90)$$

Since $u^* = u_1^* - u_2^*$ (see Equation 51 in Chapter V), Equation 90 can be written as

$$u^* = u_1^* - u_2^* = 2\sum_{n=1}^{\infty}\frac{J_o(\alpha_n r^*)}{\alpha_n J_1(\alpha_n)}\int_0^\tau f(\tau-T)e^{-\frac{2\alpha_n^2}{Re}T}dT \qquad (91)$$

$$= 2\sum_{n=1}^{\infty}\frac{J_o(\alpha_n r^*)}{\alpha_n J_1(\alpha_n)}F_n(\tau) \qquad (92)$$

where,

$$F_n(\tau) = \int_0^\tau f(\tau-T)e^{-\frac{2\alpha_n^2}{Re}T}dT \qquad (93)$$

Equations 92 and 93 are the same as Equations 56 and 57 in Chapter V, respectively.

XII. APPENDIX C

LISTING OF THE COMPUTER PROGRAM FOR DETERMINING TIME-DEPENDENT DISCHARGE FOR THE REYNOLDS NUMBERS 1610 AND 700

```
C
C
C
C
C
C
C
      DIMENSION Q(30),TAU(30),ALPHA(100),T(4800)
      READ(1,5) (ALPHA(I),I=1,60)
    5 FORMAT(8F10.0)
      WRITE(3,6)
    6 FORMAT(@1@,9X,@TAU@,13X,@Q*@)
      A=1.3
      B=.0235
      XK=1.175
      XL=.625
      XM=.52
      RE=700.
      H=.01
      J=29
   15 BRE=B*RE
      REL=XL*RE
      Q(1)=0.
      TAU(1)=0.
      READ(1,5) (TAU(I),I=2,J)
      DO 61 I=2,J
      XLTAU=-XL*TAU(I)
      SUM=0.
      DO 50 N=1,60
      N1=N
      C=2.*ALPHA(N)*ALPHA(N)
      C1=C/RE
      RELC=REL-C
C
C     COMPUTE THE INTEGRAL
C
      CALL QG5(0.,TAU(I),S,C1,XM,XK)
      TERMN = (BRE/(ALPHA(N)*ALPHA(N))) * (-EXP(-C1*TAU(I))*
     1(1./C+1./RELC) + 1./C + (1./RELC)*EXP(XLTAU)) +
     1 A*S/(ALPHA(N)*ALPHA(N))
      IF(N-1)80,20,55
C
C     CHECK FOR CONVERGENCE
   55 IF(ABS(TERMN/SUM)-.00001) 60,60,20
   20 SUM=SUM+TERMN
   50 CONTINUE
   58 Q(I)=4.*SUM
      GO TO 61
   60 Q(I)=4.*(SUM+TERMN)
   61 WRITE(3,65) TAU(I),Q(I),N1
```

```
65 FORMAT(2F15.7,I7)
   A=.095
   B=.01
   XK=.16129
   XL=.25
   XM=.18
   RE=1610.0
   GO TO 15
80 STOP
   END
```

```
      SUBROUTINE QG5(XL,XU,Y,C1,XM,XK)
      FCT(T)=T**XM * EXP(-XK*T+C1*(T-XU))
C
C        FCT(T) IS THE USER@S INTEGRAND
C
      A=.5*(XU+XL)
      B=XU-XL
      C=.4530899*B
      Y=.1184634*(FCT(A+C)+FCT(A-C))
      C=.2692347*B
      Y=Y+.2393143*(FCT(A+C)+FCT(A-C))
      Y=B*(Y+.2844444*FCT(A))
      RETURN
      END
```

UNSTEADY ENTRANCE VELOCITY FOR THE REYNOLDS NUMBERS 1610 AND 700

C
C

DIMENSIONLESS TIME	DIMENSIONLESS ENTRANCE VELOCITY RE=1610	RE=700
0.1	0.0052	0.0182
0.2	0.0116	0.0483
0.3	0.0186	0.0830
0.4	0.0258	0.1194
0.5	0.0332	0.1561
0.7	0.0483	0.2266
1.0	0.0713	0.3196
1.3	0.0944	0.3945
2.0	0.1469	0.5087
3.0	0.2167	0.5797
5.0	0.3343	0.6119
7.0	0.4245	0.6205
10.0	0.5194	0.6387
12.0	0.5629	0.6549
15.0	0.6079	0.6822
18.0	0.6368	0.7093
22.0	0.6606	0.7395
25.0	0.6722	0.7559
30.0	0.6856	0.7716
35.0	0.6957	0.7766
40.0	0.7047	
47.0	0.7170	
50.0	0.7223	
60.0	0.7403	
70.0	0.7582	
80.0	0.7757	

XIII. APPENDIX D

Table 7. Pressure drop data for the Reynolds number 1610

Dimensionless time, τ	Dimensionless pressure drop, $(p_o-p)/\frac{1}{2}\rho U^2$ at various axial positions					
	Tap 1	Tap 2	Tap 3	Tap 4	Tap 5	Tap 6
0.149	0.68	1.31	2.17	2.88	5.74	8.12
0.448	1.31	2.09	3.39	4.38	8.46	12.58
0.897	1.57	2.51	3.96	5.08	10.34	15.13
1.046	1.57	2.49	3.98	5.19	10.43	15.30
1.196	1.57	2.62	4.04	5.19	10.51	15.51
1.345	1.52	2.49	3.98	5.03	10.48	15.48
1.495	1.49	2.41	3.93	4.98	10.27	15.35
2.989	1.49	2.38	3.62	4.64	9.41	13.94
5.979	1.49	2.09	3.09	3.67	7.53	11.28
8.969	1.49	1.91	2.47	2.93	5.79	8.54
11.958	1.49	1.87	2.09	2.48	4.43	6.47
14.963	1.49	1.85	2.06	2.35	4.19	5.63
17.947	1.49	1.80	1.98	2.04	3.84	4.82
20.928	1.49	1.78	1.96	2.25	3.49	4.70
29.897	1.49	1.78	1.93	2.21	3.04	3.98
38.866	1.49	1.78	1.93	2.12	2.91	3.73
47.835	1.49	1.78	1.93	2.12	2.91	3.68

Table 7 (Continued)

Dimensionless time, τ	Dimensionless pressure drop, $(p_o-p)/\frac{1}{2}\rho U^2$ at various axial positions					
	Tap 7	Tap 8	Tap 9	Tap 10	Tap 11	Tap 12
0.149	15.46	19.22	29.84	39.29	47.26	65.52
0.448	23.84	32.04	47.42	66.15	86.54	112.61
0.897	26.96	36.46	55.48	76.49	98.23	130.50
1.046	27.23	36.67	55.67	76.72	99.00	131.00
1.196	27.42	37.58	55.81	77.66	100.02	131.38
1.345	27.16	36.50	55.43	76.52	99.00	131.00
1.495	26.80	36.23	54.76	75.00	96.10	128.12
2.989	24.63	34.00	49.48	69.22	89.10	117.91
5.979	19.56	27.11	39.00	54.38	69.60	92.89
8.969	14.75	19.72	28.52	39.53	51.10	68.10
11.958	11.27	14.62	20.92	30.00	38.52	51.63
14.963	9.63	13.11	18.33	25.33	33.42	44.58
17.947	9.37	11.42	15.61	22.29	28.02	37.72
20.928	7.32	9.58	13.10	18.49	22.78	30.40
29.897	5.71	7.31	9.95	13.30	16.22	22.08
38.866	5.09	6.41	8.51	11.25	13.87	19.64
47.835	4.91	5.97	7.51	10.30	12.77	17.16

Table 8. Pressure drop data for the Reynolds number 700

Dimensionless time, τ	Dimensionless pressure drop, $(p_o-p)/\frac{1}{2}\rho U^2$ at various axial positions					
	Tap 1	Tap 2	Tap 3	Tap 4	Tap 5	Tap 6
0.05	2.77	6.12	8.80	12.77	20.72	30.41
0.156	5.54	10.26	17.15	22.68	38.71	58.10
0.260	6.92	11.76	18.92	24.89	48.65	73.18
0.286	6.92	11.76	19.08	25.10	49.25	75.30
0.312	6.36	11.07	16.75	24.35	48.15	72.68
0.364	5.95	10.92	16.60	23.91	47.75	71.90
0.781	5.25	9.68	14.24	20.47	39.00	60.82
1.561	2.76	5.53	8.85	12.46	27.25	41.49
3.253	2.49	3.70	5.22	6.51	12.30	18.00
6.506	2.49	3.58	4.57	5.56	10.04	13.22
7.156	2.49	3.40	4.11	4.88	8.05	11.47
7.807	2.49	3.31	3.88	4.57	6.83	10.00
8.458	2.49	3.16	3.78	4.30	6.25	9.02
9.108	2.49	2.91	3.53	4.12	6.08	7.68
9.758	2.49	2.91	3.53	4.12	5.88	7.50
10.409	2.49	2.91	3.53	4.12	5.88	7.39

Table 8. (Continued)

Dimensionless time, τ	Dimensionless pressure drop, $(p_o-p)/\frac{1}{2}\rho U^2$ at various axial positions					
	Tap 7	Tap 8	Tap 9	Tap 10	Tap 11	Tap 12
0.052	45.62	58.08	86.47	112.90	142.52	185.20
0.156	85.73	121.72	172.80	235.00	298.72	396.00
0.260	127.31	178.80	248.93	346.03	442.64	587.13
0.286	130.24	181.06	260.02	360.00	464.90	622.00
0.312	129.52	180.02	258.61	357.13	456.30	611.22
0.364	124.63	178.38	253.13	351.10	453.82	605.06
0.781	109.82	152.10	216.41	304.00	387.52	523.24
1.561	73.26	103.75	146.32	207.50	265.00	362.15
3.253	31.81	45.10	62.25	87.10	112.14	149.43
6.506	21.86	28.40	39.52	47.81	59.26	76.33
7.156	17.33	22.64	31.20	39.84	49.00	66.12
7.807	14.92	19.11	26.72	35.68	44.89	60.86
8.458	13.12	16.66	24.13	32.44	41.42	55.30
9.108	12.00	15.75	22.21	30.11	38.43	52.16
9.758	11.41	14.82	20.59	29.58	36.04	49.58
10.409	10.75	13.88	19.87	28.38	34.46	48.00